Ultrafast Laser-induced Spin Dynamics in advanced materials

Guanqi Li

Doctor of Philosophy

University of York

Physics

July 2021

Abstract

Helicity-dependent all-optical induced magnetization switching has been achieved in Pt/Co/Pt samples with perpendicular magnetic anisotropy. Applying a dual-pump laser excitation, first with a linearly polarized (LP) laser pulse followed by a circularly polarized (CP) laser pulse, the timescales and contribution from heating and helicity effects in HD-AOS were identified with a Pt /Co /Pt triple-layer. When the LP laser pulses preheat the sample to a nearly fully demagnetized state, the CP laser pulses with a power reduced by 80% switch the sample's magnetization. By varying the time delay between the two pump pulses, the results show that the helicity effect, which gives rise to the deterministic helicity-induced switching, arises almost instantly within 200fs close to the pulse width upon laser excitation.

All-optical-induced magnetization switching in Pt/Co/Pt triple layers has been further explored as a function of the thickness of the Co and Pt layers, respectively. The Ab initio calculation shows that the Pt atom significantly improves the spin-orbit coupling of Co's 3d electrons. This enhanced spin-orbital coupling only occurs at the Pt/Co interface. Moreover, the ab initio calculation gives a surprising interlayer antiferromagnetic coupling in the Co/Pt multilayer system, which is due to the oscillation of the RKKY coupling.

The effect of ultrafast laser heating on the interlayer antiferromagnetic coupling of synthetic antiferromagnetic tri-layers has been investigated by time-resolved pump-probe measurements together with transient hysteresis loop measurements at selected time delays. Time-resolved Kerr hysteresis loop measurements have shown that the interlayer antiferromagnetic coupling can be transiently suppressed by the laser's heating effect within the first picosecond after laser excitation. While the Kerr rotation time scans show, the antiferromagnetic coupling can be transferred into an apparent ferromagnetic coupling state and then recovered to the antiferromagnetic coupling state as the recovery of the magnetization of each Co layer.

List of Contents

List of Figures

List of Tables

Acknowledgements

First and foremost, I would like to show my deepest gratitude to my supervisors, Dr. Jing Wu in Department of Physics and Prof. Yongbing Xu in Department of Electronics. They are respectable, responsible and resourceful scholar, who has provided me with valuable guidance in every stage of my Ph.D. research. Without their enlightening instruction, impressive kindness and patience, I could not have completed my thesis. Their keen and vigorous academic observation enlightens me not only in this thesis but also in my future study.

I would like to thank my colleagues and we have shared a wonderful experience and time here. Your names are: Dr. Xianyang Lu, Dr Xiangyu Zheng, Dr Yu Yan, Dr. Junlin Wang, Dr. Yichuan Wang, Dr. Kunpeng Zhang, and Dr. Kelvin.

I would like to thank my cat Pangpang. Its companionship always make me feel like everything would be better.

I am grateful to the Department of Physics for funding my study at University of York.

Last but not least I would like to thank my parents for their unwavering support and encouragement throughout my PhD study here and my life.

Declaration

I declare that this thesis titled, “Ultrafast laser-induced spin dynamics in advanced materials, and the work presented in it are my own. I confirm that:

This work was done wholly or mainly while in candidature for a research degree at University of York and has not been submitted previously for a degree at this or any other university. All sources are acknowledged as references. I am solely responsible for all the research work described in this thesis except for the following collaborations:

In chapter 4, the sample was prepared by Jianwang Cai. After discussion with myself, the atomic two-temperature simulations were done by Junling Wang.

Guanqi Li

July 2021 in China

Publication List

1. **Li, G.**, Zheng, X., Wang, J., Lu, X., Wu, J., Cai, J., Ostler, T. and Xu, Y., 2020. Timescales and contribution of heating and helicity effect in helicity-dependent all-optical switching. *arXiv preprint arXiv:2009.12816*. Accepted by Rare metals

2. Zheng, X., Wang, J., **Li, G**., Lu, X., Li, W., Wang, Y., Chen, L., Yin, H., Wu, J. and Xu, Y., 2020. Paradigm of Magnetic Domain Wall-Based In-Memory Computing. *ACS Applied Electronic Materials*, *2*(8), pp.2375-2382.

3. Lu, X., Atkinson, L.J., Kuerbanjiang, B., Liu, B., **Li, G**., Wang, Y., Wang, J., Ruan, X., Wu, J., Evans, R.F. and Lazarov, V.K., 2019. Enhancement of intrinsic magnetic damping in defect-free epitaxial Fe3O4 thin films. *Applied Physics Letters*, *114*(19), p.192406.

4. Yin, H., Zheng, X., Wang, J., Zhou, Y., Kuerbanjiang, B., **Li, G.**, Lu, X., Wang, Y., Wu, J., Lazarov, V.K. and Evans, R.F., 2020. Defect-Correlated Skyrmions and Controllable Generation in Perpendicularly Magnetized CoFeB Ultrathin Films. *arXiv preprint arXiv:2006.02864*. Accepted by Applied Physics Letters

Chapter 1 Introduction

1.1 History of magnetic recording

Magnetism has attracted human attention for over 2500 years. About 400 BC, the Chinese had the record of the naturally occurring mineral magnetite, Fe_3O_4. Nearly one decade later, the ancient Chinese discovered the interaction between the geomagnetic field and magnetic materials, and they used this phenomenon for navigation. The first compass is the so-call Si Nan. Nowadays, as one of the four pillars of modern physics, humans can easily manipulate the electromagnetic force and utilize it for our needs. With the development of magnetism, people have invented many technological devices based on magnetism and magnetic materials. One could give many examples like permanent magnet motor, sound and video systems components, nuclear magnetic resonance image, magnetic sensors, hard disks and its read/write heads. Nevertheless, the most important achievement in magnetism is the magnetic recording of information.

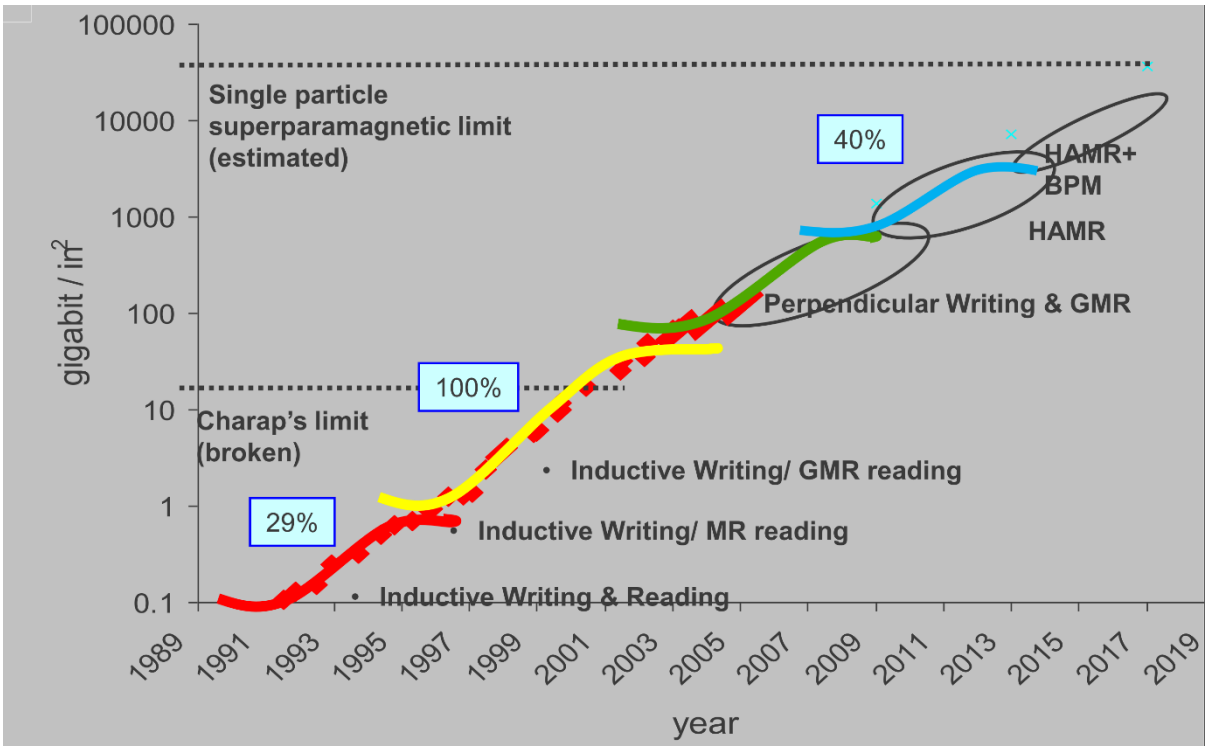

Figure 1.1 Development of HDD data storage density [1].

Since the 1950s, fast-growing information technology has given birth to binary data storage. At first, the computer system's data storage was based on the punched card and pantograph, whose writing and reading speeds are both far behind the computational speed. This restriction was not released until magnetic materials were used for information storage. Magnetic materials are perfect binary data carriers, as the spin's direction is also binary. Spin up and down correspond to 0 and 1, respectively. In 1957, IBM introduced a revolutionary product, the IBM 305 RAMAC (random access method of accounting and control) [2]. This first hard disc driver (HDD) has an information storage areal density (AD) of $2\ \mathrm{kbit/in^2}$. It almost doubled every two years and rocketed to $2.6\ \mathrm{Gbit/in^2}$ in 1997. Several technologies contribute significantly to this miracle, including a thin film head, magnetoresistance (MR) head and the partial response maximum likelihood (PRML) signal process system. Then the giant magnetoresistance (GMR) was discovered independently by the groups of Albert Fert and Peter Grunberg in 1988 [3, 4], and after ten years, the GMR reading head was created by IBM, and then the hard disk drive (HDD) AD rapidly grew to $12\ \mathrm{Gbit/in^2}$ in 1999 [5]. Due to its great improvement in information storage, the 2007 Nobel Prize in Physics was awarded to Albert Fert and Peter Grunberg for the discovery of GMR.

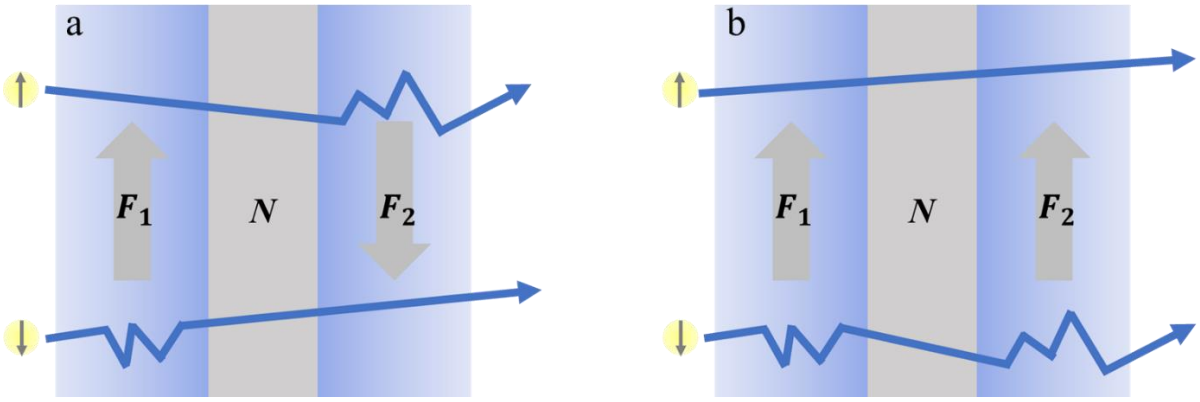

Figure 1.2 Schematic representation of spin valve based on the GMR effect. An unpolarized current flows through a tri-layer film with two ferromagnetic layers, F_1 and F_2, sandwiching a nonmagnetic metal spacer layer N. The magnetic directions of F_1 and F_2 are parallel in (a) and antiparallel in (b).

GMR originates from spin-related electrons scattering. FIG 1.2 shows a GMR sensor a spin valve, while FIG 1.2. (a) shows the high resistance state and FIG 1.2. (b) shows the low resistance state. An unpolarized current flows through this structure, and electrons with spin up and down scatter

differently. When the electron's spin direction and the ferromagnetic layer's magnetic direction are antiparallel, the high scattering probability results in a high resistance is R_H. Otherwise, it will have a low resistance R_L. According to the results of Albert Fert and Peter Grunberg, the GMR ratio in Fe(3 nm)/Cr(0.9 nm) superlattices at 4.2 K is about 80 % [3]. For the GMR reading head, an antiferromagnetic layer is added to this structure, which can fix the magnetic layer's direction by exchange coupling. This layer is called the pinning layer, and the other is called the free layer. The free layer's direction could be changed by an external magnetic field or current, and the information stored can be read by measuring the current flowing through this structure.

A new bottleneck appeared after GMR. From 2002 to 2006, the increasing rate of the storage density dropped to about 25% to 40% per year. In addition to increasing HDD's head sensitivity, the HDD industry also focused on decreasing the magnetic grain size in each data bit. However, thermal fluctuation plays a more and more important role in the reduction of magnetic grain size. Furthermore, it will approach the so-called superparamagnetic limit. The magnetic direction of each magnetic grain is protected by the magnetic anisotropy energy barrier K_1V. Here, V is the volume of the magnetic grain, and K_1 is the magnetic anisotropy constant, which is related to the material. The magnetic relaxation time due to the thermal effect is determined by the equation:

$$\frac{1}{\tau} = f_0 e^{-\frac{K_1 V}{k_B T}} \qquad \text{Equation 1.1}$$

where $f_0 \approx 10^9 s^{-1}$ is a frequency constant, and k_B is Boltzmann's constant [6]. For the first 50 years of HDD history, longitudinal recording media was used for storing information. To meet the enormous demands for higher AD, researchers focused on the perpendicular magnetic thin film, as it has a much higher magnetic anisotropy and geometry advantage. Perpendicular recording technology was first proposed by Iwasaki *et al.* in the late 1970s [7-9], but it took 30 years for the industry to make the HDD based on the perpendicular recording available commercially. The first announced HDD based on perpendicular recording has a capacity of 80 gigabits (GB) [10]. After 15 years of development, in March 2020, most of the HDDs based on perpendicular recording has an information capacity of several terabits (TB). Up to date, we are very close to the single magnetic grain's superparamagnetic limitation, and new technologies are needed for increasing information capacity.

A promising technology for the next generation of HDD is heat-assisted magnetic recording (HAMR). This technology gives the magnetic recording a new degree of freedom: temperature, and Fig 1.2 shows a specific process of the HAMR writing. The recording material is heated by a focused laser beam, and with its temperature approaching to the Curie temperature the material's coercivity could have a significant drop. A much smaller magnetic field is needed for writing at that temperature. After the data were written, the media's temperature rapidly went back to the storage temperature. Hence, the higher magnetic anisotropy material can be used by adding a laser heating system. While according to the superparamagnetic limit equation, a higher magnetic anisotropy material could have a smaller grain size, which offers a higher AD. However, several challenges must first be addressed before the HAMR becomes a generalization commercial technology. For example, the recording materials' anisotropy should be not only large at room-temperature, but also quite sensitive to the temperature. After the material was heated by the laser, its anisotropy was reduced significantly. Also, the thermal conductivity of the disk should be taken into consideration. Furthermore, the light delivery system must deliver the laser efficiently from a laser diode to the recording media, and the focused spot size should be far smaller than the diffraction spot size. Therefore, designing a HAMR HDD needs system-level optimization. In February 2019, the HAMR HDD up to 24 TB was tested in the laboratory, and the next generation HAMR HDD is aiming for 40 TB by 2023 [11].

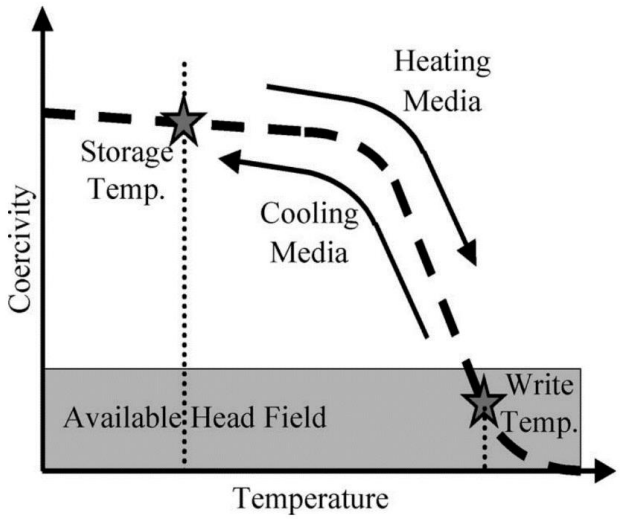

Figure 1.3 The schematic diagram of the HAMR writing process [12].

1.2 The Electron/spin dynamics

As the working frequency of magnetic recording approaches the GHz frequency regime, the electron/spin dynamic process at pico/femtosecond timescales attracts researchers' attention. In 1983, the picosecond laser-induced reflectivity transients of Cu were observed by the so-called time-resolved pump-probe technology, and the set-up used in this experiment is shown in Fig 1.4 (a) [13]. With the light speed of $3 \times 10^8\ m/s$, one-millimeter optical path difference of pump and probe pulse will give 3.33 picoseconds delay time. While the stepper motor's bidirectional repeatability is better than 1 micrometer, which shall give a time-resolution of 3.33 femtoseconds, much shorter than the ultrafast laser's pulse duration. This technology gives us the means to explore new insight into the electron and spin dynamics. The combination of time-resolved technique and magneto-optical imaging gives a time-resolved magnetic imaging system, which provides information on magnetic domain wall or vortex motion [14]. Details about the time-resolved pump-probe measurement will be given in chapter 3.2. Fig 1.4 (b) shows the temporal profile of the reflectivity changes representing anomalous rapid heating and cooling processes of the specimen, which is attributed to the electron and lattice thermal non-equilibrium state. Since photons only directly interact with electrons, and the laser pulse duration is much shorter than the electron-lattice relaxation time, this transient process could be observed by ultrafast laser. It is obvious in this graph that the electron-lattice's relaxation time is extremely short in metals.

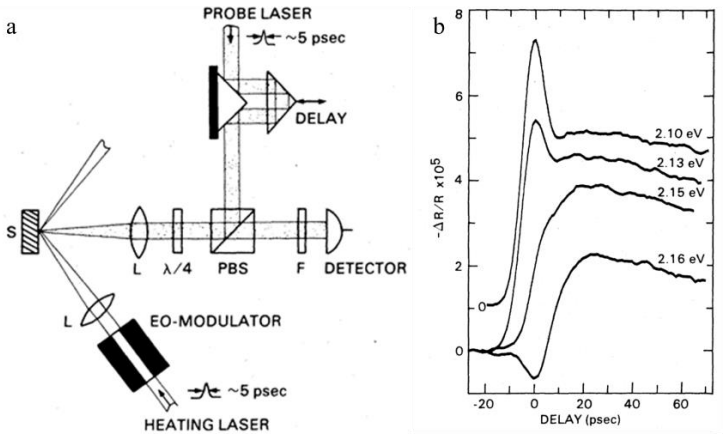

Figure 1.4 (a) An optical schematic of the time-resolved pump-probe experimental set-up. (b) Time-resolved $\Delta R/R$ transients for copper [13].

If we consider the magneto-optical interaction in the time-resolved pump-probe measurement, we could get the magnetic information at ultrafast timescales as well. The experimental set-up for

ultrafast magnetic measurement is just a bit more complicated than the normal time-resolved pump-probe set-up. Based on the time-resolved magneto-optical Kerr effect measurement, one could observe the spin-electron-lattice thermal non-equilibrium state as shown in Fig 1.5.

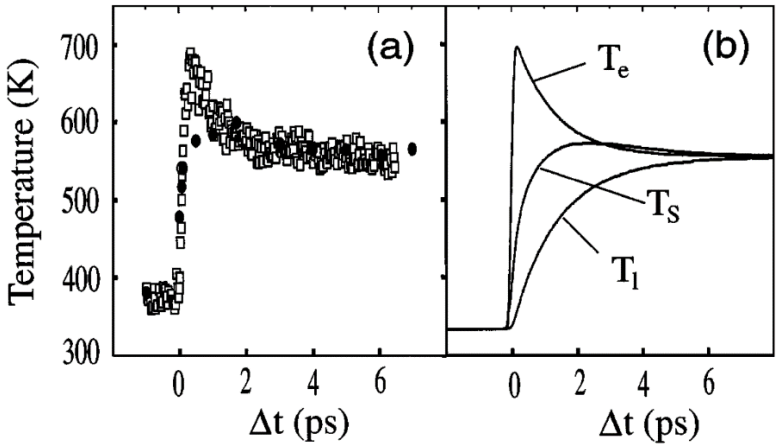

Figure 1.5 The temperature variation of electron (T_e, hollow squares) deduced from differential transmittance is plotted in(a), where the absolute electronic temperature scale is obtained by normalization to spin temperature (T_s, solid dots) measured by TR-MOKE. (b) Calculated spin (T_s), electron (T_e) and lattice (T_l) temperatures from three-temperature model [15].

To describe the dynamics process in Fig 1.5(a), Beaurepaire *et al.* introduced a new phenomenological three temperature model (3TM) [15]. This model is an extension of the modelization of the electron thermalization in metals called two temperature model [16]. The energy transfer of three systems is considered, including electron, spin, and lattice, and they are regarded as three energy reservoirs. The following differential equations show the relationship between temperature and the heat capacity of each system.

$$C_e(T_e)dT_e/dt = -G_{el}(T_e - T_l) - G_{es}(T_e - T_s) + \mathrm{P(t)},$$
$$C_s(T_s)dT_s/dt = -G_{es}(T_s - T_e) - G_{sl}(T_s - T_l), \qquad \text{Equation 1.2}$$
$$C_l(T_l)dT_l/dt = -G_{el}(T_l - T_e) - G_{sl}(T_l - T_s)$$

Here, C_e, C_s, and C_l are heat capacity and T_e, T_s, and T_l denote temperatures of electron, spin, and lattice, respectively. While the interactions of them are defined by the coupling parameters G_{es}, G_{el}, and G_{sl}. The first process when the magnet is exposed to the laser is the pure energy

transfer from the photon to the electron system, which is presented by the laser source term P(t) in the equation 1.2. Then the energy transfers from the electron system to the lattice and spin systems. This equation set allows us to extract a value of the electron-spin coupling strength of the sample from the magnetic dynamics. It is a major step to solving magnetic dynamic problems. More details about this topic will be discussed in chapter 2.5.1.

1.3 All-optical control of the magnetic direction

The interaction of photon and magnetic materials has been under intense investigation into its potential application in magnetic information storage. The transfer of energy and momentum from the photon to the electron is commonly known. But, the transfer of angular momentum was not unveiled until 2007, when Stanciu *et al.* demonstrated that laser could switch the magnetic direction in GdFeCo [17]. This helicity-dependent all-optical switching (HD-AOS) was considered as circularly polarized light simultaneously acting as a magnetic field so-called inverse Faraday effect (IFE). All-optical switching shows excellent potential for low-energy ultrafast spintronics since the energy density required for AOS is < 10 femto-Joules for a $(20\ \text{nm})^3$ cell, and the switching time is about ten ps, which is more than one order of magnitude faster than any magnetic field induced switching [18].

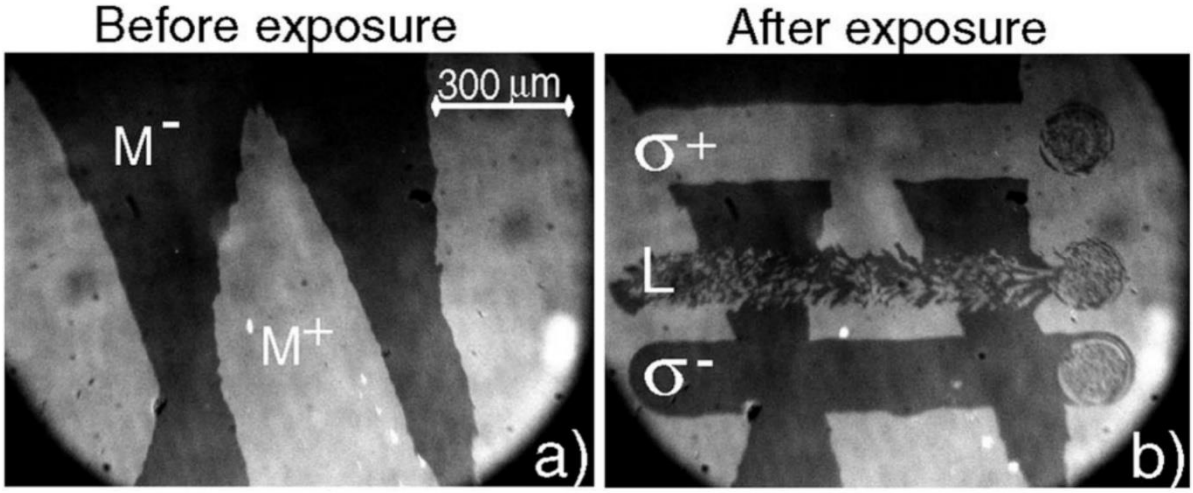

Figure 1.6 The landmark experiment observed all-optical switching in GdFeCo [17]. (a) Magneto-optical image of the initial magnetic state before exposure. (b) Three different polarized laser beams scanned across the sample from left to right with a speed of $30\ \mu m/s$. Here the right-handed circularly (σ^+) polarized beam switched the M^- to M^+, and the left-handed circularly

(σ^-) polarized beam switched the M^+ to M^-, while the linearly polarized beam remained in a multidomain state.

Hence, this phenomenon has widely attracted researchers' attention, and in the next few years, the range of material systems where AOS has been observed is continuously increasing. First, HD-AOS has been achieved in a number of rare earth-transition metal ferrimagnets [19]. Then, a transient ferromagnetic-like state was discovered in GdFeCo, which mediates the helicity-independent all-optical switching (HID-AOS) [20, 21]. Based on this discovery, AOS was achieved in Pt/Co/Gd stacks [22]. Then the material systems in which HD-AOS was observed were expanded to the ferromagnetic material, Co/Pt multilayer, in 2014 [23]. In the next few years, AOS has been widely investigated in these materials, as the interlayer exchange interactions spin-orbit coupling are considered to play an essential role in HD-AOS [24], and the optical spin-transfer torque is strongly enhanced by the Pt capping layer [25].

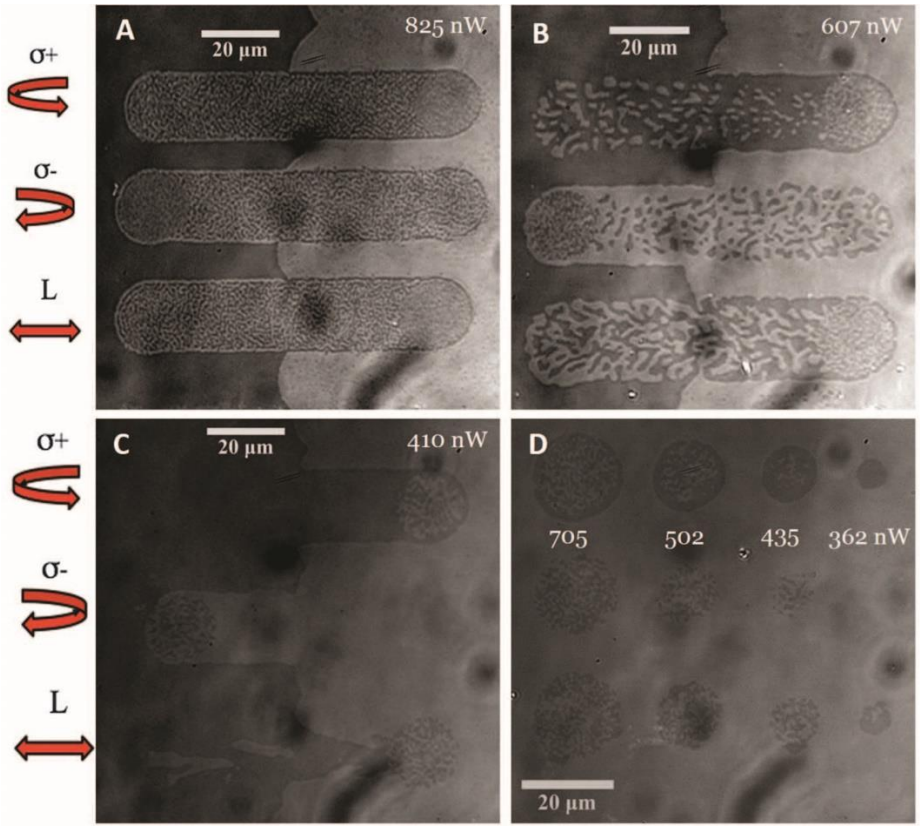

Figure 1.7 Magneto-optical images of helicity-dependent all-optical switching in $[Co/Pt]_N$ multilayer samples. Three different polarized laser beams scanned across the sample from left to right. (A) N = 8. (B) N = 5. (C) and (D) N = 3 [23].

Obviously, the HID-AOS mechanism is not applicable to HD-AOS. While the Fe and Gd spin sublattices in GdFeCo are antiferromagnetic coupling, all spins in ferromagnets are in the same direction. The most suggested mechanism for HD-AOS include the laser-induced heating [26, 27], magnetic circular dichroism (MCD) [28, 29], IFE [30-32], and optical selection rule [33]. MCD mechanism suggests that different magnetic states have different circularly polarized (CP) absorption ratios. For example, when the sample is illuminated by the left-handed circular polarized laser (LCP), the $M^{\uparrow}$ state's temperature is higher than the $M^{\downarrow}$ state as the former could absorb more LCP photons. That makes the probability of $M^{\uparrow} \rightarrow M^{\downarrow}$ higher than $M^{\downarrow} \rightarrow M^{\uparrow}$. According to a previous study, only 0.5% of MCD makes the AOS possible. IFE effect is more uncertain, the origin of IFE in the metal is still unknown, and it is very difficult to characterize experimentally [28]. Moreover, IFE is strongly materials and frequency-dependent [32]. Therefore

the amplitude and duration of the IFE field are treated as free parameters in simulations. As the AOS is at the picosecond scale, the effective magnetic field should be at 10 T scale. And the duration of at least 0.15 ps is necessary to achieve AOS in Co/Pt [30]. But AOS in Co/Pt is seen for a much shorter laser duration [23, 34]. In term of experimental observations of AOS, some questions are still open. First, for the circular polarized laser, heating and helicity effects are entangled. Overheating a ferromagnet only produces a random domain state. Heating it near its Curie temperature makes magnons easier to flip. Additionally, a temperature gradient was discovered to induce the domain wall drifting [35]. Hence, we could not identify the contribution of heating and helicity effect by using pure CP laser pulses. Second, up to data, HD-AOS is still a multi-pulse effect, therefore the most important information at picosecond scales in the HD-AOS process cannot get from time-resolved measurements.

1.4 Introduction to two-dimension materials

The two-dimensional (2D) materials first caught attention in 2004, when the carbon atom sheets stacked by the van der Waals forces were fabricated into 2D systems. The electrons in graphene show miraculous properties, including ballistic conduction [36], fractional quantum hall effect [37], Dirac point [38], and so on. Researchers soon found some of the properties do not rely on the carbon atom, but the 2D structure is more important, and many-layered materials have been mechanically exfoliated into monolayers. For example, transition metal dichalcogenides (TMDC), MX_2 (M=Mo, W; X=*S, Se, Te*), have the Dirac point and transit to a direct bandgap when they are down to monolayers [39]. The direct bandgap gives monolayer TMDCs a promising potential in future electronics. Devices such as photodetectors and transistors have been successfully fabricated [40-42]. The bandgap in monolayer TMDCs is in the visible light region. More than that, according to a recent study, the 2D TMDCs materials achieve one order of magnitude higher sunlight absorption than the most commonly used solar absorbers such as GaAs and Si [43].

The Dirac point in two-dimension (2D) materials gives the electron a new degree of freedom (DOF) called valley degree. Unlike graphene, the metal atom in TMDCs provides a strong spin-orbital coupling, and the inversion symmetry is broken in odd layer TMDCs. Both induce a spin-valley coupling in TMDCs Thus the spin and valley can be efficiently controlled by the optical helicity [44]. The direct interband transition results in an additional orbital magnetic moment at each valley,

and the conservation of angular momentum makes the transition between the valence band and the conduction band following the optical selection rule. Excited by the circularly polarized light, a non-equilibrium state valley current can be obtained, like the manipulation of the spin DOF. It is necessary to generate the valley-polarized current efficiently to operating the valley electronic devices.

In most 2D materials, the electron in the conduction band bottom is no longer can be considered as a single isolated electron. This is because in 2D materials, the dielectric screening is decreased enormously, and the effective masses of the electrons and hole near the Dirac point is much larger than in bulk materials [45]. For example, the electrons in graphene can interaction with each other, and that makes it a great stage to study the fractional quantum hall effect. Things get more complicated in 2D semiconductors, such as TMDC. This system exhibits tightly bound excitons, trions, and even intervalley biexcitons [46]. Furthermore, the first principle calculation based on density functional theory has shown that above the fundamental 1*s* exciton, monolayer TMDCs have densely spaced exciton states [47, 48].

Several measuring technologies are used to study the basic physical characteristics of 2D materials. The photoluminescence (PL) spectra shows that bulk MoS_2 with an indirect bandgap only has a negligible photoluminescence, while the monolayer MoS_2 has a strong photoluminescence emerges even in the room temperature [49]. The Raman shift also proves that TMDCs' band structure is strongly dependent on the number of layers [50]. Before long, time-resolved PL at 4 K shows that the trion in monolayer MoS_2 has a great contribution to the PL intensity, and the relaxation time of the trion is three times longer than the exciton [51]. As a potential valleytronic and spintronic material, the valley and spin relaxation time are the keys to the issue. PL gives the time scale of the electron and hole recombination as about 3 to 100 picoseconds. However, according to the time-resolved pump-probe experiment results, the electron spin relaxation time is longer than three nanoseconds at 5k in n-doped MoS_2 [52]. To directly explore the 1*s* intraexcitonic transient to n*p* in monolayer TMDCs, the researchers' in Korea developed a new technique called time-resolved mid-infrared spectroscopy, where the pump photon's energy is slightly higher than the A exciton, and the probe photon's energy is tuned to the transient energy [53]. Based on this technique, they discovered an intraexcitonic relaxation channel of 1*s* to 2*p* and an even higher-order transition was observed at a higher temperature.

Most of these monolayer materials have the same lattice structures, heterostructure, and they can be assembled with each other by van der Waals force. The orientations of each layer are confirmed by second harmonic generation measurements [54, 55]. The properties of these monolayer crystals have slight differences, and when they are coupled only by van der Waals forces, the interaction between them will induce phenomena that are absent in individual layers. In 2015, the researchers in the USA studied the phonon mode in MoS_2 / WSe_2 and $MoSe_2$ / MoS_2, and the layer-breathing mode vibration between the two TMDC monolayers was founded by the Raman spectroscopy [56]. Since the Raman measurement is a basic technology, this research provides a convenient and useful probe to the van der Waals heterostructures. The lifetime of spin/valley polarization in monolayer TMDCs is no longer than several nanoseconds. However, time-resolved PL spectra show the spin/valley relaxation time in WSe_2 / $MoSe_2$ is 40 nanoseconds, and this long-lived polarization is tunable by the gate voltages [55]. In 2016, time- and angle-resolved photoemission was used to directly measure the transient band structure evolution in van der Waals-bonded graphene and MoS_2 heterostructure [57]. The results confirmed that after the first laser pump pulse, the bandgap is reduced by up to about 400 meV on several femtoseconds. Beyond that, when the pump photon energy is lower than the bandgap, the higher-order multiple photon processes were observed, and this result seems related to our new result since we also have the negative reflection in monolayer $MoSe_2$ as well. These results are equally possibly come from the dark exciton, which has been confirmed by the two-photon PL excitation [58, 59].

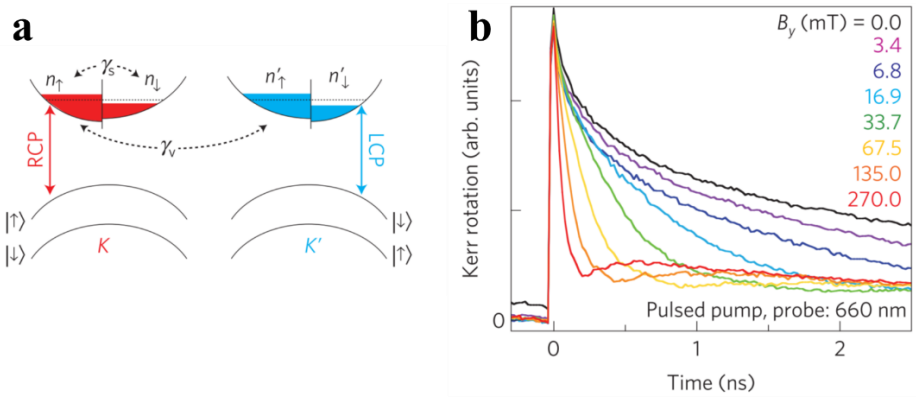

Figure 1.8 (a) A simple bandstructure picture of the conduction and valence bands at the K and K' valleys of monolayer MoS2, along with the relevant optical selection rules and scattering processes.

(b) Nanosecond spin relaxation time in $MoSe_2$ was detected by the time-resolved Kerr rotation [52].

Researchers are not limited to graphene and TMDCs, and plenty of 2D materials with incredible properties have been exfoliated from bulk. For example, monolayer CrI_3 are demonstrated 2D ferromagnetism, and it has layer-dependent magnetic phases, which is the first revealed isolated 2D magnets [60]. Before long, CrI_3 and WSe_2 bond to create new van der Waals heterostructures, and a large magnetic exchange field of nearly 13 T was found in this material [61]. Transition metal carbides (TMC), produced by exfoliation of Ti_3AlC_2, have also joined the 2D family in 2011 [62]. Bulk Mo_2C was found to have superconductivity in 1966 [63], and monolayer Mo_2C also has superconductivity [64]. Black phosphorus is stacked together by Waals interaction as well. Thus, monolayer black phosphorus was fabricated into a transistor in 2014, and its electrical mobility is found to be layer-dependent [65]. These two 2D materials are just like bricks with different properties. With more 2D materials found, researchers can create more devices with unique characters to satisfy different requirements.

1.5 Synthetic antiferromagnetic materials

As human civilization needs to store and process information continuously increases, the main objective of spintronics is to reduce device power consumption and scale. However, the limit of current memory and process devices will be approached soon, and much more magnetic interactions will enter the researchers' scene, as they may provide a new degree of freedom for controlling or detecting magnetic properties. Such as using the Dzyaloshinskii-Moriya interaction to control domain-wall motion [66], switching the magnetic direction by the spin-transfer torque [67-69] or spin-orbital torque [70-72], and tuning the interlayer exchange coupling by electrical field [73-75].

With more important interactions being discovered in antiferromagnetic materials, antiferromagnetic spintronics has become a fast-growing, cutting-edge field in spintronics. The storing and the magnetoresistive read element are merged into one in magnetic random-access memory (MRAM) [76], and the stray magnetic field is not even used in the spin-torque [69] or spin-orbital torque MRAM [77, 78]. Unlike traditional ferromagnetic spintronics, antiferromagnetic spintronics has no stray magnetic field and, therefore, a much higher magnetic

field stability [79]. Synthetic antiferromagnetic (SAF) multilayer is one of the easiest ways to manipulate antiferromagnetic (AFM) coupling [80]. Two ferromagnetic (FM) layers are separated by a nonmagnetic (NM) spacer layer, and there is an indirect interaction through the NM layer called the interlayer exchange coupling. The interlayer exchange coupling is easily tuned by the spacer layer's thickness [81], and the interaction can be changed from ferromagnetic coupling to antiferromagnetic coupling. As shown in Fig 1.7, the oscillation interlayer coupling is not limited to metallic layers [82, 83] but also to nonmagnetic layers [81, 84].

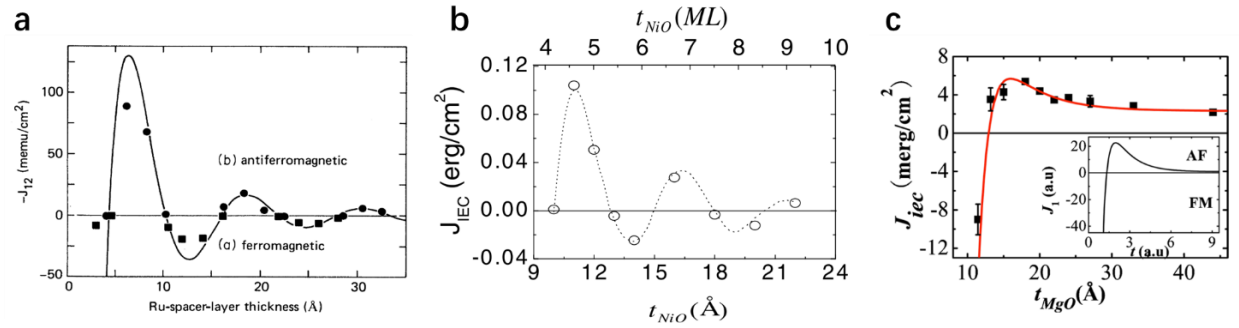

Figure 1.9 The dependence of the interlayer exchange coupling strength on the spacer thickness. (a) Metallic spacer layer Ru [85]. (b) Antiferromagnetic spacer layer NiO [84]. (c) Insulating spacer layer MgO [86].

In recent years, electric-field regulation has replaced magnetic field control due to its high speed and energy efficiency. When the spacer layer is metallic, the interlayer exchange coupling is described by the Ruderman-Kittel-Kasuya-Yosida (RKKY) interaction theory [87-89]. Controlling RKKY interaction by electric field was discovered in 2018 by Qu Yang *et al.* [90]. But for other spacer layers, electric field controlling is not achieved yet. Manipulating all the interlayer exchange couplings becomes a new challenge. With the regulation of antiferromagnetism gaining increasing attention, more methods with higher speed, more compact and higher energy efficiency will be found.

1.6 Thesis overview

The study presented in this thesis focuses on the study of magneto-optical interaction in various magnetic materials. The crucial experimental results are using the ultrafast laser to investigate the

magnetic dynamics, which deals with nonequilibrium physical process on a femtosecond time scale. To explore the underlying mechanism and the microscopic nature of the magnetic properties, the first-principle calculation is used to reveal the static properties of samples used in this thesis. The calculation results have two parts. The first part is the magnetic moment distribution on each layer of multilayer samples. The second term is the spin-orbital coupling of different atoms, as this parameter plays a key role in the magneto-optical interaction. The basic magnetic characterizations are also performed, including magneto-optical Kerr imaging and vibrating sample magnetometer. The results provide new physical insight to better understand the all-optical switching mechanism and manipulate the magnetic direction by using an ultrafast laser pulse.

In chapter 1, a brief introduction and basic background of the ultrafast spin and electron dynamics have been presented. Three sub-fields are introduced, including a brief review of the magnetic recording, all-optical switching and the two-dimension materials.

The theoretical background of magnetism was presented in chapter 2. Magneto-optical interactions are introduced, including ultrafast laser-induced heating effect, Kerr and Faraday effects, magnetic circular dichroism, and inverse Faraday effect. The ultrafast laser heating effect plays an irreplaceable role in explaining the magnetization dynamics. The Kerr and Faraday effects provide us with tools to measure the magnetic properties. The magnetic circular dichroism and inverse faraday effect are the two most discussed candidates to explain the mechanism of all-optical switching. Finally, the first principle calculation is briefly introduced.

In chapter 3, all the experimental techniques used in this thesis are introduced. Three conventional characterization techniques are introduced, including a magneto-optical Kerr effect image system, time-resolved pump-probe spectroscopy and vibrating sample magnetometer. A new experimental setup designed to figure out the heating and helicity effects in the all-optical switching is also included, and details are discussed in chapter 3.3. Since all the samples were grown by magnetron sputtering, this growth technique was introduced in chapter 3.4.

Although helicity dependent all-optical switching (HD-AOS) in ferromagnetic materials was discovered in 2014, its microscopic physical picture of it is still under hot debate. In chapter 4, several new experiments were designed, combining the magneto-optical Kerr image system and the time-resolved pump-probe system. The experimental results provide a new physics insight into

this field. The sample used in this chapter is a simple but of fundamental importance, Pt/Co/Pt multilayer structure, which is the first ferromagnetic material that observed all-optical switching [23]. To explore the contribution of the heating effect in HD-AOS, linearly polarized and circularly polarized laser pulses were used. Several energy combinations and different pulse delay time were tested. The results suggested that the heating effect could significantly assist helicity dependent all-optical switching, and the phenomenological magnetic circular dichroism was identified as the mechanism [28] responsible for the observed HD-AOS in Pt/Co/Pt multilayer structures.

Chapter 5 focuses on improving the energy efficiency and switching ratio for HD-AOS. High-quality Pt/Co/Pt multilayer thin films were growing by magnetron sputtering at the same growth condition with different Pt and Co thicknesses. The all-optical switching power and switching ratio were studied in all the samples. The first-principle results and the experimental results are compared to further understand the all-optical switching. The Pt layer was found to enhance the spin-orbital coupling of its nearby Co layer and, therefore, improved the switching ratio. However, the high reflectivity of the Pt layer increased the energy consumption of all-optical switching.

Chapter 6 presents the spin dynamics in synthetic antiferromagnetic materials investigated by the time-resolved magneto-optical Kerr effect measurement. Three series samples with the same structure FM/Spacer layer/FM and three different spacer layers (MgO, NiO, Ru) were studied. By changing the thickness of the spacer layer, the interlayer exchange coupling can be tuned from ferromagnetic coupling to antiferromagnetic coupling. The transient hysteresis loops provide a direct opportunity to study the interlayer exchange coupling. The results pave the way to manipulating the interlayer exchange coupling by ultrafast laser pulses.

In the last chapter, two future works are presented that are based on the new findings and methods in this thesis.

Chapter 2 Theory

2.1 Overview

According to modern physics, magnetism providers in the atomic scale can be divided into two categories: First, elementary particles, including electrons, protons, and neutrons, have the spin magnetic moment. This concept was first introduced by Wolfgang Pauli in 1924 to explain the fine structure of the emission spectrum of alkali metals [91]. Even today, we still cannot answer the question of why these small particles could produce such an enormous magnetic field but describe it as an intrinsic property. It does not prevent us from using and developing a great variety of magnetic materials. Second, the electron's orbital motion in the atom provides the orbital moment, and the proton's and neutron's motion in the nucleus also provides a small magnetic moment. When atoms or molecules compose materials, those magnetism providers have multiple interactions with each other, which is the origin of magnetic materials. Here we introduce several important magnetic interactions related to this thesis, including exchange coupling, spin-orbit coupling and Zeeman interaction. Also, the interaction between light and magnetic materials is the most attractive part of spintronics. One will expect many applications if the light could control the magnet. However, the interaction of the light and the magnet is very complex, many effects should be considered, and the microscopic mechanisms of opto-magnetic effects are still missing. Although the light is an electromagnetic wave, the interaction between the light and the magnet is extremely weak, which also makes it quite tough to study. Through researchers' many decades' efforts, we now know more details about the magneto-optical interactions, and we will introduce several of them that were used in our research.

2.2 Exchange coupling

Most of the gas, liquid and solid are paramagnetic materials, which obey Curie's law. It is described as the magnetization of the material is proportional to an applied magnetic field and inversely proportional to temperature, which can be presented as:

$$M = C\frac{B}{T} \qquad \text{Equation 2.1}$$

However, people found some materials present very strong magnetization even without an applied magnetic field, and they are referred to as ferromagnetic materials. Pierre Weiss made a correlation to the Curie's law and expanded it to ferromagnet, called Curie-Weiss' law:

$$M = C\frac{B}{T-T_c} \qquad \text{Equation 2.2}$$

where T_c is called the Curie temperature. Above this temperature, the material could be regarded as paramagnet, and below this temperature the ferromagnet has a spontaneous magnetization. Weiss introduced a molecular field in the ferromagnet to explain spontaneous magnetization in 1907 [92], which has an astonishing scale of 10^7 T. However, the origin of the molecular field is not explained until the development of quantum mechanics. After that, this field is described as the exchange coupling. The spin-spin exchange interaction is the most important coupling in magnetism, which is responsible for the magnetic order. The exchange coupling is a short-range interaction between electrons, which is the strongest magnetic interaction. It aligns the spin system to parallel or antiparallel depending on the exchange energy, while the former gives ferromagnetic coupling and the later gives antiferromagnetic coupling. The exchange coupling induced energy splitting was first observed in the *He* spectrum, which is the easiest but perfect model to explain magnetism in quantum mechanics. To understand the origin of exchange coupling, here we figure out why the helium energy of the spin system's antiparallel alignment is higher than its parallel alignment. The Hamiltonian of this system under Born-Oppenheimer approximation could be presented as:

$$H(r_1, r_2) = \frac{p_1^2}{2m_e} + \frac{p_2^2}{2m_e} - \frac{2e^2}{4\pi\epsilon_0|r_1|} - \frac{2e^2}{4\pi\epsilon_0|r_2|} + \frac{e^2}{4\pi\epsilon_0|r_2-r_1|} \qquad \text{Equation 2.3}$$

Where r_1, r_2 are the electrons' position, and p_1, p_2 are the electrons' momentum. Here the first 4 terms are the central field part, which could be treated as the zero-order Hamiltonian $H^0(r_1, r_2)$. While the last term gives the electron-electron interaction, which is treated as a perturbation $H^1(r_1, r_2)$. We start from the wavefunction of $H^0(r_1, r_2)$, since electrons are Fermions, the wavefunction of this system should be antisymmetric. Therefore, the wavefunction for parallel spin alignment is:

$$\Psi^P(a, b) = \frac{1}{\sqrt{2}}[\psi_1(r_1)\psi_2(r_2) - \psi_1(r_2)\psi_2(r_1)]\chi_p(s_1, s_2) \qquad \text{Equation 2.4}$$

Here the space part is antisymmetric. While the wavefunction for antiparallel spin alignment is:

$$\Psi^A(a,b) = \frac{1}{\sqrt{2}}[\psi_1(r_1)\psi_2(r_2) + \psi_1(r_2)\psi_2(r_1)]\chi_A(s_1,s_2) \quad \text{Equation 2.5}$$

Here, the space part is symmetric. Then, according to the perturbation theory, we obtain the energy correction due to electron-electron interaction:

$$E^P_{e-e} = \langle\Psi^P(a,b)|H^1(r_1,r_2)|\Psi^P(a,b)\rangle = I - J \quad \text{Equation 2.6}$$

for parallel alignment. And

$$E^A_{e-e} = \langle\Psi^A(a,b)|H^1(r_1,r_2)|\Psi^A(a,b)\rangle = I + J \quad \text{Equation 2.7}$$

for antiparallel alignment. We, therefore, get the exchange coupling induced energy shift:

$$E^A_{e-e} - E^P_{e-e} = 2J \quad \text{Equation 2.8}$$

The energy J has a simple physical explanation that is the energy related to the two electrons exchanging their quantum state. When J is positive, it leads to parallel spins, which is the case in *He*. When J is negative, it leads to antiparallel spins, which is the case in H_2.

2.3 Spin-orbit Interaction

Spin-orbit interaction plays an irreplaceable role in magnetism as it is the coupling between electrons and lattice, and therefore, it induces magnetocrystalline anisotropy when atoms compose crystals. The interaction induced energy splitting was first observed in the optical emission spectra, so-called the fine structure, and researchers found this energy splitting increase with the atomic number Z. Here, we introduce the spin-orbit coupling by using a semiclassical model with a spin $\boldsymbol{S}$ and an orbital momentum $\boldsymbol{L}$. According to the Biot-Savart Law, a magnetic field is generated by an electrical current. The electron orbital motion can be regarded as a current $\boldsymbol{I} = -\frac{e\boldsymbol{L}}{2\pi m_e r^3}$, and its magnetic field can be presented as:

$$\boldsymbol{H}_{orbit} = -\frac{e\boldsymbol{L}}{4\pi m_e r^3} \quad \text{Equation 2.9}$$

Here e is the electron charge, m_e is the electron mass, and r is the distance between the nucleus and the electron. Then the spin *S* in this field has an energy of:

$$E_{so} = -\frac{e^2}{4\pi\epsilon_0 m_e^2 c^2 r^3} \boldsymbol{S} \cdot \boldsymbol{L} \qquad \text{Equation 2.10}$$

From quantum mechanics, the spin-orbit interaction Hamiltonian is given by the following equation:

$$H_{so} = \xi_{nl}(r) \boldsymbol{s} \cdot \boldsymbol{l} \qquad \text{Equation 2.11}$$

Here the *n* is the principal quantum number and *l* is the angular quantum number, and the expectation value of $\xi_{nl}(r)$ is called the spin-orbit parameter ($\zeta_{nl} = \langle \xi_{nl}(r) \rangle$) with dimension [energy]. Spin-orbit interaction is about 10-100 times smaller than the exchange interaction, and from equation 2.11 we know it is related to both principal and angular quantum numbers. For the atoms like H and He, the spin-orbit interaction energy is about $5 \times 10^{-5}\, eV$, but for the 3d electrons in Co and Fe, this energy has a magnitude of $1 \times 10^{-2}\, eV$, while for the 4f electrons in rare earth elements like Gd, it is about 0.1 *eV*, and 5d electrons in Pt, it is about $0.8\, eV$.

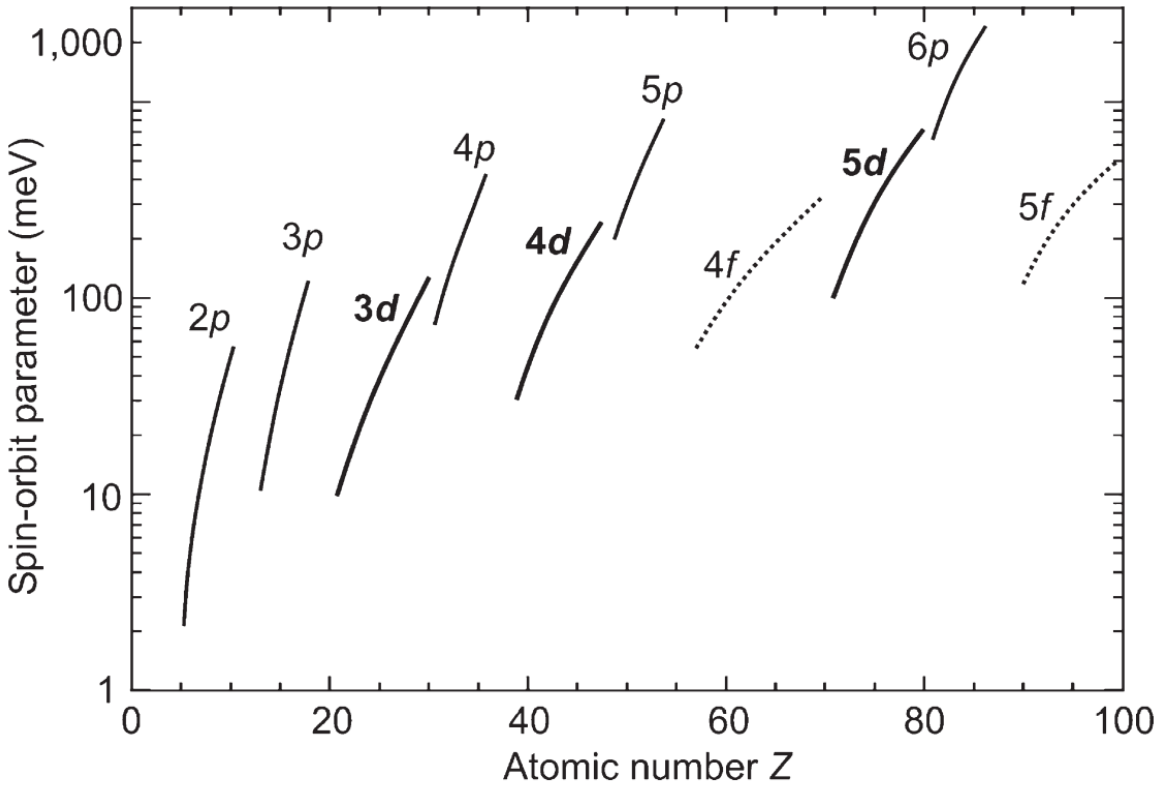

Figure 2.1 The spin-orbit parameter ζ_{nl} for the valence shells of neutral atoms in their ground state. These parameters are calculated by Cowan by using the relativistic Hartree-plus-statistical-exchange method [93].

2.4 The magnetic anisotropy

Magnetic anisotropy is an experimental concept which includes magnetocrystalline anisotropy, shape anisotropy, and surface-induced magnetic anisotropy. It is the energy that takes to rotate the magnetization direction from the magnetic easy axis to the hard axis, which can be characterized by a polar vector. The uniaxial anisotropy is the most common magnetic anisotropy, which has a single magnetic easy axis. And its anisotropy free energy density is expressed as [94]

$$E_{\text{ani}} = K_1 + K_2 \sin^2\theta + K_3 \sin^4\theta + \cdots \qquad \text{Equation 2.12}$$

here θ is the orientation of magnetization with respect to the easy axis, and K_1, K_2, K_3,…, are the anisotropy constants.

We now explain why the spin-orbit interaction determines the magnetocrystalline anisotropy in solid. The physical meaning of the spin-orbit interaction energy is the energy needed to turn the

spin $\boldsymbol{S}$ from a perpendicular to a parallel orientation to the orbit moment $\boldsymbol{L}$. The treatment of the spin-orbit coupling in the previous section is based on a single atom. In this condition, for example, the energy of 3d orbits is degenerate. But the situation in condensed matters is much different, the orbital moment may prefer to lie along a specific direction due to crystal structure [95], a specific bonding [96, 97], or the interface effect [98], which is called the anisotropy of the orbital moment. In 1989, Patrick Bruno showed that the anisotropy of the spin-orbit energy is directly related to the anisotropy of the orbital moment under the tight-binding approach [99]. The Bruno model can be expressed by the following equation:

$$\Delta E_{so} = \zeta\left[\langle \boldsymbol{L}\cdot\boldsymbol{S}\rangle_{easy} - \langle \boldsymbol{L}\cdot\boldsymbol{S}\rangle_{hard}\right] = \frac{\zeta}{4\mu_B}\left(m_o^{easy} - m_o^{hard}\right) > 0 \qquad \text{Equation 2.13}$$

here m_o^{easy} (m_o^{hard}) is the orbital moment along the easy (hard) magnetization direction. This equation gives us a particularly important insight that the easy axis has a larger orbital moment than the hard axis, and the difference is proportional to the magnetocrystalline anisotropy. In 1995, D. Weller *et al.* confirmed this theoretical prediction by using the high-field, angle-dependent x-ray magnetic circular dichroism measurements [100].

2.5 Zeeman interaction

Zeeman interaction was named by Dutch physicist Pieter Zeeman, which was first observed in the spectral lines split into multiple closely spaced lines in the presence of a static magnetic field. These results were then explained by the quantum mechanics. The external magnetic field $\boldsymbol{H}$ exerts a torque on a magnetic dipole, and the Hamiltonian corresponding to the Zeeman energy can be expressed as [101]

$$H_{Zeeman} = -\int_V \boldsymbol{M}\cdot\boldsymbol{H}d^3\boldsymbol{r} \qquad \text{Equation 2.14}$$

Considering the quantization of the total magnetic momentum, including the spin and orbital parts:

$$\boldsymbol{M} = -\mu_B(\boldsymbol{l} + 2\boldsymbol{s})/\hbar \qquad \text{Equation 2.15}$$

In order to compare the Zeeman interaction with other interactions, we consider the applied magnetic field along z-axis and the simple case when $l = 1$ and $s = 1/2$ and therefore, we have:

$$\langle H_{Zee}\rangle = 2\mu_B H = 2\frac{\mu_B}{\mu_0}B \qquad \text{Equation 2.16}$$

Here $\mu_B = \frac{e\hbar}{2m_e} = 5.788382 \times 10^{-5} eV/T$ is the Bohr magneton. And therefore, the estimated Zeeman energy has a typical size of $\sim 0.1\ meV$ when the field is 1 Tesla, which is much smaller than the exchange coupling and the spin-orbital coupling. But the Zeeman interaction is the only energy term directly determined by the external field.

2.6 Magneto-optical interaction

Although the interaction between photons and magnetic materials is fiendishly complicated, many researchers have made a massive effort to clarify it. Up to date, many magneto-optical interactions have been discovered, including Kerr effect, Faraday effect, magnetic circular dichroism, magnetic linear dichroism, optical transition selection rules and so on. Even though some of their fundamental physical pictures are still under debate, there is no doubt that those findings gave birth to a wealth of techniques to detect and manipulate magnetism and therefore pushed the development of magnetism. In this section, we will introduce several magneto-optical interactions that closely relate to the research of this thesis.

2.6.1 Heating effect

The heating effect is normally not considered as a magneto-optical interaction. However, for the all-optical switching, the heating effect becomes nonnegligible. As we mentioned in Chapter 2.2, the magnetization and coercivity decrease with the temperature increases. This phenomenon is used in the commercial hard disk, which increases the capacity of storing information. With the development of the ultrafast laser, the ultrafast laser-induced ultrafast demagnetization also attracted many researchers' attention. Ultrashort heating is radically different from standard heating as it could produce a non-equilibrium magnetic state, as shown in Fig. 2.2 (a), (b). Since the temperatures of spin, electron and lattice are no longer the same, this non-equilibrium state cannot easily be described by the Curie-Weiss law, but a new basic mechanism is required. As early as 1991, Vaterlaus *et al.* discovered the demagnetization time of gadolinium is about 100 ps [102]. A few years later, Beaurepaire *et al.* found a significant faster demagnetization time on a nickel thin films, within 1 ps, as shown in Fig 2.2 (c) [15].

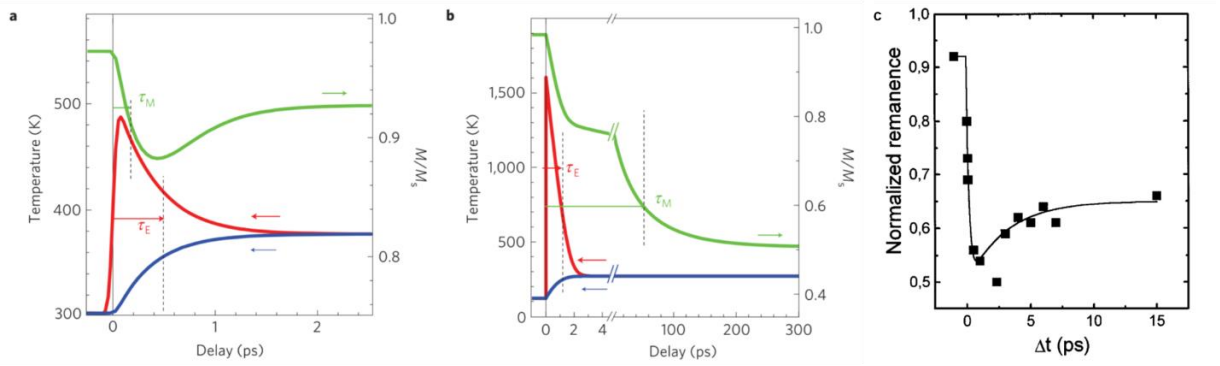

Figure 2.2 (a) Simulating ultrafast laser-induced demagnetization for Ni-based on the M3TM theory. Here the red line presents the electron temperature $T_e(t)$, blue line presents the lattice temperature $T_l(t)$, and green line is the ultrafast demagnetization $m(t)$. (b) The similar result for the Gd *[103]*. (c) Transient remanent longitudinal magneto-optical Kerr effect (MOKE) signal of a Ni($20\ nm$)/MgF_2($100\ nm$) film for $7\ mJ/cm^2$ pump fluence [15].

This paradoxical phenomenon was successfully explained by Koopmans in 2009 [104]. They took the Elliot-Yafet-like spin-phonon flip processes into account and expanded the phenomenological three temperature model (3TM) [15, 105]. This new microscopic 3 temperature model (M3TM) can be expressed by the following differential equation:

$$\frac{dm}{dt} = Rm\frac{T_p}{T_C}\left(1 - m\coth\left(\frac{mT_C}{T_e}\right)\right) \qquad \text{Equation 2.17}$$

Just like the ordinary 3TM, T_p is the phonon temperature, T_e is the electron temperature, T_C is the Curie temperature, and $m = M/M_s$ is the magnetization relative to its value at zero temperature, where R is a materials-specific scaling factor. This concise and elegant equation predicts a wide variety of magnetic dynamic features. About the demagnetization, rapid demagnetization will be observed at low laser fluence. With the laser fluence increasing, the demagnetization is stronger but slower. And the recovery of the magnetization also has the same tendency.

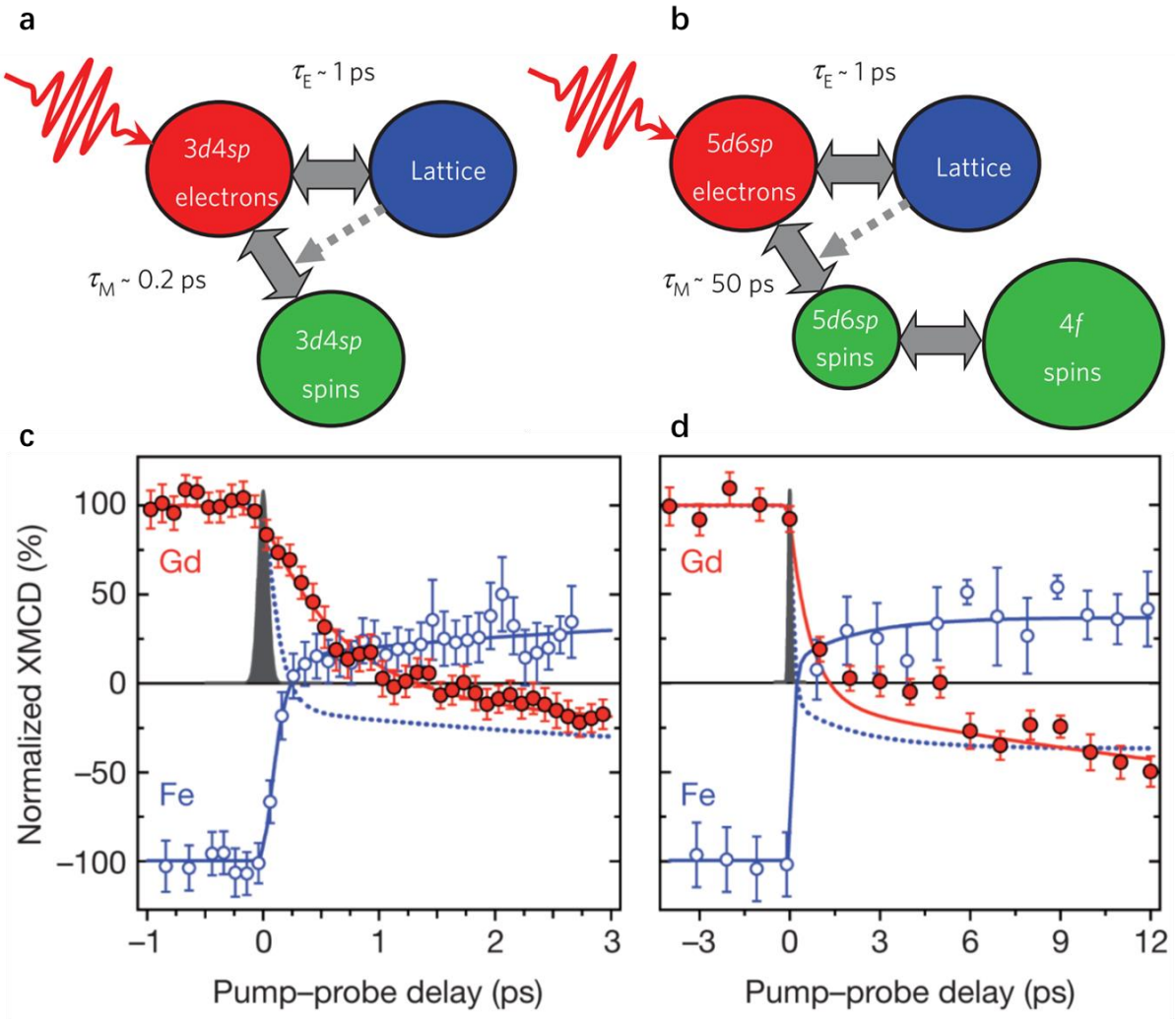

Figure 2.3 (a) ultrafast demagnetization process on the 3d transition metals. (b), Similar to the extra 4f system *[103]*. (c) and (d), Element-resolved dynamics of the Fe and Gd magnetic moments measured by time-resolved X-ray magnetic circular dichroism (XMCD) with femtosecond time-resolution. c, transient dynamics of the Fe (blue open circles) and Gd (red filled circles) magnetic moments measured with the first 3 ps. d, As c but on a 12 ps timescale [20].

The explanation of the single-pulse HID-AOS in GdFeCo is based on the observation that demagnetization time for Gd's 4f electrons (about 1.5 ps) is about five times slower than that of Fe's 3d electrons (about 300 fs) [20]. As shown in Fig 2.3 (a) and (b), photons directly interact with the electrons near the Fermi level. The electron's temperature rockets to the peak within 1 ps no matter it is the 3d, 4p or 5d, 6s electron. The lattice temperature increases by the hot electrons

scattering process with a time scale of ~1 ps. As the interaction between lattice and electrons at different orbits has no differences, these two processes have no significant timescale difference. However, the coupling between the electron and spin systems strongly depends on materials. For the transition metals like Co, Ni, and Fe, spin polarized electrons, 3d electrons, could directly interact with photons, and therefore, the coupling between electron and spin is much stronger. The situation for rare-earth elements is much different. The 4f electrons are spin polarized, but they cannot interact with photons but with the 5d, 6s electrons' spin, this indirect coupling is much weak, and the time constant for these elements is ~50 ps. Due to the difference in the demagnetization speed, the ultrafast demagnetization in GdFeCo is different from normal materials. Once the laser pulse arrived, the Fe's fully demagnetization occurs within 0.5 ps, and then it was re-magnetized by the Gd sublattice, and then the ferrimagnet material GdFeCo was at a transient ferromagnetic state.

The HID-AOS was not found in any other materials without Gd until 2019. As shown in Fig. 2.4, the pure thermal single-pulse switching was discovered again in the ferrimagnetic Heusler alloy Mn_2Ru_xGa *(MRG),* which proves that HID-AOS is not limited to Gd based amorphous ferrimagnet films [106], and the mechanism in MRG is rather different. There are two sublattices with opposite spin directions called Mn (4a) and Mn (4c). The 4a sublattice has a stronger intrasublattice exchange interaction and a weaker easy axis. While the DOS of 4c is greater at the Fermi level and a maximum in the unoccupied density of states about 1.2eV above the Fermi level according to the first-principles calculation, which leads to a faster demagnetizing [107]. The 4a sublattice is fully demagnetized after being exposed to the 800 nm (1.55 eV) laser pulse, and the 4c sublattice's angular momentum is transferred to the 4a sublattice leading to a transient ferromagnetic state just like the AOS process in the GdFeCo. Finally, with the spin ordering recovered, the stronger easy axis in the 4c will force the 4a's spin flips. This finding proves that HID-AOS can be achieved by not only the difference of demagnetizing time for 4f and 3d electrons but also the coupling strength of two sublattices, which significantly widen the basis for AOS and break new ground for engineered materials used for AOS.

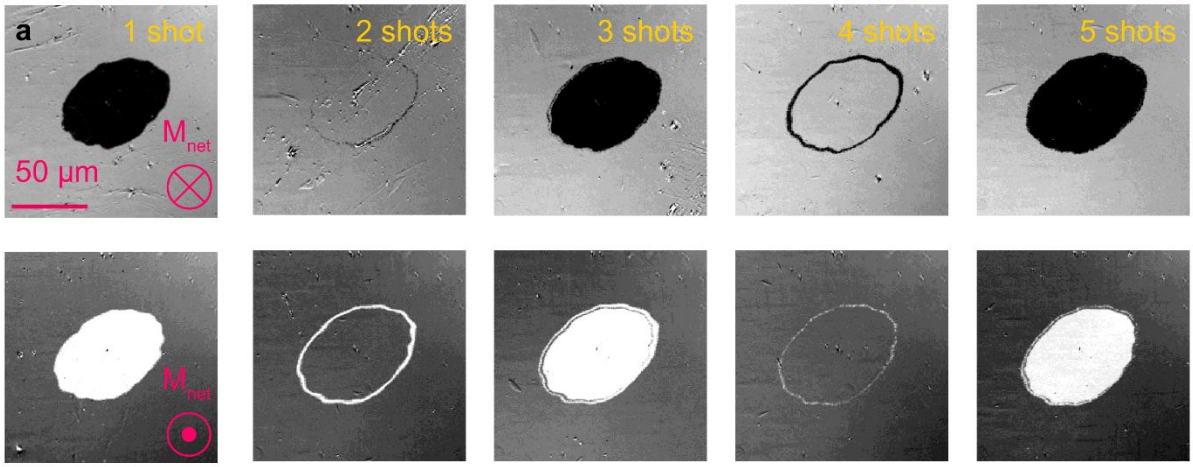

Figure 2.4 Single linearly polarized laser pulse induced all-optical toggle switching in Mn_2RuGa. This MRG sample has a compensation temperature above room temperature. The laser pulse used here has a 200 fs duration and 800 nm wavelength *[106]*.

2.6.2 Kerr-Faraday effect

Although light is an electromagnetic wave, the interaction between light and magnetic field was not discovered until 1845. Michael Faraday found that when a beam of linearly polarized light passes through the glass under an applied magnetic field, its polarization axis is rotated. This experiment was the first evidence that there is an interaction between light and the magnetic field. Thirty-two years later, John Kerr found that when linearly polarized light reflects from a magnetic material, its polarization axis is rotated. Nowadays, the magneto-optical effect's transmission part and reflection part are called the Faraday effect and Kerr effect, respectively. These effects can be phenomenologically described by the dielectric law:

$$\boldsymbol{D} = \varepsilon(\boldsymbol{E} + iQ\boldsymbol{m} \times \boldsymbol{E}) \qquad \text{Equation 2.18}$$

where $\boldsymbol{E}$ is the electrical vector of the incident light, $\boldsymbol{m}$ is the magnetization vector and Q is the complex magneto-optical constant, which is introduced in the permittivity tensor:

$$\varepsilon = \varepsilon_q \begin{bmatrix} 1 & -iQm_z & iQm_y \\ iQm_z & 1 & -iQm_x \\ -iQm_y & iQm_x & 1 \end{bmatrix} \qquad \text{Equation 2.19}$$

here m_x, m_y, m_z are the magnetisation components along the x, y, and z axes, respectively. From this equation, we get the reflection light amplitude, the $\boldsymbol{D}$ vector, which is related to the

magneto-optical interaction of the incident light amplitude $\boldsymbol{E}$ with the sample's magnetization vector $\boldsymbol{m}$, and it can be regarded as secondary light amplitude. The magneto-optical constants of the Cu/Co multilayers at a wavelength of 6328Å is $Q = 0.0177 - 0.0063i$ and $Q = 0.00038 - 0.00315i$ for Co/Pd multilayers [108]. A key point for experimental setup and measurement is the cross product of $\boldsymbol{E}$ and $\boldsymbol{m}$, and we shall discuss this part in Chapter 3 and Chapter 6.

Then we derivate the equation of the Kerr rotation and Kerr ellipticity from the Fresnel equation. As the Kerr effect is about the change of the light's polarization, the s- and p-polarized light are separately considered in the Fresnel equation. Here we present this equation as follows:

$$\begin{pmatrix} E_{rs} \\ E_{rp} \end{pmatrix} = \begin{pmatrix} r_{ss} & r_{sp} \\ r_{ps} & r_{pp} \end{pmatrix} \begin{pmatrix} E_{is} \\ E_{ip} \end{pmatrix} \qquad \text{Equation 2.20}$$

Here E_{rs} and E_{is} (E_{rp} and E_{ip}) present the reflected and incident light's electric field vector's component on the s-polarized (p-polarized) direction, respectively. Where r_{ss}, r_{sp}, r_{ps}, and r_{pp} are the Fresnel reflection coefficients and the subscripts denote the scattering plane dependence of each element such that r_{ps} represents the ratio between the complex electric field amplitude of p-polarised reflected light and that of s-polarised incident light. Expression of the Fresnel reflection coefficients can be calculated by applying the reflection boundary condition [109]:

$$r_{ss} = \frac{\mu_2 N_1 \cos\theta_1 - \mu_1 N_2 \cos\theta_2}{\mu_2 N_1 \cos\theta_1 + \mu_1 N_2 \cos\theta_2} \qquad \text{Equation 2.21}$$

$$r_{sp} = \frac{i\mu_1\mu_2 N_1 N_2 \cos\theta_1 Q(m_x \sin\theta_2 - m_z \cos\theta_2)}{(\mu_1 N_2 \cos\theta_1 + \mu_2 N_1 \cos\theta_2)(\mu_2 N_1 \cos\theta_1 + \mu_1 N_2 \cos\theta_2)\cos\theta_2} \qquad \text{Equation 2.22}$$

$$r_{ps} = \frac{i\mu_1\mu_2 N_1 N_2 \cos\theta_1 Q(m_y \sin\theta_2 + m_z \cos\theta_2)}{(\mu_1 N_2 \cos\theta_1 + \mu_2 N_1 \cos\theta_2)(\mu_2 N_1 \cos\theta_1 + \mu_1 N_2 \cos\theta_2)\cos\theta_2} \qquad \text{Equation 2.23}$$

$$r_{pp} = \frac{\mu_1 N_2 \cos\theta_1 - \mu_2 N_1 \cos\theta_2}{\mu_1 N_2 \cos\theta_1 + \mu_2 N_1 \cos\theta_2} + \frac{2i\mu_1\mu_2 N_1 N_2 \cos\theta_1 Q m_x \sin\theta_2}{\mu_1 N_2 \cos\theta_1 + \mu_2 N_1 \cos\theta_2} \qquad \text{Equation 2.24}$$

where μ_1, μ_2 are the permeabilities of media 1 and 2; N_1, N_2 are the complex indices of refraction; θ_1 is the incident angle; θ_2 is the refracted angle. The Kerr rotation, θ_k, and

ellipticity, η_k, for individual s- and p-polarised components are defined as per equations 2.21 to 2.24, while the total Kerr rotation and ellipticity are superpositions of the two components [109]:

$$\theta_{ks} = \mathrm{Re}\left(r_{ps}/r_{ss}\right) \quad \text{Equation 2.25}$$

$$\theta_{kp} = \mathrm{Re}\left(r_{sp}/r_{pp}\right) \quad \text{Equation 2.26}$$

$$\eta_{ks} = \mathrm{Im}\left(r_{ps}/r_{ss}\right)\mathrm{Re}\left(r_{ps}/r_{ss}\right) \quad \text{Equation 2.27}$$

$$\eta_{kp} = \mathrm{Im}\left(r_{sp}/r_{pp}\right)\mathrm{Re}\left(r_{sp}/r_{pp}\right) \quad \text{Equation 2.28}$$

Here Re and Im denote the real and imaginary part of the complex number. The Kerr rotation is quite a small angle, for example, and the Kerr rotation is about 0.02 degrees for Co/Pd multilayer in a polar configuration [108].

2.6.3 Magnetic circular dichroism (MCD)

The ultimate switching speed of magnetic direction has been a subject of considerable interest and debate. All-optical control using femtosecond laser pulses is the fastest manipulating method [17]. This phenomenon was first attributed to the inverse Faraday effect [110, 111]. Then the ultrafast heating effect is proved to be a sufficient stimulus for single-shot AOS in GdFeCo [112], as we discussed in the previous section 2.6.1. While MCD combined with ultrafast heating effect was introduced to explain the helicity dependent switching of Stanciu *el at* [17]. But models for multishot HD-AOS in ferrimagnets like TbFeCo [113] or TbCo [114] and ferromagnets [23, 115] are lacking until today. In retrospect, MCD or IFE is the most likely explanation for the HD-AOS [28, 116, 117], and therefore, they will be introduced in this section.

The MCD as a candidate mechanism for HD-AOS in ferromagnets was first demonstrated by J. Bokor in 2016 [28], and the underlying mechanism is shown in Fig 2.5. There is an energy barrier E_{ab} between the magnetic state a (up) and b (down). However, the magnetic direction may flip due to the thermal fluctuation. Assuming the magnetic system at a temperature T, according to the Neel-Brown formula, the characteristic flipping time from the magnetic state a to b can be given by the following equation:

$$\tau_{ab}(T) = \tau_0 \exp\left(\frac{E_{ab}(T)}{k_B T}\right) \qquad \text{Equation 2.29}$$

Here τ_0 is the attempt time with an order of 100 picoseconds [118], k_B is the Boltzmann constant, and the energy barrier is also temperature dependence, which is inversely proportional to the temperature. The laser's heating effect will increase the sample's temperature to $T_0 + \Delta T$ with a duration of t_{hot}, then the probabilities of magnetic state a to b is given by:

$$P_{ab} = \frac{1}{2}\left[1 - \exp\left(-\frac{t_{hot}}{\tau_{ab}(T_0+\Delta T)}\right)\right] \qquad \text{Equation 2.30}$$

$$P_{aa} = 1 - P_{ab} \qquad \text{Equation 2.31}$$

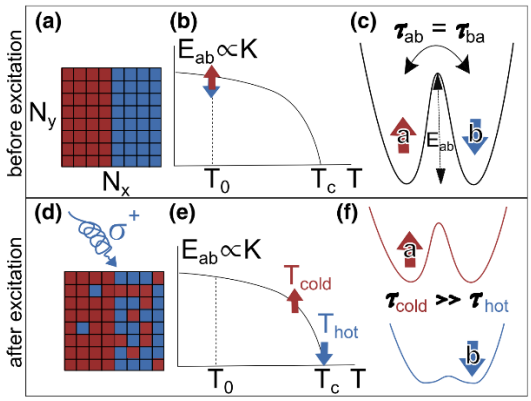

Figure 2.5 (a-f) The HD-AOS model based on the MCD mechanism [28]. A N_x by N_y grid of cells are taken into consideration. (a to c) shows the initial state before exposed to laser pulses. The characterise spin-flip time for the spin-up (a) and (b) is the same. (d to e) After being exposed to a right-handed circularly polarized light due to MCD, the spin-down (b) cell's temperature is higher than the spin up (a) state, which makes the spin flip time $\tau_{ab} \gg \tau_{ba}$.

Due to MCD, the $M^{\uparrow}$ domain absorbs more σ^+ phonons than the $M^{\downarrow}$ domain which makes its temperature closer to the Curie temperature T_c. Also, it makes $M^{\uparrow}$ domain has a higher probability of switching to the $M^{\downarrow}$ domain. Once it switches to the $M^{\downarrow}$ domain, its temperature will decrease as it absorbs less σ^+ phonons. After *N* laser pulses shots, the cumulative probability for the magnetization to end in state *b* are given by:

$$P_B = \left(P_{ib} - \frac{P_{ab}}{P_{ab}+P_{ba}}\right)(1 - P_{ab} - P_{ba})^{N-1} + \frac{P_{ab}}{P_{ab}+P_{ba}} \qquad \text{Equation 2.32}$$

here the subscript *i* refers to the initial state. With laser pulses increasing, the probability is close to 1, and a minimum of 0.5% MCD is needed to achieve multishot HD-AOS. In the cooling process, the existence of a strong dipolar field will decrease the probability of AOS. Hence, magnetic films with a small magnetization volume have a higher switching ratio [23]. MCD effect was observed in ferromagnetic thin films, and the evidence is the helicity-dependent laser-induced domain wall motion in all-optical switchable Co/Pt multilayers, as shown in Fig 2.6 [34]. The linearly polarized laser provides a pure heating effect. When the laser spot is in the centre of the domain wall, there is no temperature gradient, and the domain wall has no motion. While the laser spot is off centre, the temperature gradient drags the domain wall to the hotter side in Fig 2.6 (b). Compared with Fig 2.6 (a) and (b), the domain wall motion was observed even when the circularly polarized laser spot was in the centre of the domain wall. These results prove that the absorption ratio of circularly polarized laser does related to the magnetic direction.

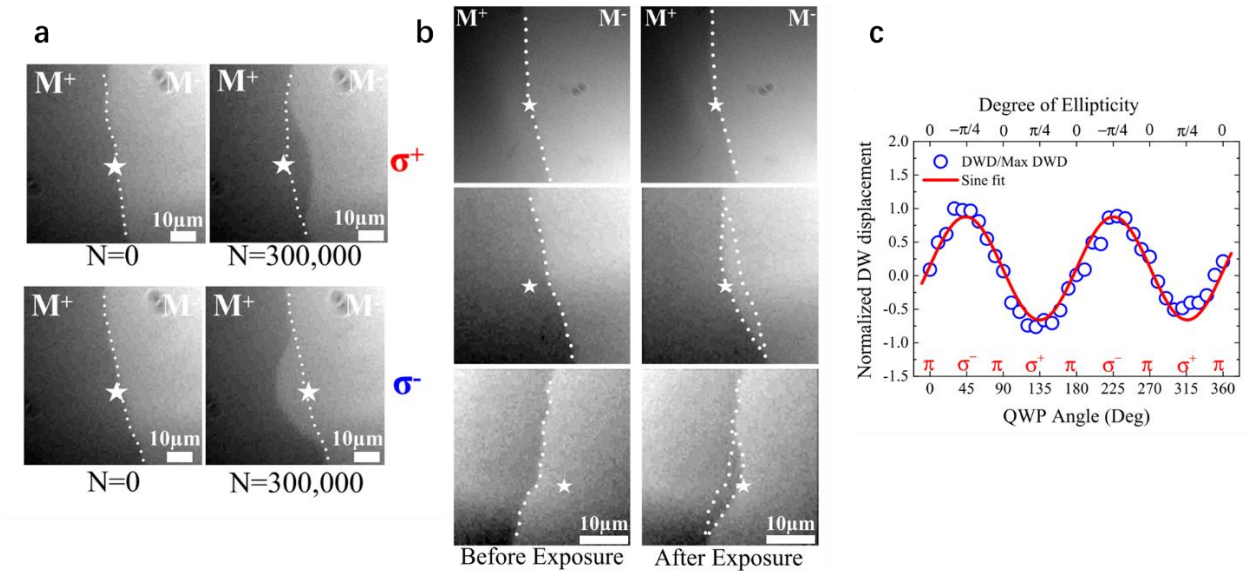

Figure 2.6 Magneto-optical Faraday images of domain wall motion in Co/Pt multilayers induced by (a) circularly polarized (b) linearly polarized 40 femtoseconds laser pulses with fluence per pulse of 12.5 mJ/cm^2. The white star points out the centre of the laser spot, and N is the number of laser pulses. (c) Normalized domain wall motion as a function of the degree of laser's ellipticity [34].

2.6.4 The Inverse Faraday Effect (IFE)

Although IFE was predicted by Pitaevskii in 1961 [111], 44 years later, it was firstly reported by Kimel *et al.* that spins can indeed be manipulated by a circularly polarized laser beam [119]. Then the discovery of HD-AOS has revealed direct optical control of magnetization, and the IFE was considered the mechanism of HD-AOS from the beginning [120].

It was the easiest way to introduce the HD-AOS required magnitude and duration of the IFE magnetic field. IFE hypothesizes circularly polarized light acts as a strong effective magnetic field pulse B_{eff} on the spins of the magnetic medium. The direction of B_{eff} depends on the helicity of the light, and according to the atomistic spin simulations, about ~10 T field is needed to describe some key features of HD-AOS [121]. Koopmans' group extended the M3TM model [104] and described the IFE induced magnetization dynamics in the following equation [30]:

$$\frac{dm}{dt} = \frac{RT_p}{T_C}\left[m + B_{eff}\right]\left[1 - m\coth\left(\frac{T_C}{T_e}\left[m + B_{eff}\right]\right)\right] \qquad \text{Equation 2.33}$$

where m is the magnetization relative to the saturation value, T_C is the Curie temperature, and R is a prefactor in the demagnetization rate. The calculated magnetic dynamics based on this equation are shown in Fig 2.7 (a). Also, crucial parameters in determining whether HD-AOS will occurs are calculated in the phase diagram. The minimal lifetime of the IFE field to achieve HD-AOS is the order of 100 fs with a magnitude of 20 T, as presented in Fig 2.7 (b).

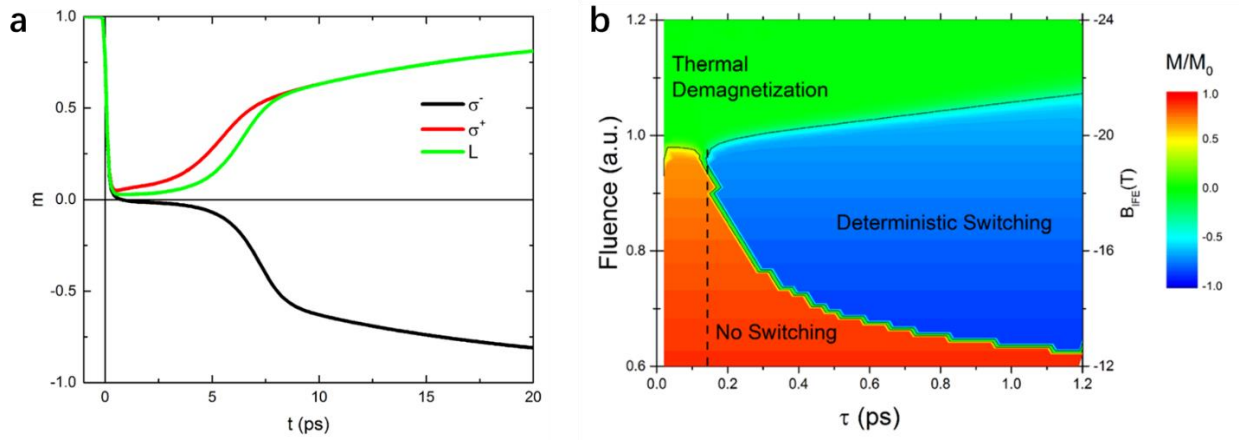

Figure 2.7 (a) The magnetization as a function of time after being exposed to three different polarized laser pulses. The linear polarized pulse is assumed to have no magnetic field, while the circularly polarized pulse has a magnetic field of 10 T and a duration of 0.4 ps. (b) Phase diagram of HD-AOS as a function of IFE field's magnitude and duration [30].

The magnetic field induced by laser pulse's IFE, as discussed in the foregoing, has a strength that is comparable with exchange coupling. The origin of the IFE has not been fully understood, and various treatments have been proposed. A simple derivation of the IFE was proposed by Hertel [122], which involves microscopic currents rather than a purely phenomenological approach. In his derivation, the conducting electrons in metallic materials are treated as plasma, and the light's perturbation is treated as a high-frequency electromagnetic field. Then the magnetization $\boldsymbol{M}$ generated in the plasma by the field can be presented as [122]:

$$\boldsymbol{M} = \frac{i\varepsilon_0 e\omega_p^2}{4m\omega^3}\left[\widehat{\boldsymbol{E}} \times \widehat{\boldsymbol{E}}^*\right] \qquad \text{Equation 2.34}$$

Where m and e are the electron's mass and charge, respectively; ω and $\widehat{\boldsymbol{E}}$ are the light's frequency and electrical component, respectively; $\omega_p = (\langle n \rangle e^2/m\varepsilon_0)^{1/2}$ is the plasma frequency. If the light is propagating in the z-direction, the last term of equation 2.34 can be written as

$$\widehat{\boldsymbol{E}} \times \widehat{\boldsymbol{E}}^* = \pm i|\boldsymbol{E}|^2 \cdot e_z \qquad \text{Equation 2.35}$$

According to this equation, the opto-magneto field's direction is the same as the light's propagating direction. That is why the HD-AOS is only observed in materials with perpendicular magnetic

anisotropy. Also, equation 2.35 equals zero in the case of linear polarization, and its sign depends on the chirality of the light wave.

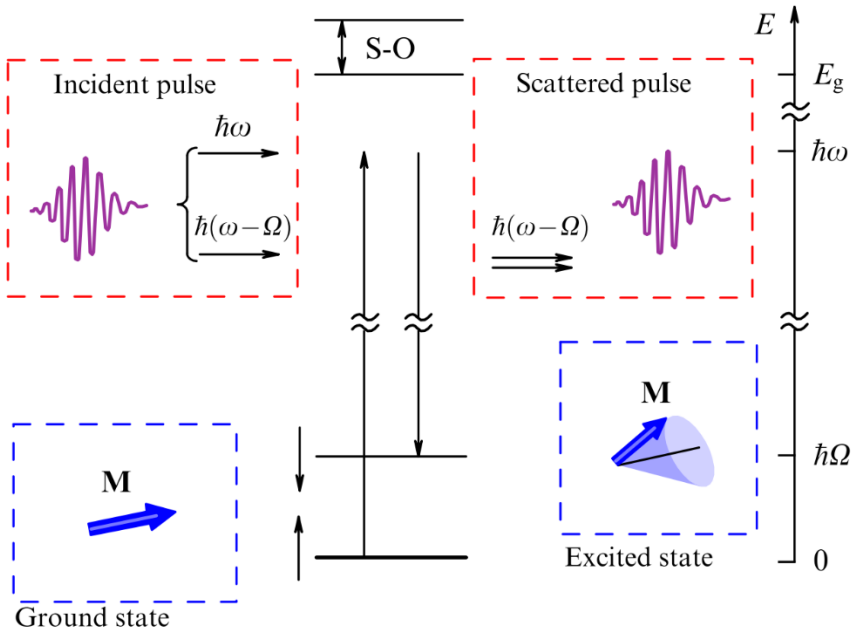

Figure 2.8 Schematic representation of the process of impulsive stimulated Raman scattering on the magnon *[123]*. The right axis shows the corresponding energy, as it indicates the photon energy is lower than the edge of the fundamental absorption $\hbar\omega < E_g$, and the difference equations to Ω. The incident photon pair have the frequency of $\omega - \Omega$ and ω. After they participate in the SRC process, the scattered photon pair's frequency drops to $\omega - \Omega$, and this process generates a magnon with frequency Ω.

Although the above equation $M(t) = \gamma \widehat{\boldsymbol{E}} \times \widehat{\boldsymbol{E}}^*$ described the light-induced magnetic field, it is based on a much longer pulse duration compared with the ultrafast laser pulse used in HD-AOS. There should be different mechanisms that describe the ultrafast IFE. A new assumption was made that the microscopic mechanism of ultrafast IFE is the stimulated Raman scattering (SRC) on magnons [120, 124]. SRC can be regarded as a second-order inelastic scattering of light, which will generate an excited state. As shown in Fig 2.8, they considered two photons with frequencies ω and $\omega - \Omega$. The ultrafast laser used in HD-AOS has a duration that varies from 10 fs to 1 ps, which is about one 2 orders shorter than the coherent spin precession period $2\pi/\Omega$. Therefore, there must be pairs of photons in the laser pulse that satisfy the SRC process leading to coherent

magnons' excitation. The spin-orbit coupling plays an irreplaceable role here since the optical electric dipole matrix elements cannot change the spin magnetic quantum number m_s alone, but invoking the spin-orbit coupling, it makes it possible to reach the excited state with $\Delta m_s = \pm 1$ [125]. Another important feature of IFE is that IFE induced magnetization is strongly materials and frequency-dependent according to the ab initio calculation [32, 126]. As shown in Fig 2.9, spin and orbital parts are calculated separately. For magnetic materials (Fe, Co and Ni), the spin IFE shows negligible dependence on the laser polarization, while the nonmagnetic metals have a small spin IFE component. And the total IFE for all materials is mainly contributed by the orbital component. The photon energy dependence also provides a deep insight into HD-AOS. Compared with other materials, Pt shows a much stronger IFE, which could explain most of the HD-AOS materials have Pt layers. The mostly used laser in HD-AOS has photon energy of about 1.5 eV (800 nm), but according to calculated results, the IFE is much larger when using higher photon energy, and it is valuable to do the HD-AOS with different photon energy.

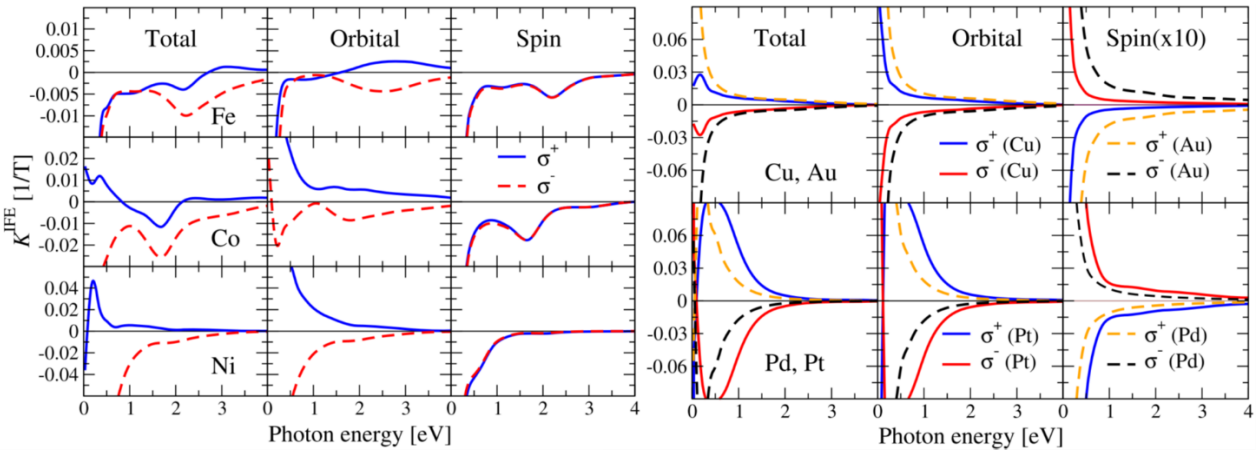

Figure 2.9 Materials specific ab initio theoretical calculated total, orbital, and spin IFE as a function of the photon energy and laser polarizations [32].

2.7 First principal calculation

2.7.1 Introduction to Density functional theory

According to quantum mechanics, once the system's Hamiltonian was obtained, we could get the system's all properties by solving the system's Schrödinger equation. For many simple systems, like a single atom or molecule, this method gives beautiful and accurate results. But for now, there

is no precise computation method for solving a multi-electron system's Schrödinger equation. Solid is a multi-particle system with a 10^{29} orders of magnitude electrons/nuclei per cubic meter. Its Hamiltonian includes all the nuclei and electrons' kinetic energy and their interaction with each other. The Hamiltonian of a solid system can be present by the following equation:

$$H = H_e + H_N + H_{e-N} \qquad \text{Equation 2.36}$$

Since the motions of nuclei are ignorable compared with the outer shell electrons, the Born-Oppenheimer approximation suggests that the system's total Hamiltonian can be separated into the electronic and nuclear parts. The simplified Schrödinger equation is:

$$\left[-\sum_i \frac{\hbar^2}{2m}\nabla_i^2 + \frac{1}{8\pi\varepsilon_0}\sum_{i\neq j}\frac{e^2}{|\boldsymbol{r_i}-\boldsymbol{r_j}|} + \sum_i v(\boldsymbol{r_i})\right]\varphi(\boldsymbol{r}) = E\varphi(\boldsymbol{r}) \qquad \text{Equation 2.37}$$

where the first term in the left side is the electron's kinetic energy, the second term is the electron-electron repulsion interaction and the third term is nuclear potential. As each electron has 3 degrees of freedom (excluding the spin degree of freedom), a system with *N* electrons has 3*N* degrees of freedom. It is still impossible to solve this equation. Density Functional Theory (DFT) provides a new way of researching complex multi-electron systems. DFT is an ab-initio theory based on quantum mechanics, which does not need any experimental parameters, but DFT calculation gives important physical properties of the system. DFT does not consider each electron's position but treats the whole electrons as an electron density $\rho(\boldsymbol{r})$. Also, due to the wave-particle dualism and uncertainty principle, even if we get the electron's wavefunction, we cannot predict the electron's position at any given moment. DFT expresses the system's energy as a function of $\rho(\boldsymbol{r})$ and it is proved by the Hohenberg-Kohn theorem that the total energy of an interacting inhomogeneous electron gas in the presence of an external potential $V_{ext}(r)$ is a function of the density $\rho(\boldsymbol{r})$[127], and the ground state energy of this system is the only function of the particle number density. Then Kohn and Sham proposed to replace the system's interacting functionals with separated, non-interacting functionals and to express all correlations in so-called exchange-correlation functionals. That means the real kinetic energy $T(\rho)$ and the potential energy $U(\rho)$ are replaced by the non-interacting kinetic energy $T_s(\rho)$ and the non-interacting potential energy $U_H(\rho)$, which can be solved by the Hartree-Fock equation. The difference between their approximate value and the real

value is put into the exchange-correlation functional $E_{xc}(\rho)$, and only this term is used to include all the errors and unknown effects.

$$E_{xc}(\rho) = [T(\rho) - T_s(\rho)] + \big(U(\rho) - U_H(\rho)\big) + E_{unknow}(\rho) \qquad \text{Equation 2.38}$$

$$E(\rho) = T_s(\rho) + U_H(\rho) + V(\rho) + E_{xc}(\rho) = T_s(\rho) + \frac{e^2}{8\pi\epsilon_0}\iint \frac{\rho(\boldsymbol{r})\rho(\boldsymbol{r}')}{|\boldsymbol{r}-\boldsymbol{r}'|}d\boldsymbol{r}d\boldsymbol{r}' + E_{xc}(\rho)$$

Equation 2.39

Here the electron density and the real kinetic energy can be presented by:

$$\rho(\boldsymbol{r}) = \sum_{i=1}^{N}|\varphi_i(\boldsymbol{r})|^2 \qquad \text{Equation 2.40}$$

$$T(\rho) = \sum_{i=1}^{N}\int \varphi_i^*(\boldsymbol{r})(-\frac{\hbar^2}{2m}\nabla^2)\varphi_i(\boldsymbol{r})d\boldsymbol{r} \qquad \text{Equation 2.41}$$

Then the variation of these two equations is equal to a single electron's Schrodinger equation:

$$\left[-\frac{\hbar^2}{2m}\nabla^2 + V_{eff}(\boldsymbol{r})\right]\varphi_i(\boldsymbol{r}) = E_i\varphi_i(\boldsymbol{r}) \qquad \text{Equation 2.42}$$

$$V_{eff}(\boldsymbol{r}) = V(\boldsymbol{r}) + \frac{e^2}{4\pi\varepsilon_0}\int \frac{\rho(\boldsymbol{r}\prime)}{|\boldsymbol{r}-\boldsymbol{r}\prime|}d\boldsymbol{r}' + \frac{\delta E_{xc}(\rho)}{\delta\rho(\boldsymbol{r})} \qquad \text{Equation 2.43}$$

These equations are the so-called Kohn-Sham equation which is consistent. As the effective potential V_{eff} is determined by the electron density and the electron density can be calculated from the wavefunction $\varphi_i(\boldsymbol{r})$. About the only unknown term exchange-correlation energy $E_{xc}(\rho)$, there are two most used approximations called Local Density Approximation (LDA) [128, 129] and Generalized Gradient Approximation (GGA) [130]. For LDA approximation derived from the homogeneous electron gas model, the exchange-correlation energy has the following expression:

$$E_{xc}(\rho) = \int n(\boldsymbol{r})\,\epsilon_{xc}(n(\boldsymbol{r}))d\boldsymbol{r} \qquad \text{Equation 2.44}$$

For the system with electron density $\rho(\boldsymbol{r})$ changes slowly with the $\boldsymbol{r}$, the LDA approximation gives accurate calculation results. For the system with electron density $\rho(\boldsymbol{r})$ changes fast with the $\boldsymbol{r}$, LDA should be replaced by GGA:

$$E_{xc}(\rho) = \int n(\boldsymbol{r})\epsilon_{xc}(n(\boldsymbol{r}),\nabla n(\boldsymbol{r}))d\boldsymbol{r} \qquad \text{Equation 2.45}$$

GGA approximation adds the electron density gradient term. This correlation gives better results like lattice constant, molecular bond, cohesive energy, and bandstructure.

2.7.2 Pseudopotential

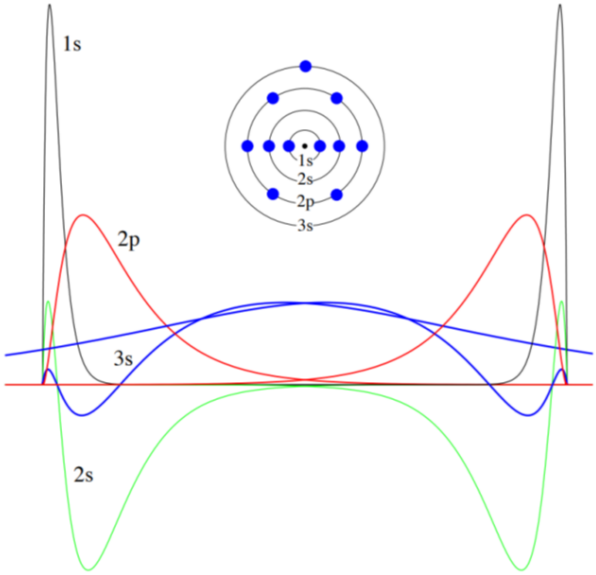

Figure 2.10 The schematic diagram for the overlapping of different electron orbits. When the atoms are composed of molecules, the overlapping of orbits (1s, 2s and 2p) of inner shell electrons is ignorable. Core states are approximately inert and insensitive to the environment. Hence, we could combine inner electrons with the nucleus to make a pseudo-ion.

Now we introduce the last important approximation, pseudopotential. As shown in Fig 2.10, the chemical bonding arises from the overlap of outer electrons. Since the outer shell electrons determine the system's most properties like electrical conductivity, magnetism, optical properties and so on, the change of the inner shell electrons' wavefunction is neglected when isolated atoms are composed into a condensed matter state. Based on this fact, the pseudopotential method is proposed, which treats the inner shell electrons as core electrons and the outer shell electrons as valence electrons. Here we introduce the valence electron's pseudopotential wavefunction (ψ_{ps}) in a single atom. Suppose ψ^v and ψ^c are the valence electron's and core electron's wavefunctions, respectively, and their Schrödinger equations are:

$$\widehat{H}|\psi^v\rangle = \epsilon^v|\psi^v\rangle \qquad \text{Equation 2.46}$$

And

$$\hat{H}|\psi^c\rangle = \epsilon^c|\psi^c\rangle \qquad \text{Equation 2.47}$$

Here ϵ^v and ϵ^c are the eigenvalue of the valence and core electrons, respectively. And

$$\hat{H} = \hat{T} + V \qquad \text{Equation 2.48}$$

is the single electron's Hamiltonian. $\hat{T}$ is the electron's kinetic energy part, and the potential V. We could construct the pseudopotential as follow:

$$|\psi_{ps}\rangle = |\psi^v\rangle + \sum_c \langle \psi^c|\psi_{ps}\rangle |\psi^c\rangle \qquad \text{Equation 2.49}$$

Then the valence electron's wavefunction can be presented by:

$$|\psi^v\rangle = |\psi_{ps}\rangle - \sum_c \langle \psi^c|\psi_{ps}\rangle |\psi^c\rangle \qquad \text{Equation 2.50}$$

Using the Hamiltonian operator in the equation:

$$\hat{H}|\psi^v\rangle = \hat{H}\left[|\psi_{ps}\rangle - \sum_c \langle \psi^c|\psi_{ps}\rangle |\psi^c\rangle\right] \qquad \text{Equation 2.51}$$

And then replace the $|\psi^v\rangle$ and get the eigenvalue of the Hamiltonian operator:

$$\epsilon^v\left[|\psi_{ps}\rangle - \sum_c \langle \psi^c|\psi_{ps}\rangle |\psi^c\rangle\right] = \hat{H}|\psi_{ps}\rangle - \sum_c \epsilon^c|\psi^c\rangle\langle\psi^c|\psi_{ps}\rangle \qquad \text{Equation 2.52}$$

We could extract the $|\psi_{ps}\rangle$ in both side of this equation:

$$\epsilon^v[1 - \sum_c |\psi^c\rangle\langle\psi^c|]|\psi_{ps}\rangle = \left[\hat{H} - \sum_c \epsilon^c|\psi^c\rangle\langle\psi^c|\right]|\psi_{ps}\rangle \qquad \text{Equation 2.53}$$

Rewrite this equation in the form of Schrödinger equation we get:

$$\left[\hat{H} + \sum_c (\epsilon^v - \epsilon^c)|\psi^c\rangle\langle\psi^c|\right]|\psi_{ps}\rangle = \epsilon^v|\psi_{ps}\rangle \qquad \text{Equation 2.54}$$

It is obviously that this equation gives a Schrödinger equation with a new Hamiltonian with the eigenfunction of the pseudopotential wavefunction $|\psi_{ps}\rangle$ and the same eigenvalue ϵ^v of the valence electron:

$$\hat{H}_{ps} = \hat{H} + \sum_c (\epsilon^v - \epsilon^c)|\psi^c\rangle\langle\psi^c|$$

$$= \hat{T} + V + \sum_{c} (\epsilon^{v} - \epsilon^{c}) |\psi^{c}\rangle\langle\psi^{c}|$$

$$= \hat{T} + V_{ps} \qquad \text{Equation 2.55}$$

Compared with the normal potential, this pseudopotential V_{ps} has a new term $\sum_c(\epsilon^v - \epsilon^c)|\psi^c\rangle\langle\psi^c|$. V_{ps} includes two parts, the first part is the Coulomb attraction potential provided by the nuclear which is negative, and the second part is the Coulomb repulsion potential provided by other electrons which is positive. And since the valence electron has a higher eigenenergy, this term is positive ($\sum_c(\epsilon^v - \epsilon^c)|\psi^c\rangle\langle\psi^c| > 0$) as well and hence, the pseudopotential V_{ps} is smoother than the *V*.

Chapter 3 Experiment technology

3.1 Magneto-optical Kerr effect image system

The Magneto-optical Kerr effect (MOKE) image system, as the name implies, is based on the Kerr effect. This system helps us to image the magnetic material's domain structure. The basic experimental setup is shown in FIG 3.1. (a). The Light-emitting diode provides a 450 nm light to the system, which gives a better optical resolution than longer wavelength light. Lens 1 plays the role of light collector while the aperture is on its back-focus plane. The latter not only adjusts the luminous flux but also controls the light's incident direction to the sample. When the light is perpendicular to the sample, then the whole system is sensitive to the out-of-plane materials, which is called polar MOKE mode. If not, it detects the in-plane material called longitudinal MOKE mode. Since Lens 1 and 2 are conjugated, the light becomes parallel light after Lens 2. Lens 3 and the objective lens are also conjugated that ensures the incident light is parallel light.

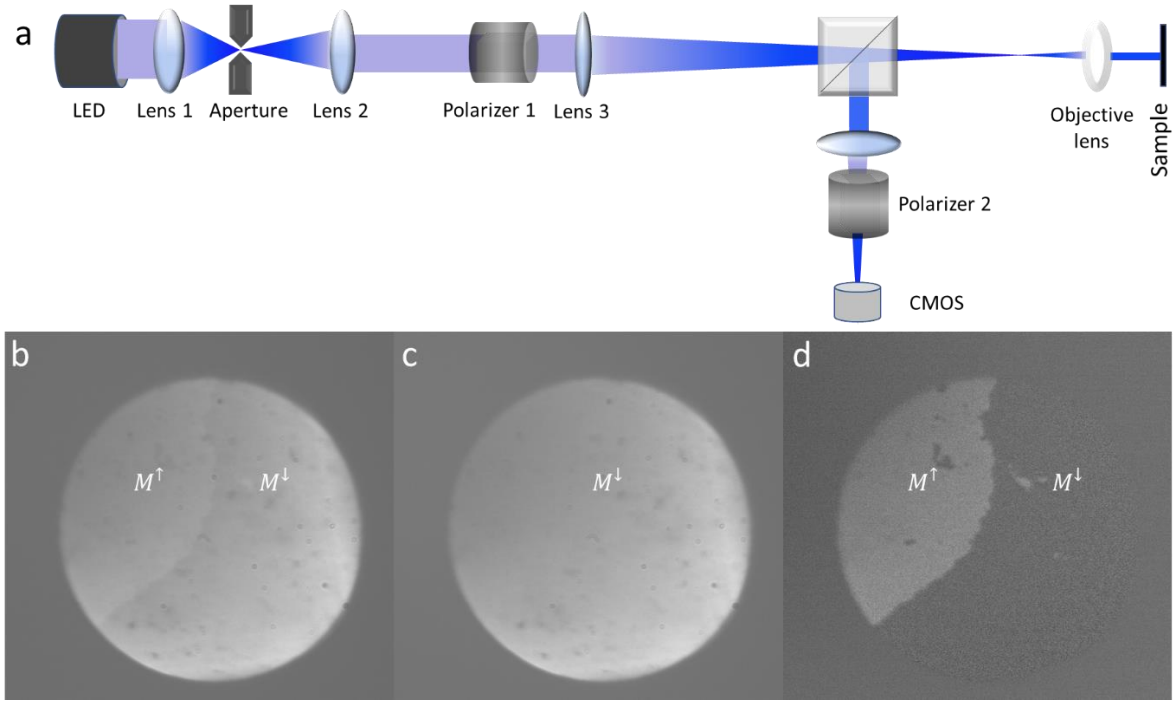

Figure 3.1 (a) Schematic drawing of the experimental setup for magnetic domain imaging using the magneto-optical Kerr effect. (b) The raw magnetic domain image of the Co/Pt out-of-plane

thin film, while the sample is in a multi-domain state. (c) The image of a single domain state. (d) The subtraction image of (b) and (c), which shows a better contrast than (b).

As we mentioned in Chapter 2, the light reflected from a magnetic sample will have a small rotation angle in the polarization plane. Here the polarizer 1 is set to S polarization, while polarization 2's direction is nearly perpendicular to it. Therefore, the magnetic state of the sample could change the luminous flux to the complementary metal-oxide-semiconductor (CMOS) detector. And the intensity obeys:

$$I_{\uparrow} = \frac{1}{2} I_0 cos^2(\varphi + \theta_K), \text{ for the } M^{\uparrow} \text{ domain,}$$

$$I_{\downarrow} = \frac{1}{2} I_0 cos^2(\varphi - \theta_K), \text{ for the } M^{\downarrow} \text{ domain.}$$

where I_0 is the intensity of the incident light, φ is the angle between polarizer 1 and 2, and θ_K is the Kerr angle. FIG 3.1. (b) shows a classical polar MOKE image. The circle shows the boundary of the field of view. There are two different magnetic states in the circle labelled as $M^{\uparrow}$ and $M^{\downarrow}$, which show a different light intensities. It is impossible to ensure I_0 has the same value for each point on the field of view, that decreases the signal-noise contrast. Hence, we take another image in the same place and magnetize it to the same direction as shown in FIG 3.1 (c). Then the subtraction of (b) and (c) only remains the magnetic signal, and its contrast has significant improvement.

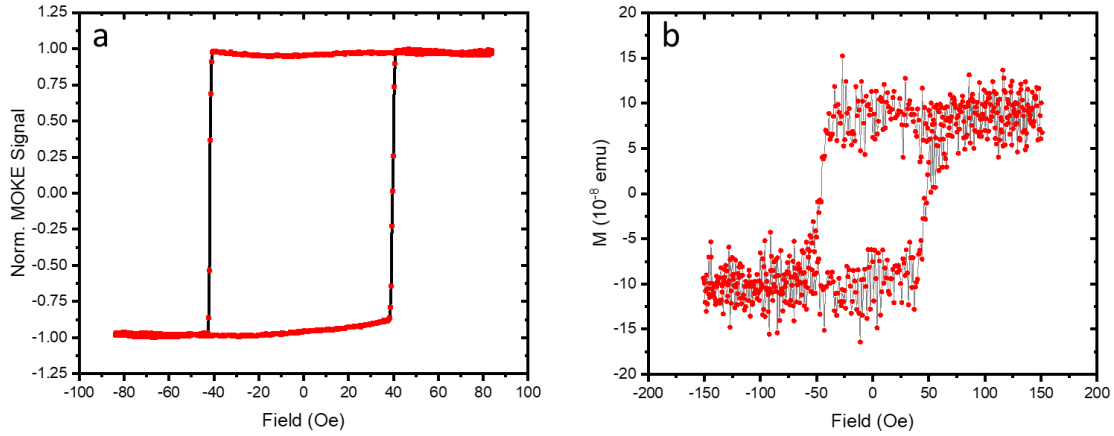

Figure 3.2 The single hysteresis loop of the out-of-plane Co/Pt multilayer sample. (a) was taken from the MOKE image system, and (b) was taken from the VSM.

By changing the electromagnet's field, we could get the whole hysteresis loop images. Therefore, we could get each area's magnetic properties, that helps us compare the sample's domain structures and domain wall. FIG 3.2 (a) shows the hysteresis loop took from our MOKE image system, which has a much better signal-noise ratio than the vibrating-sample magnetometer (VSM) data. However, MOKE image system cannot give the magnetic moment. As the optical signal is related to many non-magnetic effects, one could not calibrate the magnetic moment, while VSM can.

3.2 Time-resolved pump-probe spectroscopy

The femtosecond time-resolved (TR) method was developed in the 1980s [13, 131-133]. As the classical timescale of the electron and spin dynamic is under nanosecond, this methodology has been widely applied to research the physics dynamic process and has led to breakthroughs in our understanding of ultrafast physical properties. There are a variety of interactions between photons and materials, and each of them has the possibility to develop a time-resolved technology based on the ultrafast laser system, like TR-photoluminescence [134], TR-fluorescence [135], TR-x-ray diffraction [136] and etc. MOKE can also yield a great deal of information about magnetization dynamics in magnetic materials. Here we introduce the TR-MOKE technique, which has been used in this thesis.

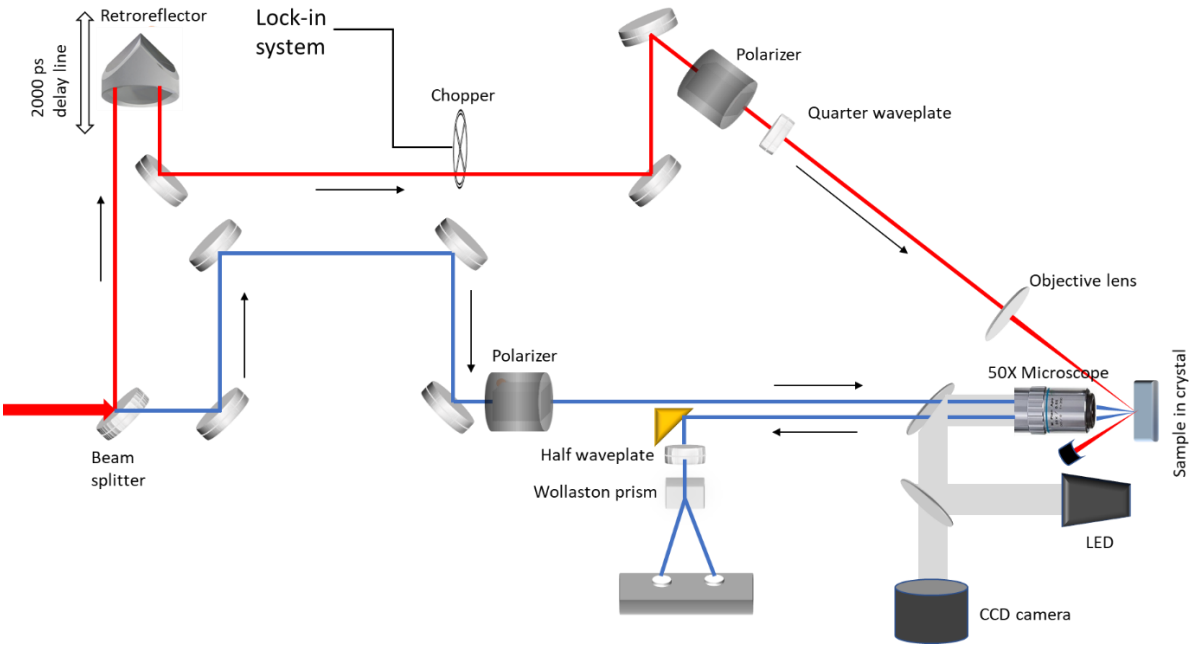

Figure 3.3 Experimental configuration of the time-resolved pump-probe technique. The laser beam is split into a pump (blue line) and a probe (red line). The time delay between pump and probe pulse changes with the movement of the retroreflector. To extract the very weak signal, an optical chopper system and lock-in system are used.

Our laser pulse is generated by the Ti:sapphire laser amplifier system, and it has a Gaussian profile with an approximately 100 fs pulse width at half maximum intensity and 800 nm central wavelength. In terms of the temporary resolution of TR-MOKE, it is determined by the laser's pulse width, here we consider the time resolution is about 100 fs in our measurements. The laser beam is split to two beams, called pump and probe, respectively. As shown in FIG 3.3, the pump beam is presented by the red line, while the probe beam is presented by the blue line. In some measurements, the Beta barium borate (BBO) crystal will be added in the probe line, which changes the probe's wavelength to 400nm. The pump beam goes through a retroreflector, which is mounted at a 300 mm (corresponding to a 2000 ps delay time) linear translation stage. The retroreflector's position determines the delay time between the pump and probe pulses. Then the pump goes through the optical chopper, and some pulses are blocked. FIG 3.4 (a) shows this progress. When the pump pulse is blocked, the detected signal is called I_0. This signal has the same frequency as the probe beam, 1000Hz or 80MHz in our experiments. If not, the pump pulse could induce a small change ΔI. Normally, ΔI would be three to six orders of magnitude smaller

than I_0 [137]. Since the optical chopper gives the pump beam a special frequency f_0, such a small signal can be extracted by the Lock-in amplifier system. Without the Lock-in amplifier system, the noise of I_0 will fully cover the ΔI signal.

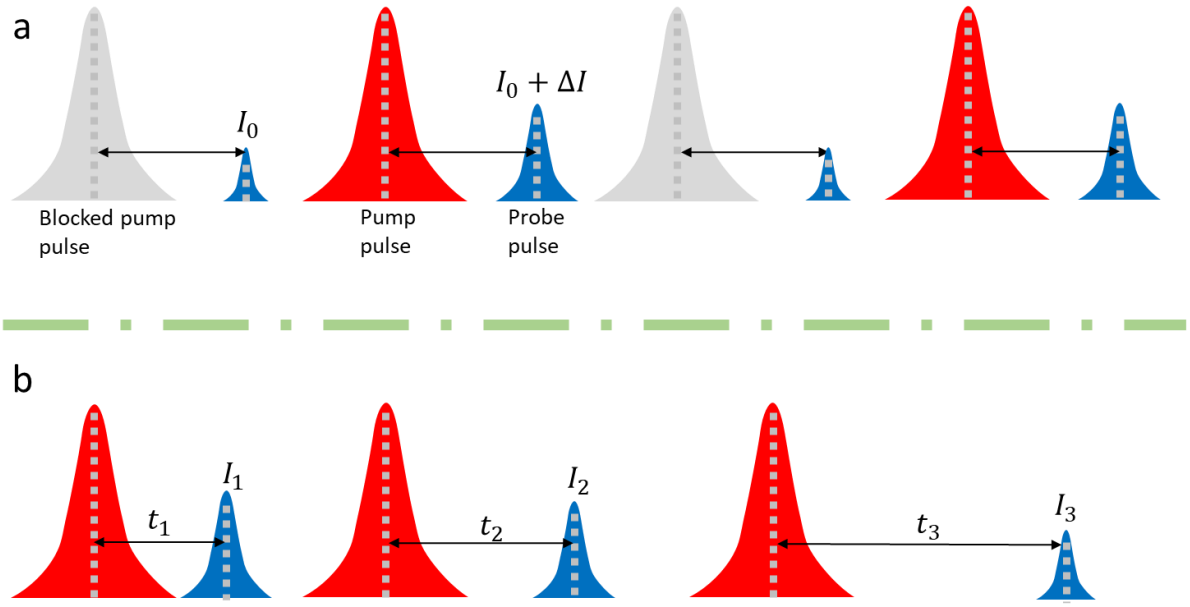

Figure 3.4 Schematic diagram for the detection scheme of TR-MOKE. (a) The pump pulse is blocked by a driving optical chopper with a special frequency of f_0, where I_0 is the origin signal without pump pulse, and ΔI is the pump pulse induced signal change. Here we amplified the proportion of $\Delta I/I_0$ to make it more obvious. (b) The detector's signal $(I_0 + \Delta I)$ is related to the delay time between the pump and probe pulses, as the pump induced signal ΔI changes with the delay time.

The delay time between the pump pulse and probe pulse changes with the position of the retroreflector changing. The conversion relation is simple: $\Delta t = 2x/c$, where *x* is the position of the retroreflector, $x = 0$ is the zero-delay point, and *c* is the light speed. The sample reflected probe beam was collected to the photodetector. The detector we used is a bridge detector, which has two separate Si photodiodes, and we call them A and B here. And there is a half waveplate and a Wollaston crystal in the front of the detector. The Wollaston crystal can separate the light's s and p components into two beams. Before measurements, we will tune the angle of the half waveplate and set the $A - B$ signal of I_0 equal to zero. Fig 3.5 shows the typical time-resolved signal.

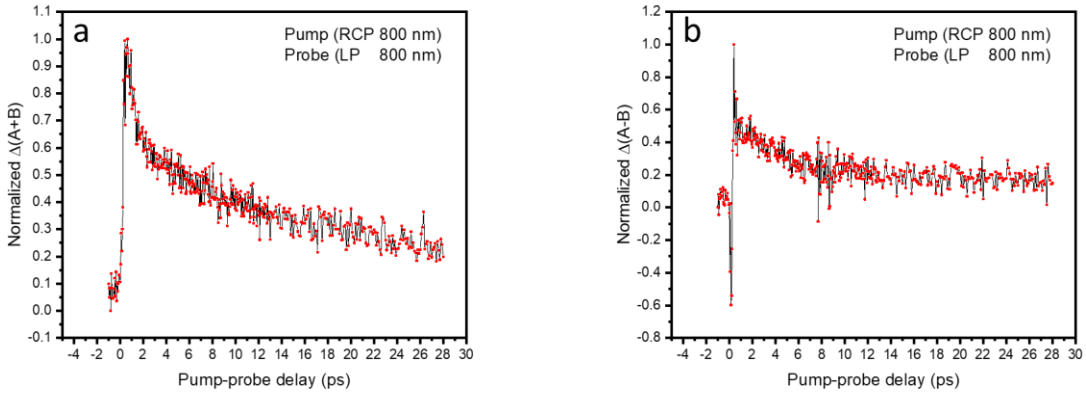

Figure 3.5 Normalized time-resolved signal of the intrinsic GaAs sample. The pump's fluency is 24.4 $\mu J\ cm^{-2}$, and it is right-handed circularly polarized (RCP). While the probe's fluency is 2 $\mu J\ cm^{-2}$, and it is linearly polarized (LP). (a) $\Delta(A+B)$ signal, which is considered as the change of reflection. (b) $\Delta(A-B)$ signal, which is considered as the change of the Kerr signal.

3.3 Magnetron sputtering

Magnetron sputtering is a kind of physical vapour deposition (PVD). The magnetron sputtering method was developed in the 1970s. With the characteristics of simple equipment, large coating area, slow base surface temperature rising and relatively low cost, it has been widely used in the field of scientific research. All the magnetic thin film samples studied in this thesis were grown using the Magnetron sputtering system, as shown in Fig 3.6. A base pressure of 1×10^{-7} mbar will be reached in the growth chamber before growth. This is achieved by the vacuum system, which has a rotary pump and a molecular turbo pump. A rate thickness crystal monitor is used to measure the sputtering rate and hence, the film thickness. This is a key factor to control the properties of the samples. Unlike the normal magnetron sputtering system, the main Ar gas pipe is divided into 5 Ar gas branch pipes. As shown in Fig 3.7 (a), each magnetron sputtering target has its own shutter and argon gas feed. Since the high purity (99.999%) argon gas is directly injected into the sputtering area, the growth pressure is relatively low.

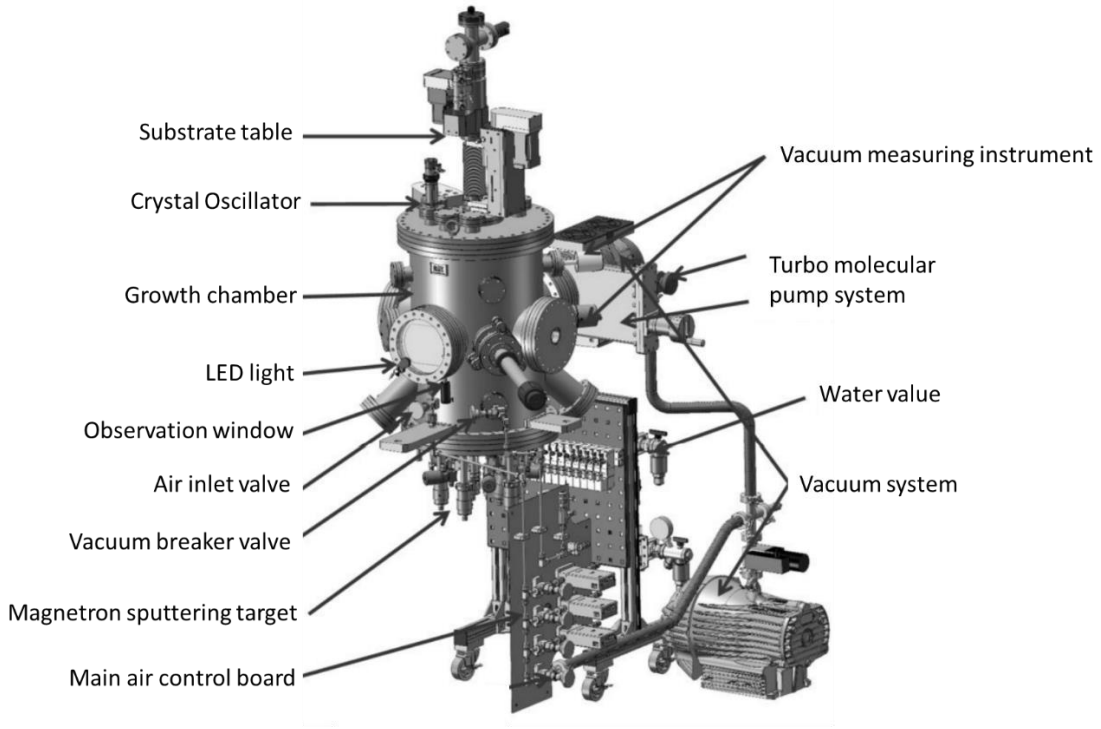

Figure 3.6 Schematic diagram of the magnetron sputtering system we used to grow samples in this thesis.

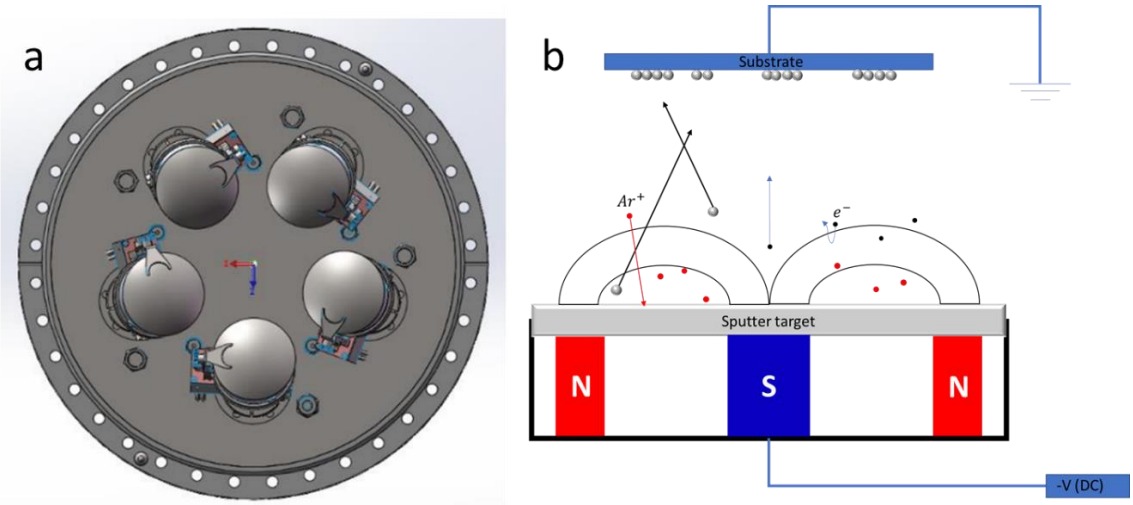

Figure 3.7 (a) Schematic diagram of magnetron sputtering targets and Argon gas feeds. (b) Schematic illustration of the magnetic field and electrical field controlled Ar^+ plasma sputtering process. The sputter target is placed in an electromagnet, and the magnetic field controls the

moving direction of the electrons. A negative voltage up to 900 V is added to the target while the substrate is connected to the ground. The electrical field speeds up electrons and also pushes Ar^+ ions to the target.

Fig 3.7 (b) shows the sputtering process. The magnetron sputtering target is placed in the cathode, and the voltages applied to the target can be increased to -900V. With the electrical field between the target and the substrate increasing, electrons will get enough kinetic energy (>30 eV), then the electron collides with Ar and will produce a new electron and an Ar^+ ion. Although the electrical field will push electrons to the substrate, the Lorentz force provided by the magnetic field makes them travel along that field's lines of force. This magnetic field-controlled process significantly improves the collision probability and highly reduces the number of electrons that arrived in the substrate. Due to that, we get a higher sample purity and a lower substrate temperature. The Ar^+ ion bombards the target due to the electrical field, and its kinetic energy transfers to the target atoms. When the atom's energy exceeds the binding energy, the atom will overflow from the surface, resulting in the sputtering phenomenon. The intensity of plasma up to $10^{12}\sim10^{13}$ ions/cm^{-3} can be generated with an Ar pressure of 3×10^{-3} mbar. To improve the growth samples' purity, the target and the substrate will be cleaned by the Ar^+ plasma sputtering before deposition starts. Firstly, we close the substrate's shutter, and the target shutter is open and, a maximum voltage is added for 60 seconds. This process will remove the top oxidised layer and any other contaminants. Then the target shutter will be closed, and the substrate will be cleaned by the plasma for 60 seconds. The target's shutter opens for another 10 seconds pre-sputtering to get a stable deposition rate. Then the substrate shutter opens, and the growth begins.

3.4 Vibrating Sample Magnetometer

The vibrating sample magnetometer (VSM) is usually used to measure the magnetic properties of magnetic materials. The sample is placed in a uniform magnetic field $\boldsymbol{H}$, causing the sample to be magnetized with a magnetization intensity $\boldsymbol{m}$. In the vibration sample magnetometer measuring system, the sample is placed between the sensing coils, and fixed at an adjustable angle. And the vibration device can vibrate the sample in a fixed up and down at the sine wave mode. According to the Faraday's law of induction, it will generate an electric induction current in the coil near the magnetic sample.

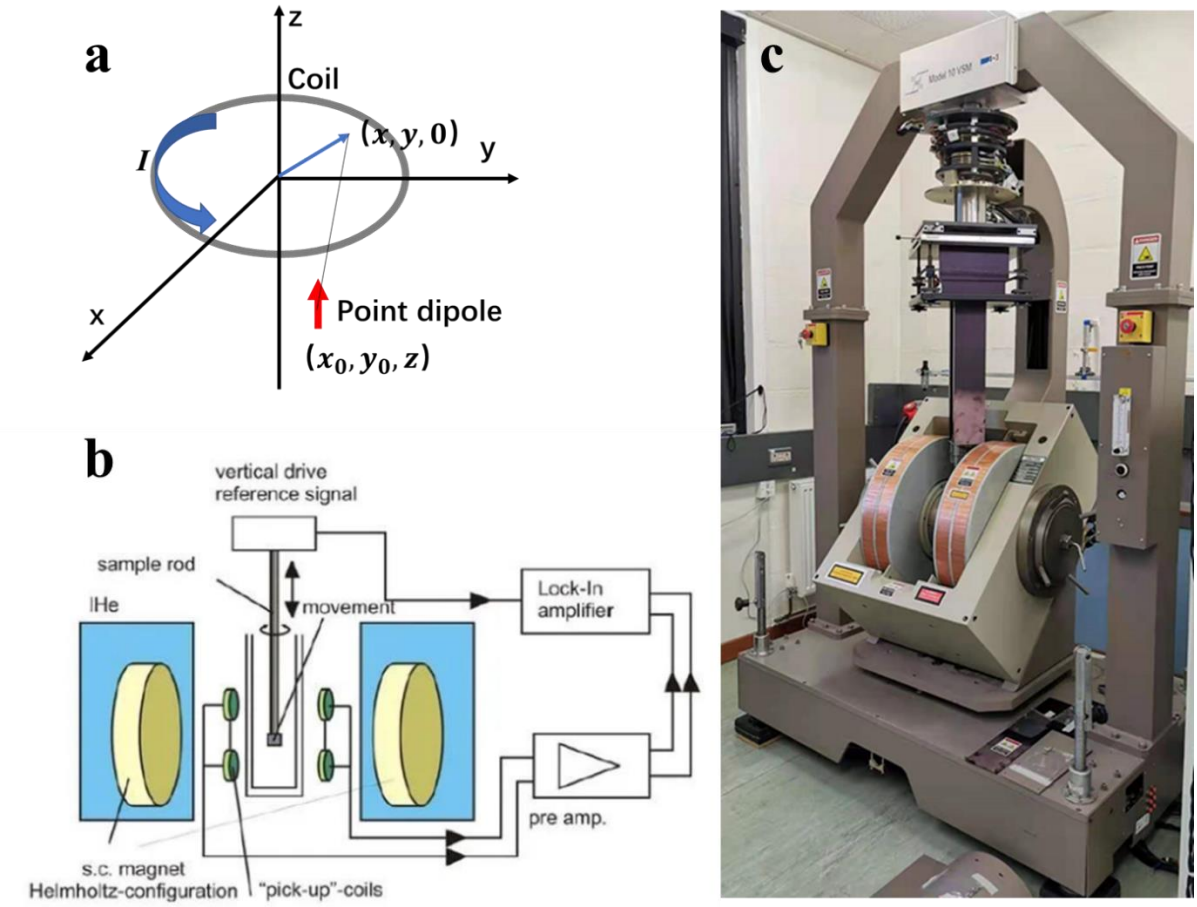

Figure 3.8 (a) A point dipole induces an electrical current in the detecting coil. (b) Schematic diagram of a VSM system. (c) The VSM model used in the York spintronics lab. ADE model 10 VSM has high sensitivity ($< 0.1\ \mu emu$) and a high maximum magnetic field up to 2.2 T.

We shall consider the easiest model, as shown in Fig 3.8 (a). We set the coordinate origin at the coil centre. When the sample is very small, it can be regarded as a point dipole. The magnetic field intensity $\boldsymbol{B}$ at the point (x, y, 0) induced by the point dipole is:

$$\boldsymbol{B}(\boldsymbol{m}, \boldsymbol{r}, t) = \frac{\mu_0}{4\pi}\left[\frac{3(\boldsymbol{m}\cdot\boldsymbol{r})\boldsymbol{r}}{r^5} - \frac{\boldsymbol{m}}{r^3}\right] \qquad \text{Equation 3.1}$$

and the magnetic flux in through the coil is:

$$\phi(\boldsymbol{m}, \boldsymbol{z}, t) = \oint \boldsymbol{B}(\boldsymbol{m}, \boldsymbol{r}, t) \cdot d\boldsymbol{S} = \frac{\mu_0 m_z}{2} \frac{r_c^2}{\sqrt{\left[r_c^2 + z^2(t)\right]^3}} \qquad \text{Equation 3.2}$$

Here $\boldsymbol{r}(t) = (x - x_0)\boldsymbol{i} + (y - y_0)\boldsymbol{j} + z(t)\boldsymbol{k}$. And when the point dipole moves in the z direction, the induction electric potential in the single coil is:

$$\varepsilon_0(m, z, t) = \frac{\partial\phi(\boldsymbol{m},\boldsymbol{z},t)}{\partial t} = -\frac{3\mu_0 m_z}{2}\frac{z(t)r_c^2}{\sqrt{[r_c^2+z^2(t)]^5}} \cdot \frac{\partial z(t)}{\partial t} \qquad \text{Equation 3.3}$$

Now, according to the principle of reciprocity and the Biot-Savart law, the magnetic flux induced by the sample is equivalent to the magnetic flux induced by the current $\boldsymbol{I}$ in the coil:

$$\varepsilon(t) = \frac{d\phi(t)}{dt} = \nabla\left[\frac{\boldsymbol{B}(r)}{I} \cdot \boldsymbol{m}(r,t)\right] \cdot \frac{dr(t)}{dt} = \boldsymbol{m} \cdot \boldsymbol{g}_{coil}(r) \cdot \frac{dr(t)}{dt} \qquad \text{Equation 3.4}$$

Here $\boldsymbol{g}_{coil}$ is called the geometric sensitivity factor. Since the vibration device can vibrate the sample at the cos mode with an amplitude *a* and a frequency ω_0,

$$\varepsilon(t) = \frac{d\phi(t)}{dt} = [\boldsymbol{m} \cdot \omega_0 \cdot a \cdot \boldsymbol{g}_{coil}(r)] \cdot \sin(\omega_0 t + \varphi_0) \qquad \text{Equation 3.5}$$

and this frequency is imported to the lock-in amplifier, the output signal can be presented as:

$$V_{out} = \int [\boldsymbol{m} \cdot \omega \cdot a \cdot \boldsymbol{g}_{coil}(r)] \cdot \sin(\omega_0 t + \varphi_0) \cdot \cos(\omega_1 t + \varphi_1)\, dt$$

$$= \frac{1}{2}\boldsymbol{m} \cdot \omega \cdot a \cdot \boldsymbol{g}_{coil}(r) \int \{sin[(\omega_0 + \omega_1)t + (\varphi_0 + \varphi_1)] + sin[(\omega_0 - \omega_1)t + (\varphi_0 - \varphi_1)]\}\, dt$$

Equation 3.6

As we know the integration $\int \sin(\omega t + \varphi) = 0$ in a 2π cycle. Therefore, the output signal is not zero only if $\omega_0 = \omega_1$.

The VSM model we used in the York spintronics lab is the ADE model 10 VSM. An electromagnet cooled by the water cycle applies a magnetic field provides a maximum magnetic field up to 2.2 T, which magnetized the sample homogenously. This big heavy electromagnet can be rotate in the horizontal plane, and the sample rod also can rotate in the horizontal or vertical plane. Therefore, we could measure the hysteresis loop along any direction. A liquid nitrogen refrigeration and a resistance wire heating system are also added in the sample rod which provide a temperature dependent hysteresis loop measuring from 78 to 773 K. Analysing the data by computer software, the magnetization vs. the applied magnetic field can be plotted, known as the hysteresis loop.

Chapter 4 Heating and helicity effect in helicity-dependent all-optical switching

4.1 Introduction

All-optical magnetization switching (AOS) was first observed in a landmark experiment [17] demonstrating that magnetization can be reversed by laser pulses without any applied magnetic field in GdFeCo. The microscopic mechanism for the AOS process in GdFeCo has been considered to be a helicity-independent heating effect, which is due to the fact that the Fe and Gd sublattices demagnetize on very different timescales [112]. This leads to a transient ferromagnetic-like state discovered in GdFeCo, which mediates the helicity-independent all-optical switching (HID-AOS) [20]. HID-AOS is a single-pulse thermal switching [18, 138] that is not limited to Gd-based ferrimagnetic alloys but has also been observed in Gd-based ferrimagnetic multilayers [22, 139] and the ferrimagnetic Heusler alloy, Mn_2Ru_xGa [140]. However, AOS is also found to be helicity-dependent in some materials such as ferrimagnetic Tb-transition metal (TM) alloys [141], synthetic ferrimagnets [19], and ferromagnetic Co/Pt multilayers [23]. It was initially thought that the circularly polarized light acts as an effective magnetic field, due to the inverse Faraday effect (IFE), in the spin system during helicity-dependent AOS (HD-AOS) [30, 32, 124]. The strength and lifetime of the induced field pulses is still a matter of debate. When HD-AOS is studied in the ultrafast time domain [34, 141], the effective magnetic field strength due to the IFE has to be as large as 10 Tesla to achieve such a short switching time according to the theoretical simulations. A minimal IFE lifetime of 0.15 ps was estimated for Co/Pt [30] while longer durations of several picoseconds after the laser pulse excitation have also been reported [119, 142-144]. Furthermore, the IFE response has been found to be strongly material dependent, and the interlayer exchange interactions and spin-orbit coupling are considered to play an important role in HD-AOS of magnetic multilayers [24]. An optical spin-transfer torque was also suggested to play a role in HD-AOS of ferromagnetic thin films with a Pt capping layer [25]. Other mechanisms put forward to account for HD-AOS include the laser-induced heating [26, 27], magnetic circular dichroism (MCD) [28, 29], and optical selection rule [33].

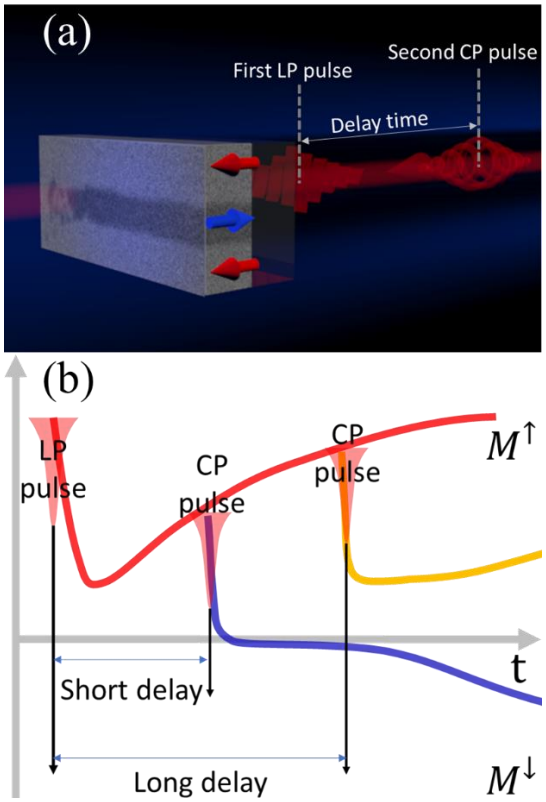

Figure 4.1 Double-pump scheme and its implementation. (a) A magnetic domain image of the Pt/Co/Pt triple-layer sample under laser illumination from the substrate side. The magnetization is initially saturated along the perpendicular direction of the sample plane labeled as $M^{\uparrow}$ state (red arrows). The area exposed under the laser is switched to the opposite direction labelled as $M^{\downarrow}$ state (blue arrow). (b) The magnetization of the exposed area as a function of time with dual-pulse excitation. The first linearly polarized (LP) pulse heats the sample to a demagnetized state (red curve). The second circularly polarized (CP) pulse arrives after a certain delay. For a short delay, the domain switching is expected (blue curve), but for a long delay, the switching may not occur (yellow curve).

Heating and helicity effects are entangled in HD-AOS using circularly polarized laser pulses, and the individual contribution cannot be distinguished by using just one circularly polarized pump beam. Furthermore, as the HD-AOS has been reported as a multi-pulse effect [35], the important information, such as the onset and duration of helicity effects, and interplay between the heating and helicity effects in the first few picoseconds of HD-AOS switching processes cannot be obtained from a conventional time-resolved measurement with a single pump beam [23, 28, 34,

144]. In this work, we have developed a dual-pumping scheme combined with a magneto-optical microscopic detection to investigate HD-AOS in a Pt/Co/Pt triple-layer sample, as shown schematically in Fig. 4.1(a), to identify individual contributions from heating and helicity effects, and distinguish the time dependence between them.

This novel dual-pumping scheme allows us to choose the helicity of each pump pulse independently and vary both the power combination and time delay between the two pump pulses. The pulse width of two pump pulses is the same as 150 fs. The transient pre-heated state of the electron-spin system, on which the second CP pump pulse is to impinge, can be tuned by controlling the power of the first LP pump pulse as well as the precise time delay between the two pulses, as indicated in Fig. 4.1(b). We have found that HD-AOS can be achieved with circularly polarized laser pulses with very low fluencies, if a LP pulse is used to preheat the system into a reduced magnetization state. The strong correlation between HD-AOS and the time interval between the LP and CP pulses signposts an instant onset of helicity effect, but only lasting for a period of the order of the laser pulse duration. The pre-heated transient demagnetized state is found to be a key factor for realizing HD-AOS.

4.2 Experimental Technique

4.2.1 Sample fabrication

The sample used in this study was a Pt (2 nm)/Co (0.6 nm)/Pt (2 nm) triple layer grown on a 5 nm Ta buffer layer. The film was deposited on a Corning glass substrate with thickness of 0.13 mm at room temperature by direct current (DC) magnetron sputtering. The base pressure of the sputtering system was better than 4×10^{-5} Pa. The Ar pressure during growth was 0.5 Pa. The sputtering rate with a DC current of 40 mA was 0.041, 0.084 and 0.048 nm/s for Ta, Pt, and Co, respectively. The Ta buffer layer was employed to improve the Pt/Co interface smoothness and the (111) orientation, and hence enhance the perpendicular magnetic anisotropy of the Co layer. This is confirmed in the MOKE hysteresis loop shown in Fig. 4.2. Here Fig. 4.2(a) is measured by the MOKE image system used in the AOS experiments and Fig. 4.2(b) is measured by the vibrating-sample magnetometer (VSM). Both loops prove that the sample has a well-defined perpendicular magnetic anisotropy.

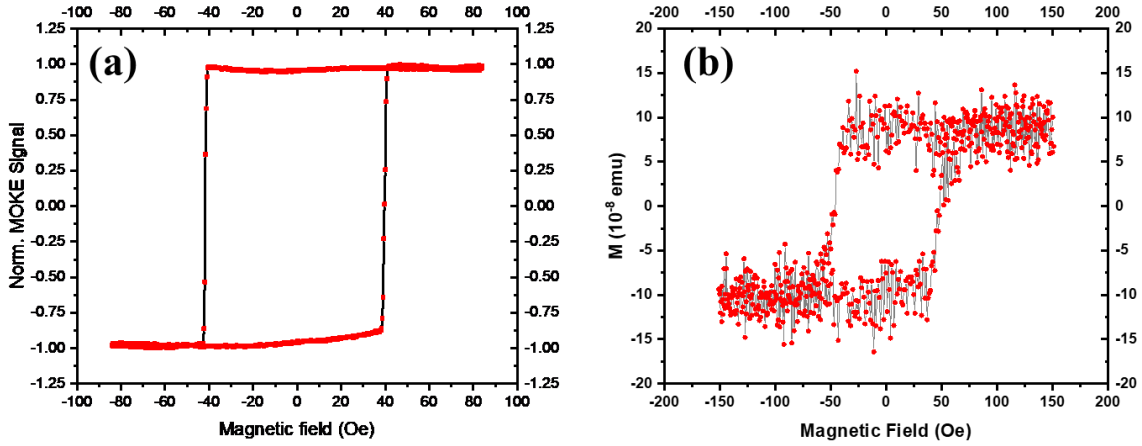

Figure 4.2 Magnetic hysteresis loops of the Glass/Ta (5 nm)/Pt (2 nm)/Co (0.6 nm)/Pt (2 nm) sample at room temperature. Here (a) is measured by MOKE image system and (b) is measured by VSM.

4.2.2 Experimental Method

Fig. 4.3 is a schematic diagram of the double pump experimental setup, which is a combination of TR-MOKE and MOKE image systems. For the image part, the Light-emitting diode provides a 465 nm light to the system. Lens 1 plays the role of light collector, while the aperture is on its back-focus plane. The latter not only adjusts the luminous flux, but also control the light's incident direction to the sample. Since lenses 1 and 2 are conjugated, the light becomes parallel light after lens 2. Lens 3 and the objective lens are also conjugated to ensure that the incident light is parallel. A Ti:sapphire laser amplifier system with 150 fs pulse duration, 800 nm central wavelength, and a 1000 Hz repetition rate was used. For the dual-pumping measurements, the pulse was split into two pulses. The first pump pulse was linearly polarized (LP) and used to heat up the sample's electron/spin systems. The second pump pulse was circularly polarized (CP), delayed with respect to the first LP pulse, and used to switch the sample's magnetic state, as illustrated in Fig. 4.1(a). The power of each pump beam was individually adjusted for a desired power combination. The two pump beams were combined at a beam splitter before being focused onto the Pt/Co/Pt triple layer from the substrate side. The spot size was measured as 38 μm in diameter using a CCD beam profiler, which gives a laser fluence of $8.83 \times 10^{-2} \mathrm{mJ/cm^2}$ at average laser power of 1 μW. The sample was mounted on a motorized 3-axis nanomax flexure stage. The magnetization of

the sample was initially saturated along the perpendicular direction of the sample plane defined as $M^{\uparrow}$ state. When the sample was exposed to the dual-pump beams, the stage was scanned over a 300 μm distance at a velocity of 10 μm/s, equivalent to 100 pulses per every 1 μm illuminated path on the sample from each pump beam. After laser excitation, the magnetic domain state was recorded as a MOKE image via a wide-field Magneto-Optical Kerr (MOKE) microscope. The sample was then re-magnetized to the $M^{\uparrow}$ state and a reference MOKE image was taken. The MOKE images presented are the subtractions of each pair of these images, where any effects from the surface morphology are eliminated.

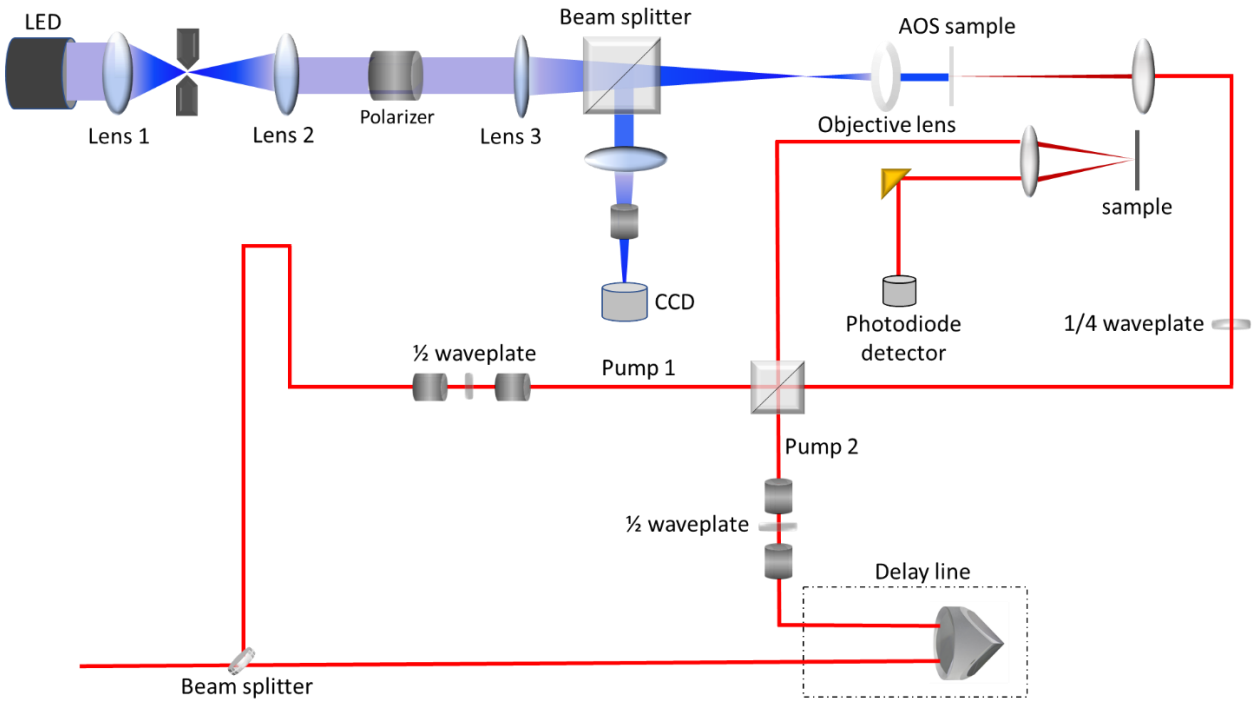

Figure 4.3 A magneto-optical Kerr microscope was coupled to the TR-MOKE laser system. The 450 nm light-emitting diode (LED) served as a light source for the Kerr microscope. The reflected imaging beam was directed towards the charge-coupled-device (CCD) camera by a polarizing beam splitter. As the sample's substrate is glass, the laser beam was focused by another objective lens and pass through the sample from the glass substrate side.

4.2.3 Double pump overlapping

The laser pulse with 150 fs duration and 800 nm central wavelength was split into two pulses by the beam splitter. The delay time between these two pulses is adjusted by the delay time. And the power of each pump beam is adjusted by two polarizers and one half-wave plate, which ensures the power homogeneous of the laser spot. Then the two pump beams were made co-linear by a non-polarizing beamsplitter cube before being focused onto the Pt/Co/Pt triple layer from the substrate side. The quarter-wave plate was set just before the focus lens, as we found the laser's circularly polarization cannot be perfectly maintained after going through the beamsplitter cube and several mirrors. These two beams were linearly polarized, and their polarized directions have a 45° angle. Therefore, after they went through the quarter-wave plate's fast axis, one became circularly polarized and the other was kept linearly polarized. The temporal overlapping of two pump pulses was determined by monitoring interference between them in a time-resolved reflectivity measurement using a GaAs sample. Here, the fringes in the reflectivity signal, as shown in Fig. 4.4 (a), are the cross-correlation of two pulses occurring when they are overlapping in time domain. The duration of the fringes is approximately 300 femtoseconds, which indicates a 150 femtoseconds FWHM pulse duration. These fringes have a period of about 1 femtosecond, which is the same as the step size set for the delay line. Observation of interference fringes allows an easy determination of zero-delay position. The power fluctuation induced by the interference can be measured using a power meter placed in the beam path after the beamsplitter cube. The interference between two beams redistributes the laser fluence and causes a randomly distributed multidomain state at zero-delay point as shown in Fig. 4.4(b). As the interference induces a space power rearrangement, the width of the laser scanned area is bigger than the normal double pump one.

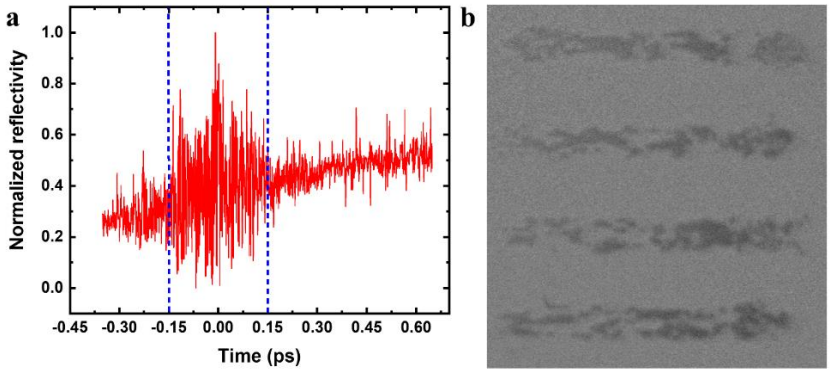

Figure 4.4 (a) Time-domain scan data of the interference at zero delay point on an intrinsic GaAs sample. (b) The interference of two pumps induced multidomain state at the AOS sample.

4.3 Experimental Results

4.3.1 Energy combination and delay time dependence

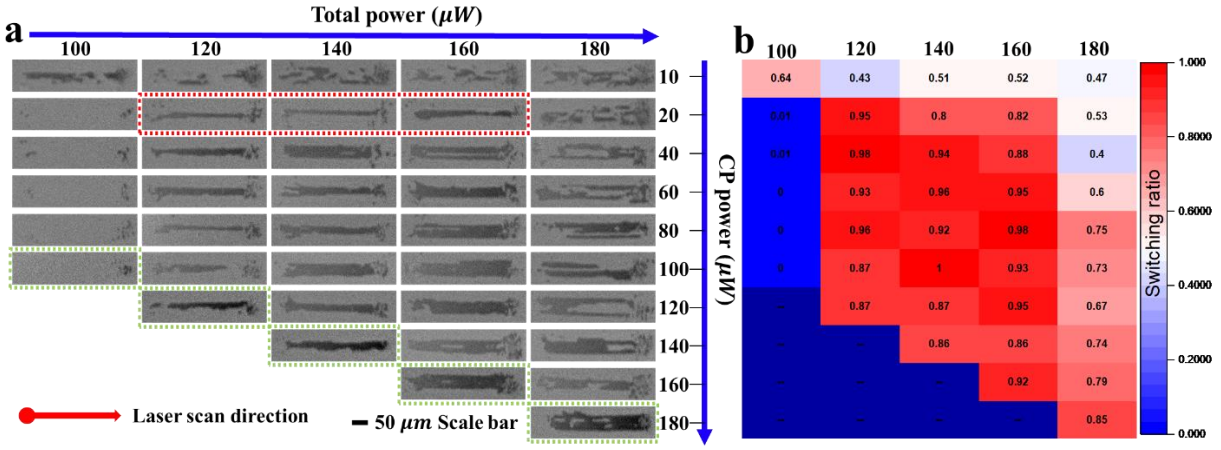

Figure 4.5 HD-AOS induced by dual-pump with different power combinations at a fixed time interval. (a) MOKE images of magnetic domains induced by a sequence of LP and CP pulse pairs with different power combinations and a fixed delay time, 1.6 ps, in a Pt/Co/Pt triple layer. The horizontal axis shows the total power of the LP and CP pulse pairs, increasing from 100 μW to 180 μW, while the vertical axis gives the power of the CP pulse increasing from 10 μW to the the total power of each column. The green frame highlights the images with CP pulses alone

showing a threshold CP power of 120 μW needed for the HD-AOS effect, while the red frame highlights the images showing a clear HD-AOS effect with the CP power as low as 20 μW after preheating with LP light. (b) Extracted switching ratio for each image frame.

HD-AOS induced by a sequence of 100 LP and CP pulse pairs with different power combinations and a fixed delay time, 1.6 picoseconds, between them was investigated first. The energy transfer for the electron-spin system to the lattice system is mediated by the phonons, which takes about 1.6 ps to reach the spin-electron-lattice thermal equilibrium state [104, 145, 146] with the system in a largely demagnetized state when the second CP pulse arrives. Fig. 4.5(a) shows each subtracted MOKE image centered along the scanning path of the dual-pump beam with a field of view of 60 μm × 380 μm. The horizontal axis shows the total power of the LP and CP pulse pairs increasing from 100 μW to 180 μW, while the vertical axis gives the power of the CP pulse increasing from 10 μW to the the total power of each column. The power of the LP pulse used for each image is the difference between the total power and the CP pulse power. Therefore, the power of the LP pump pulse is zero at the bottom of each column and the corresponding magnetic domain images, framed in green dashed line, are induced by the CP pulses only. The switching ratio, which is defined as the ratio between the total number of switched pixels and the total number of pixels within a 20μm×200μm window in each image of Fig. 4.5(a), has been extracted and presented in Fig. 4.5(b). As shown in Fig. 4.5(a), the images of the first-row show that a random domain state is induced when the CP beam power is only 10 μW. The switching ratio of each image on the first-row is between 43% to 64%, again indicating a multi-domain state as shown in Fig. 4.5(b). Once the CP beam power is increased to 20 μW and beyond, HD-AOS was observed with a total power window of 120 μW($10.6\ \mathrm{mJ/cm^2}$) to 160 μW ($14.1\ \mathrm{mJ/cm^2}$). The switch ratio is above 80% across this whole power window. It indicates that the power window for pairs of LP and CP pulses is the same as that for a single CP pulse when the second CP arrives at a 1.6 ps time delay. In the column of the 160 μW total power, multidomain patterns can be seen to emerge in the center of the laser beam path. When the total power was increased to 180 μW, multidomain patterns were induced regardless of power combination. Even though the extracted switching ratio is over 60% in the lower half of the column of the 180 μW total power, the laser caused irreversible changes in the sample's magnetic properties and the coercivity of the exposed

area increases. Therefore 180 μW is excluded from the quoted power window of HD-AOS. The occurrence of the multidomain states under high power laser pumping is due to the laser heating the sample to sufficiently high levels to demagnetize the sample again after HD-AOS. As shown in the images framed in dashed red lines in Fig. 4.5(a), the laser-swept area remains a uniformly switched magnetic domain even when the power of the CP beam is reduced to 20 μW with the samples preheated with the LP pulse. The corresponding switching ratios are all above 80% as shown in Fig. 4.5(b). When the CP beam power is less than 20 μW, no HD-AOS was observed. Therefore, the minimum power of the CP pulse required to achieve HD-AOS is 20 μW when the sample is preheated. It gives a threshold laser fluence for helicity effect as low as 1.77 mJ/cm^2, only 20% of the total laser fluence $10.6\ mJ/cm^2$ (120 μW), which would be the apparent threshold value obtained in measurements with CP pulses only as shown by the images framed with green dashed lines. This proves that the laser heating plays an essential role in HD-AOS of the Pt/Co/Pt triple layer, where only a single magnetic lattice exists, in comparison with HID-AOS in RE-FM alloy/multilayers [5,6]. When the sample is sufficiently demagnetized, circularly polarized illumination with a power threshold as low as 1.77 mJ/cm^2 is sufficient to achieve HD-AOS as demonstrated by the images framed in red dashed lines in Fig. 4.5(a). Without pre-heating by a LP pulse, the CP illumination has to be about five times as intense in order to trigger HD-AOS. This discovery reveals that in a single-pump-induced HD-AOS event in the Pt/Co/Pt structure [20], most of the required pulse energy is used to heat spin system. The helicity effect requires only a small portion of the power threshold.

As indicated in Fig. 4.1(b), the delay time between the LP and CP on HD-AOS is a critical factor. To study this effect in detail, the delay time was set from 0 to 10 ps, with a step size of 0.2 ps for the first 2 ps, and then 0.5 ps afterwards. The CP beam power was increased from 20 to 100 μW with a step size of 10 μW, while the LP was decreased from 100 to 20 μW, so that the total power was fixed at 120 μW, which is the minimum total laser power needed for HD-AOS. The switching ratio of HD-AOS was extracted for each MOKE image captured at every delay time, quantified via image processing using ImageJ [147], and plotted as a function of time delay in Fig 4.6. The calculation details will be discussed in the chapter 4.3.2. Fig 4.6 shows the effect of the delay time between the LP and CP on AOS for 9 different power combinations. It is clear that the switching ratio drops to 0 within 10 ps after the LCP power increases over 60 μW, and this tendency is the

same as the simulation results. This phenomenon furthermore demonstrates that the switching ratio is only related to the on-site magnetic state.

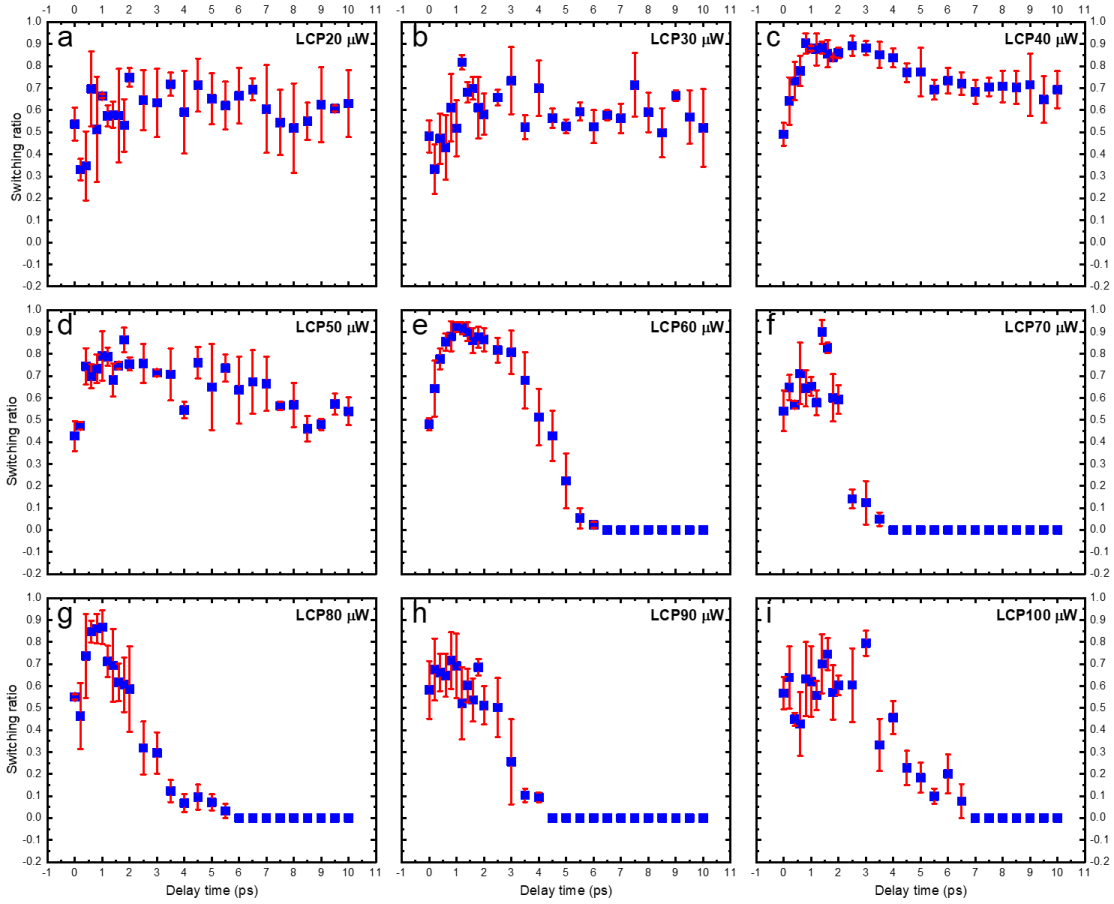

Figure 4.6 The effect of the delay time between the LP and CP on HD-AOS in a Pt/Co/Pt triple layer. All figures have the same total power of $120\ \mu W$, while Each fig shows a different CP and LP power combination.

The MOKE images and the extracted switching ratio of two representative power combinations are displayed in Fig 4.7. The interference of the two pump pulses at the zero-delay point induced a multidomain state, which leads to an approximate 50% switching ratio for every curve in Fig 4.7(c), (d) at the zero-delay point. With the increase of the time delay, the switching ratio increases first and reaches its highest point, approximately 90%, when the time delay is about 1 ps for all the power combinations. However, after the initial rise, the switching rate shows a significant difference of its dependence on the LP and CP time delay between these two power combinations.

For the case of LP power 40 μW ($3.53\,\mathrm{mJ/cm^2}$) and CP power 80 μW, the switching ratio drops sharply when the time delay between the two pulses is longer than 2 ps. It decreases to less than 20% when the time delay is longer than 3 ps as shown in Fig 4.7(c). On the other hand, for the case of LP power 80 μW ($7.06\,\mathrm{mJ/cm^2}$) and CP power 40 μW, the switching ratio stays at its highest value (~90%) for the time delay from 1 ps to 4 ps. When the time delay is longer than 4 ps, the switching ratio drops very slowly and gradually to around 60% up to 300 ps. When the time delay is longer than 300 ps, the switching rate drops dramatically below 50% as shown in Fig. 4.7(d). The gradual decrease in the switching rate between 4 ps to 300ps delay is largely due to the shrinking of the switching area. As shown in Fig. 4.7(b), the width of the central black trace decreased with the increasing of the delay time while the switching rate was calculated within a window of fixed size 20 μm×200 μm. These two different processes are also evidenced in their MOKE images at different time delays as presented in Fig. 4.7(a) and (b), where Fig. 4.7(a), for the case of LP power 40 μW, shows no sign of switching at 6 ps, while Fig. 4.7(b) a clear switching at the same delay time, but with a larger LP power of 80 μW.

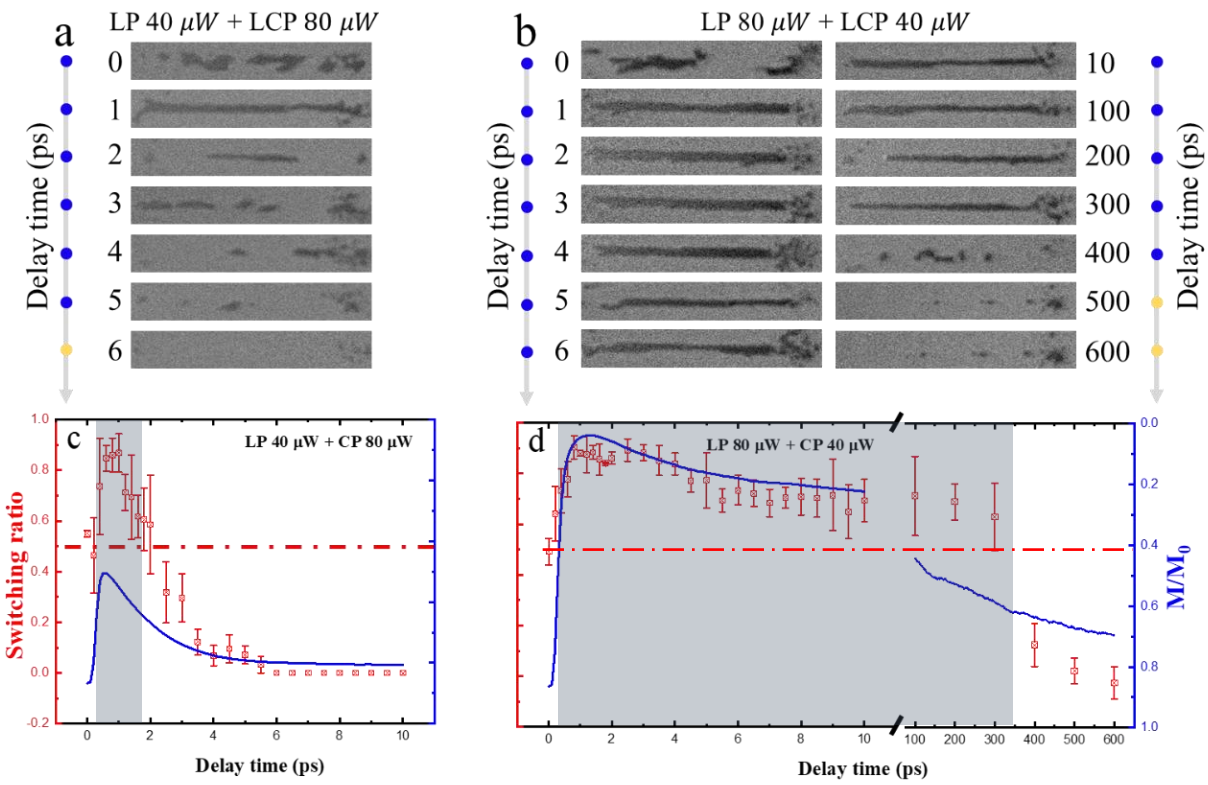

Figure 4.7 HD-AOS in a Pt/Co/Pt triple layer induced by dual-pump as a function of time interval between two pulses. The first pulse is LP and the second is CP. The upper panels show MOKE images of magnetic domains induced under two different combinations of LP and CP powers (a) LP 40 μW + CP 80 μW and (b) LP 80 μW + CP 40 μW under the same total power of 120 μW. The number next to each image indicates the delay time. The red square symbols in the lower panels, (c) and (d), show the corresponding switching ratio vs delay time. The horizontal red-dotted lines indicate a switching ratio of 50%. The superimposed blue lines are the simulated demagnetization curves from the LP pump excitation only, indicating the transient magnetization state before the arrival of the CP pulse.

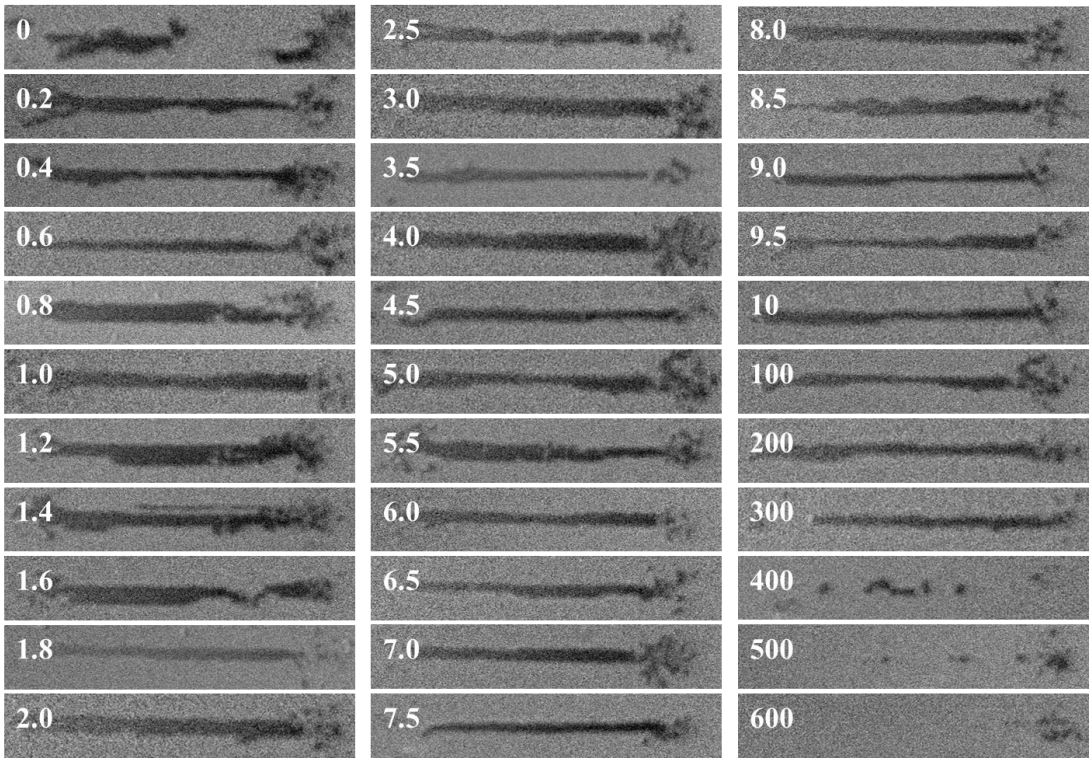

Figure 4.8 MOKE images of magnetic domain induced under the power combination of LP 80 μW+LCP 40 μW, where the number indicates the delay time between these two pumps.

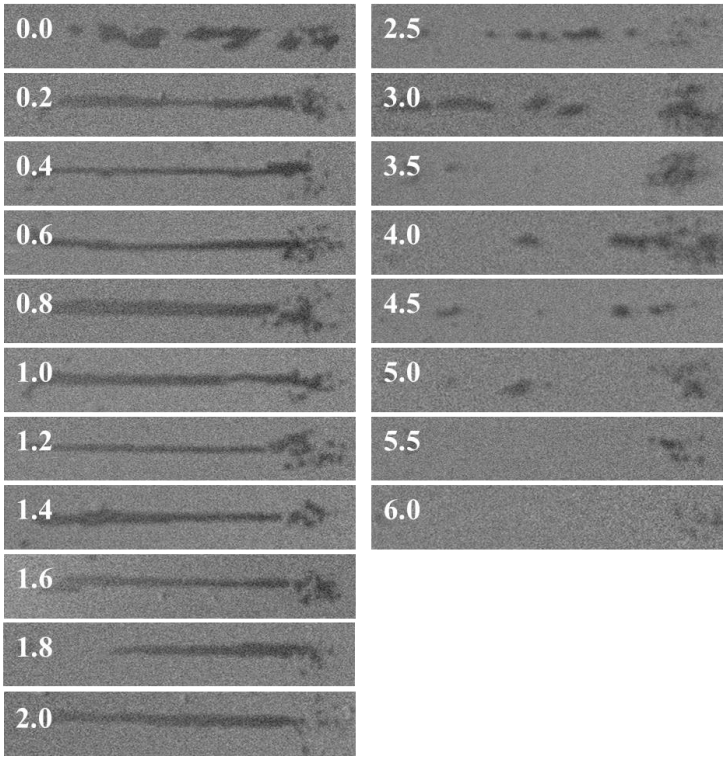

Figure 4.9 MOKE images of magnetic domain induced under the power combination of LP 40 μW+LCP 80 μW, where the number indicates the delay time between these two pumps.

4.3.2 Switching ratio and Light ellipticity

During the image processing, a rectangle of size 20 μm×200 μm covering the central area of laser swiping path was selected from a subtracted MOKE image. A reference intensity is obtained from a chosen rectangle of the same size next to the laser swiping path so as to eliminate the effect from the inhomogeneous illumination on the sample surface during imaging process. This ensures that the reference areas are not exposed to laser excitation, and examples of such reference areas are framed in blue rectangles as shown in Fig 4.10(a), which presents a subtracted MOKE image of three scans obtained under excitation of the same combination $LCP\ 140\ \mu W + LP\ 20\ \mu W$ but with three different times interval in-between. These blue rectangles have the same illumination distributions during imaging process as the corresponding laser scanned areas from which the switching rate is to be abstracted. Therefore, the reference area corresponds to the state with initial magnetization. The average brightness of this blue rectangle is set as a threshold $T_{M\uparrow}$. Then a rectangle of size 20 μm×200 μm covering the central area of laser swiping path next to the blue

rectangle was selected. If a pixel's brightness was higher than $T_{M^{\uparrow}}$, it was considered as non-switched, otherwise it was switched. Then the switching ratio is:

$$R = \frac{the\ number\ of\ switched\ pixels\ in\ a\ rectangle}{the\ number\ of\ total\ pixels\ in\ a\ rectangle} \qquad \text{Equation 4.1}$$

Since we have done this process 3 times, we get an error bar, which gives a point in the curves shown in the previous figures. The distribution of the number of pulse pairs across the width of the scanning track, i.e., the diameter of the focused pump spot, has been calculated based on the size of the pump spot and the laser scanning speed. The relationship between the position across the width versus the number of pulse pairs is plotted in Fig 4.10(b). The red line indicates the region from which the switching ratio has been extracted. The distribution of the number of pulse pairs does not vary significantly within this region.

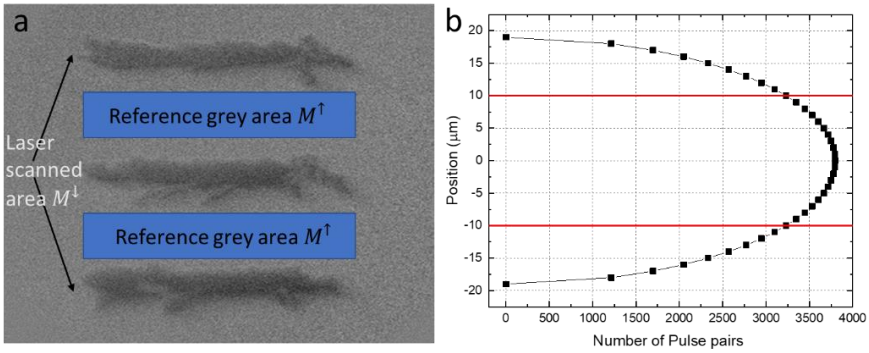

Figure 4.10 (a) The MOKE image of $LCP\ 80\ \mu W + LP\ 40\ \mu W$ at 3 delay times (0.5 ps, 1 ps, 1.5 ps. from top to bottom). The sample was initially magnetized to the $M^{\uparrow}$ direction. For each set of scans, we chose the area in the blue rectangle that is not exposed to the laser as the reference area. (b) The distribution of the number of pulse pairs across the width of the scanning track, the red line indicates the calculated switching ratio area.

As the interference occurs in the zero-delay point, we further explored the single pump light ellipticity for the HD-AOS and results are shown in Fig 4.11. The light ellipticity is tuned by the quarter-wave plate, and the number in the left of Fig 4.11(a) indicates the quarter-wave plate's angle. Here $45°$ gives the CP light, and $0°$ gives the LP light. The laser power is fixed at $120\ \mu W$ in this experiment. The elliptically polarized light can be regarded as a combination of

LP and CP. In these experiments, as the LP and CP arrived at the same time, both CP and LP's heating could not assist the switching due to the in-situ helicity effect and the lagging heating effect. Therefore, the switching ratio decreases with the CP's ratio decreases as shown in Fig 4.11(b).

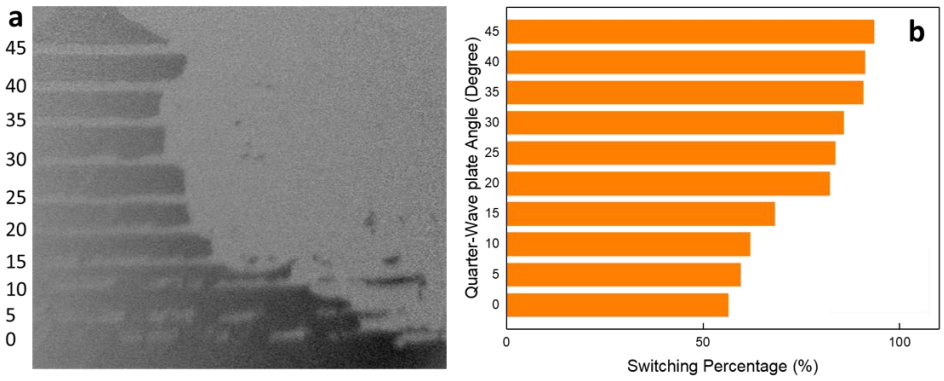

Figure 4.11 (a) Magneto-optical Kerr image of all optical switching in a Pt (2 nm)/Co (0.6 nm)/Pt (2 nm) thin film exposed to 120 μW RCP laser with different light ellipticity, which is changed by rotating the angle of the quarter-wave plate as labeled on the left. (b) The corresponding AOS switching ratio of (a).

4.4 Time-resolved MOKE scans and simulations

Atomistic spin dynamics modelling combined with a two-temperature model has been employed to simulate the demagnetization rate and magnetization recovery after the LP pulse for both cases, i.e., of 40 μW and 80 μW, and the results are superimposed on their switching rate curves in Fig 4.7 (c) and (d), respectively. The atomistic simulation of the ultrafast demagnetization in this work is provided by Vampire 5.0 package [148]. The energy of the system is described by the following Hamiltonian, which includes all the energy contribution to the magnetic behavior of the system, including the Heisenberg form of exchange:

$$H = -\sum_{i<j} J_{ij}\vec{S_i}\cdot\vec{S_j} - \sum_i k_{eff}^i\left(\vec{S_i}\cdot\hat{e}\right) - \mu_0\sum_i \mu_S^i\vec{S_i}\cdot\overrightarrow{H_{app}} \qquad \text{Equation 4.2}$$

Where the J_{ij} is the exchange interaction between the spins on site i and j, K_{eff} is the uniaxial anisotropy energy on site i along the axis $\hat{e}$, μ_S^i is the atomic spin moment on the atomic site i in

unit of μ_B and μ_0 is the permeability constant. The parameters for the atomistic simulation are obtained from the literature [149, 150] which has been listed in the Table 4.1.

Exchange strength	6.064×10^{-21} J per link
Anisotropy	1.1×10^{-24} J per atom
Magnetic moment	1.72 μ_B
Damping coefficient	0.1
Lattice constant	2.73 Å
Electron heat capacity	699 J/(m^{3}K)
Phonon heat capacity	3.15×10^{6} J/(m^{3}K)
Electron phonon coupling	2.9×10^{17} J/(m^{3}sK)

Table 4.1 Material parameters used in the atomistic simulation.

The dynamics of spin systems are determined by the Landau–Lifshitz–Gilbert (LLG) equation with Langevin dynamics:

$$\frac{\partial \vec{S_i}}{\partial t} = -\frac{\gamma}{(1+\lambda^2)}[\vec{S_i} \times \overrightarrow{H_{eff}^i} + \lambda \vec{S_i} \times (\vec{S_i} \times \overrightarrow{H_{eff}^i})] \quad \text{Equation 4.3}$$

where γ is the gyromagnetic ratio and λ is the microscopic Gilbert damping parameter, the $\overrightarrow{H_{eff}^i}$ is the net magnetic field with an additional white noise term as:

$$\overrightarrow{H_{th}^i} = \Gamma(t)\sqrt{\frac{2\lambda k_B T}{\gamma \mu_S \Delta t}} \quad \text{Equation 4.4}$$

where k_B is the Boltzmann constant, T is the temperature of the electron system, Δt is the integration time step, and $\Gamma(t)$ is the Gaussian white noise term which representing the thermal fluctuations on each atomic site. Then the effective field $\overrightarrow{H_{eff}^i}$ in the LLG equation with thermal term can be explain as:

$$\overrightarrow{H_{eff}^i} = -\frac{1}{\mu_S}\frac{\partial H}{\partial \vec{S_i}} + \overrightarrow{H_{th}^i} \quad \text{Equation 4.5}$$

The three-temperature model is indeed often used to explain the ultrafast demagnetization. Unlike the 4f electrons, for the 3d electrons (in our case is the Cobalt's 3d electrons), the time lag between the temporal profile of spin-temperature and electron-temperature after femtosecond laser excitation is very short, about several tens to a few hundreds of femtoseconds This time lag stays the same when we vary the power of the LP and CP pulses, so it won't be reflected in our comparison results. Therefore, to simplify the analysis, we consider the spin system is coupled to the temperature profile of the electrons in the two-temperature model. The energy transfer for the electron-spin system to the lattice system is mediated by the phonons, which takes about 1.6 ps for the spin-electron-lattice system to reach a thermal equilibrium state in Co/Pt multilayers as in ref [103, 145, 146]. The electron system temperature in the atomistic simulation is calculated by a simplified two-temperature model [151].

$$C_e \frac{\partial T_e}{\partial t} = -G_{e-p}\left(T_e - T_p\right) + P(t) \qquad \text{Equation 4.6}$$

$$C_p \frac{\partial T_p}{\partial t} = -G_{e-p}\left(T_p - T_e\right) \qquad \text{Equation 4.7}$$

Where C_e, C_p are the electron and lattice heat capacities. T_e, T_p is the temperature for electron and lattice (phonon), $G_{e\text{-}p}$ is the coupling constant between electron and lattice. *P(t)* describes the input laser power as a function of time and follows a Gaussian pulse with the height being proportional to a laser fluence parameter F_{eff} and a width t_0. *P(t)* can be explained as:

$$\mathrm{P(t)} = F_{eff} \cdot e^{-\frac{(t-3t_0)^2}{{t_0}^2}} \qquad \text{Equation 4.8}$$

In the atomistic simulation, the system size has been set as 50 nm * 50 nm * 0.6 nm with periodic boundary conditions in x and y-direction. The environment temperature is set at 293 K. While in this simulation, we only consider the laser's heating effect, and the duration of the heating pulse is 150 fs with a gauss profile. The fluence was set corresponding to the AOS result, where we found $120\ \mu W$ laser pulse was the minimum fluence to fully demagnetize the sample, and hence, we set the first fully demagnetized fluence in the simulation as $120\ \mu W$. To eliminate the thermal fluctuations, all curves are the average of 10 times simulations with different instances of the random number generator seed. Fig 4.12 (a) and (b) show the simulation results within the first 10 ps and 800 ps after single pump excitation with laser power varying from $40\ \mu W$ to $120\ \mu W$.

The corresponding experimental time-resolved MOKE scans are also presented in Fig 4.12(c) and (d). The simulation and the experimental data are in very good agreement. With the increase of the laser fluence, the ultrafast demagnetization increases and the relaxation time also increases from several picoseconds to nanosecond. Both the experimental and simulation results support our explanation for double-pump AOS results.

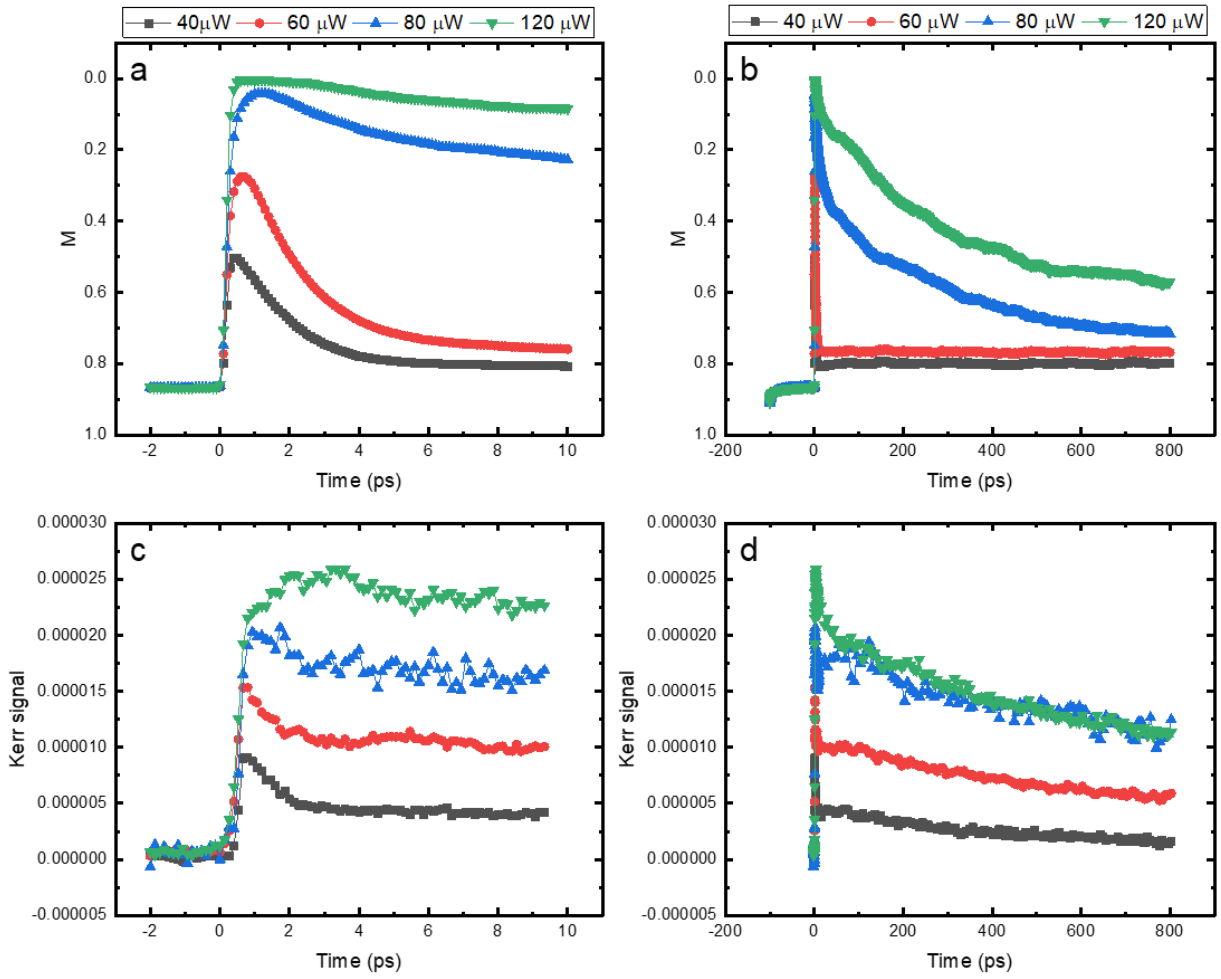

Figure 4.12 Time-resolved ultrafast demagnetization excited by a single laser pump with various laser power. (a) and (b) are simulations by two-temperature model, where (a) shows a zoomed-in view of the first 10 ps, and (b) shows the whole 800 ps duration. (c) and (d) are the time-resolved MOKE Kerr rotation excited by linearly polarized pump pulses with various power, where (c) zooms in the first 10 ps, and (d) shows the whole scans of 800 ps duration.

To simplify the analysis, we consider the spin system is coupled to the temperature profile of the electrons in the two-temperature model. It shows that the magnetization recovery (spin cooling) time after laser excitation increases from a couple of picoseconds to a few hundreds of picoseconds as the LP power increases from 40 μW to 80 μW, which was also observed in the time-resolved MOKE measurements of the sample shown in Fig 4.12. A red dotted horizontal line is drawn at 50% switching ratio (left hand y axis) in both Fig 4.7(c) and (d). In Fig 4.7(c), HD-AOS occurs when the 80 μW CP pulse arrives within a time delay between 0.2 to 2 p, shaded in grey. In Fig. 4.7(d), HD-AOS occurs when the 40 μW CP pulse arrives within a time delay between 0.2 to over 300 ps, also shaded in grey. Comparing the sample magnetic states within these two grey areas where HD-AOS is achieved, one can see a common minimum of the sample magnetization of around 60% of the saturation magnetization. This indicates that the demagnetized state upon which the CP pulse impinges is a key factor to achieve HD-AOS.

4.5 Timescales and contributions of the Heating and helicity effects

However, the essential role of heating in HD-AOS on its own cannot explain the dramatically different time-delay dependence between the above two cases since the second CP pulse also heats up the sample, which reduces the magnetization. This difference suggests that the action of the helicity effect comes to an end before the spin temperature reaches its second peak caused by the CP-pulses.

To clarify this picture, the two-temperature model has been applied again to simulate the demagnetization rate and magnetization recovering excited by both the LP and CP pulses. Fig 4.13(a) and (b) show the case when two pulses are 5 ps apart. A red dashed horizontal line is drawn at 60% of the saturation magnetization value, which is the minimum magnetization observed in the two grey areas in Fig 4.7. The spin flip energy barriers related to the spin temperatures are also added and represented by E_{fa}^{t} and E_{fb}^{t}, respectively, where t represents the delay time. To identify the lag between the helicity and heating effects, we show the corresponding E_{f}^{t} at four time points namely when: the first pulse arrival time ($t = 0$), the first demagnetization peak occurs ($t = 1\ ps$), the second pulse arrival time ($t = 5\ ps$), and when the second demagnetization peak occurs ($t = 6\ ps$). One can see that in the case of Fig 4.13(a) with the LP 80 μW + CP 40 μW pulse combination, at 5 ps delay time, the sample's magnetization has only recovered 20%. This corresponds to a lower energy barrier E_{fb}^{5} between $M^{\uparrow}$ and $M^{\downarrow}$ states upon the arrival of the

40 μW CP pulse, and HD-AOS takes place in this case. In the case of Fig 4.13(b) with LP 40 μW + CP 80 μW pulse pair, at 5 ps delay time, the sample magnetization recovers to around 80% of its saturation value. This corresponds to a high energy barrier E_{fa}^{5} between $M^{\uparrow}$ and $M^{\downarrow}$states upon the arrival of the 80 μW CP pulse and HD-AOS doesn't take places. This is because the CP pulse's heating effect takes more than 0.3 ps to demagnetize the sample's magnetization to its second peak. During the CP pulse duration, the sample's magnetization is only reduced to 70% of its saturation value., as marked by two short vertical dash lines in Fig 4.13(b). The only explanation for this observation is that the onset time of the helicity effect from the CP pulse is instant, and the duration of the helicity effect is less than 200fs which is close to the laser pulse width of 150 fs. Even though the energy barrier E_{fa}^{6} is reduced further by the heating effect of the CP pulse itself, the helicity effect has already disappeared at this point, and HD-AOS cannot be triggered anymore.

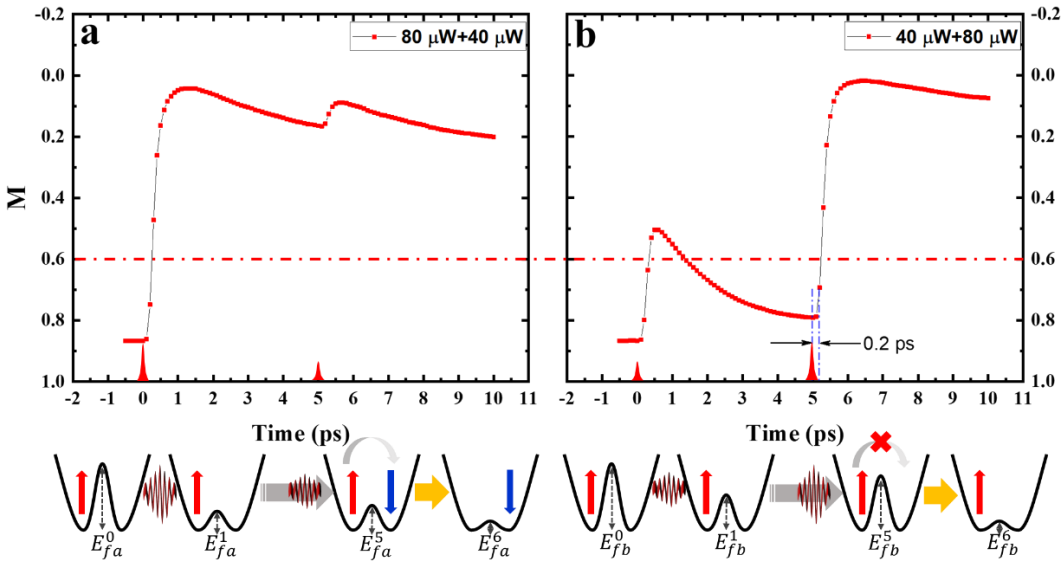

Figure 4.13 Simulation of dual-pump induced magnetic switching process. The temporal profiles of the simulated demagnetization induced by both LP and CP pulses at 5 ps time delay for two power combinations, (a) LP 80 μW+ CP 40 μW and (b) LP 40 μW+ CP 80 μW. Two short vertical dashed lines (in blue) in (b) mark 0.2 ps time interval after the CP pulse excitation. The effective energy barriers (E_{fa}^{t}, E_{fb}^{t}), determined by the transient spin temperatures, between $M^{\uparrow}$ states and $M^{\downarrow}$ states at four-time delays (t ps) are illustrated for both cases.

We have further investigated the relationship between HD-AOS switching ratio and laser ellipticity using a single pump and the results are included in Fig 4.11. The switching ratio was found to decrease as the laser polarization changes from circular to linear. This is consistent with a previous finding on laser-induced domain wall motion where wall displacement decreases as laser polarization changes from circular to linear [34]. For these single pulse cases, the LP and CP photons arrived at the same time, and the heating effect from the LP photons lags and thus the CP photons fail to achieve HD-AOS. This could account for the fact that HD-AOS has not been observed in a wider range of material systems, because, generally, ultrafast laser heating effects lag behind its helicity effect. This also explains a previous observation that a longer laser pulse duration gives a higher switching ratio under the same laser power AOS [152]. As shown in Fig 4.12, the higher laser fluence takes a longer time to reach the highest demagnetized state as pointed out previously [149]. With the dual-pump laser pulses, we expect that HD-AOS would occur in many other magnetic materials where the transient magnetization states needed for the CP lighted driven HD-AOS can be achieved by controlling the strength of the LP pulse and the delay time.

As shown in Fig 4.14(a), the first LP pulse increases both $M^{\uparrow}$ and $M^{\downarrow}$ domains' temperature but not close to the T_c. While due to the MCD effect, the second CP pulse heats the $M^{\uparrow}$ domain's temperature closer to T_c. Once it switched to $M^{\downarrow}$ domain, it absorbs less CP photons, and makes its temperature away from T_c. However, this phenomenological mechanism should not sensitive to the time sequence of the CP and LP pulses. As shown in Fig 4.14(b), if the CP pulse arrived first, it still gives a temperature difference of $T_1^{\uparrow}$ and $T_1^{\downarrow}$. And then the second LP pulse increases both domains temperature, but keeps this temperature difference. Then the HD-AOS still can happen. Also, in Fig 4.14(c), the elliptical polarized pulse can be regarded as a mixture of CP and LP pulses, based on the MCD effect, it still induces a temperature difference of $M^{\uparrow}$ and $M^{\downarrow}$ domains. However, in our results, the $60\ \mu W\ LP + 60\ \mu w\ CP$ (LP arrived first) gives the same AOS ratio as the $120\ \mu W$ CP pulse, but if they arrived at the same time (elliptical polarized pulse) the switching ratio is lower than the former. While the AOS is not observed if CP pulse arrived earlier than LP pulse. Moreover, in our double pump experiments (especially the $100\ \mu W$ LP + $20\ \mu W$ CP), the temperature difference between these two domains is much smaller than using a single $120\ \mu W$ CP pump, while these two experiments give a nearly same switching ratio. Of course, this superficial explanation ignores the spin heat capacity (C_s) changes with the spin system's temperature (T_s). Also, MCD is

introduced to explain laser-induced domain wall motion, which may also suitable to explain our results [34]. Finally, we would like to emphasize that to fully explain our results based on MCD mechanism, several more effects should take into consideration.

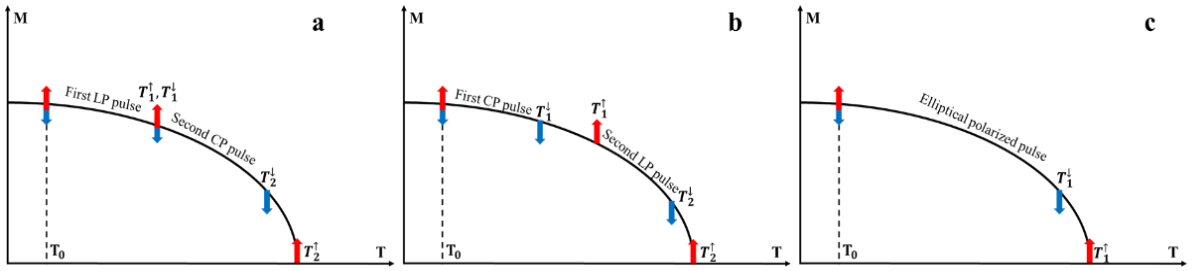

Figure 4.14 The HD-AOS model based on the MCD mechanism to explain our experimental results. (a) The LP pulse arrived first, and then the CP pulses. (b) The CP pulse arrived first, and then the LP pulse. (c) Using elliptical polarized pulse.

IFE effect could also explain our results, just like the heat-assisted magnetic recording mechanism. However, the origin of the IFE is much more complex. The standard IFE induced magnetization in a plasma is given by the expression $M(t) = -\gamma E^*(t) \times E(t)$ and its direction is parallel to the axis of propagation of the wave and its sign depends on the chirality of the wave [122]. The duration of the IFE field is still under debate. According to this equation, IFE field's duration is the same as the laser pulse duration. However, in all modern measurements of the ultrafast laser's IFE, the magnetization remains altered and takes some time to stabilize, and therefore several later papers discussed that this equation is not suitable for the ultrafast laser and the duration is longer than laser pulses [120, 124]. Here, just like the previous IFE paper discussed [30], we shall roughly consider the IFE effect provides a magnetic field.

In our results, the AOS happens when the delay time between LP and CP is only 0.2 ps. It indicates that HD-AOS only depends on the spin system's temperature, since the lattice temperature is much slower than the spin system's temperature. Once the spin temperature increased, the IFE field could switch the spin. But as we indicated in Fig 4, for $LP\ 80\mu W + CP\ 40\ \mu W$ and $LP\ 40\mu W + CP\ 80\ \mu W$, their demagnetization will reach the same after about 1 ps. But the former switched. To explain this difference, we suggest that the AOS happens when the CP pulses arrived at the sample, and the duration of the IFE field has the same timescale of pulse duration If the IFE field duration is longer than 1 ps, and the $80\ \mu W$ CP pulse will provide a stronger IFE field, and it has no reason that the later one did not switch.

We have tried the single pulse pair shots, and we did not observe a clear switching (it either has no change or induced a multidomain state.) Also, the dual pump TR-MOKE has done, but

we still did not observe a magnetic switching. However, a recent report in the arXiv, see ref. [153] tried the dual-pump HD-AOS, by using a longer duration CP pulse (up to 3ps) and successfully reduced the pulse number required for HD-AOS. This is consistent with our results, as we mentioned, the helicity effect only exists close to the laser pulse duration. Their results also suggest that by decreasing the magnetization and increasing the laser pulse duration (helicity effect's duration), HD-AOS could be achieved at single pulse pair.

4.6 Conclusions

In this chapter, we have applied dual-pulse laser excitation to identify the contribution and time dependence of the heating and helicity effects on HD-AOS in a Pt/Co/Pt triple layer. We have shown that pre-heating plays an essential role in HD-AOS. The laser power required for HD-AOS via the helicity effect was shown to be very low when the magnetization is close to a fully demagnetized state. By varying the time delay between LP and CP pulses with different energy combinations, we have demonstrated unambiguously that the helicity effect, which gives rise to the deterministic helicity-induced switching, occurs instantly upon laser excitation, and only exists over the laser pulse duration. This work has disentangled the heating and helicity effects and revealed their timescales in helicity-dependent all-optical magnetization switching. At the same time, the unique LP/CP dual-pump scheme makes the manipulation of HD-AOS feasible, which provides a promising way for achieving HD-AOS in a wide range of material systems.

Chapter 5 Tuning the power range in helicity-dependent all-optical switching

5.1 Introduction

As a candidate for the next-generation information storage technique, the energy efficiency and switching accuracy of AOS are essential issues. The Gd based materials have achieved single shot AOS, showing an incredible energy efficiency. For example, it was reported by Lalieu *et al.* that single pulse AOS was observed in Pt/Co/Gd stacks with a remarkable low threshold fluence of $\approx 1.2\, mJ/cm^2$ [22], which is more than 10 times less than the HD-AOS in Pt/Co/Pt stacks [23, 34]. Based on the mechanism of single-shot AOS in GdFeCo, Yang *et al.* found picosecond current pulse also can switch the magnetic direction in a GdFeCo cell with only 4 fJ [18]. Although the HD-AOS is still a multi-pulse switching with a much higher threshold fluence, the rare-earth element Gd is unessential for HD-AOS materials. And mining rare-earth elements is laborious and environment unfriendly work, hence, it is important to study the HD-AOS without Gd. In this chapter, we have further studied HD-AOS from two aspects, experiments and first principle calculation, to explore the approaches to tune the AOS power ranges and switching ratios. The samples used are the typical HD-AOS materials: Pt/Co/Pt stacks as in the previous chapter, but with different Pt and Co thicknesses. The HD-AOS power window and switching ratio have been studied in all of these samples. We have also calculated a similar sample structure by DFT, and the calculation results provide information about magnetic moment distribution and spin-orbit coupling energy in each atom layer.

5.2 Methodology

5.2.1 Experimental part

Here we studied the HD-AOS power window and its switching ratio in two series of samples. All of them have the same layer structure: Glass/Ta (5 nm)/Pt (t_{Pt} nm)/Co/ (t_{Co} nm)/Pt (t_{Pt} nm). The first series of samples have the Pt layers thickness of 2, 5, and 10 nm and the same Co thickness of 0.6 nm. The second series samples have the Co layers thickness of 0.6, 0.8, 1.0, 1.2, 1.4 and 1.6 nm with the same Pt layer thickness of 2 nm. These samples were deposited on Corning glass with a thickness of 0.13 nm at room temperature by DC magnetron sputtering from separate Co, Pt, Ta targets. The base pressure of the sputtering system was better than $4 \times 10^{-5}\, Pa$, and the working Ar pressure was $0.5\, Pa$. The sputtering rate with a DC current of 40 mA was 0.41, 0.84, and 0.48 $Å/s$ for Ta, Pt, and Co, respectively. The first 5 nm Ta

buffer layer was employed to improve the smoothness of the substrate[81], the Pt/Co interface smoothness and the (111) orientation, thereby enhancing the perpendicular magnetic anisotropy (PMA) of the Co layer. For all the samples studied in this chapter have the perpendicular magnetic anisotropy confirmed by both the MOKE image measurement and VSM measurement. The top Pt layer protects the sample from oxidation.

The experimental set-up is the same as we used in chapter 4. The laser used in all experiments has a central wavelength of 800 nm with an approximately pulse duration of 100 fs, which is generated by the Ti:sapphire laser amplifier system. For all these experiments, the sample was magnetized to a multidomain state, with a domain wall in the field of view. And as shown in Fig 5.2, the white part of the image is the $M^{\uparrow}$ state, and the black part of the image is the $M^{\downarrow}$ state. Then the laser scan from left to right with the velocity of $10\ \mu m/s$ and the acceleration is $10\ \mu m/s^2$. After that, the first raw image image01 was taken. Then the sample was magnetized to the $M^{\uparrow}$ state, and the second raw image02 was taken. To improve the image contrast and eliminate non-magnetic signal, we did the subtraction of image01 and image02, and then we multiplied the subtracted image by a gain factor of 200. Then we used the same method in section 4.3.2 to calculate the switching ratio of each subtracted image.

5.2.2 First-principals calculation

First-principles plane-wave calculations are widely used to predict and explain the electronic and magnetic properties. In this section, the numerical plane-wave calculations were performed by using the Vienna Ab initio Simulation Package (VASP) [154-156] at Viking-University of York Research computing cluster. Structure optimization is always the first step of the calculation, which gives rise to a reconstruction of atomic structure and outputs a relatively stable ground state structure. Two processes are included in the structure optimization, ionic relaxation iteration and electronic relaxation iteration. Electronic relaxation iteration is nested in ionic iteration, and the next ionic relaxation step is not performed until the electronic convergence criterion is reached. The parameter specifies the global break condition for the electronic iteration is EDIFF, in our calculation it is set EDIFF = 10^{-6}. And the ionic iteration's convergence is dependent on the total free energy change between two ionic relaxation steps. The parameter that specifies the global break condition for the structure optimization is the EDIFFG, in our calculation it is set EDIFF = -10^{-4}. The generalized gradient approximation (GGA) exchange-correlation potential using Perdew-Burke-Ernzerhof (PBE) functional [157, 158] is used for all calculations in this section. And the structure uses

periodic boundary conditions. The kinetic energy cutoff of 500 eV is set for the plane-wave basis set. The calculated valence configurations for Co are $3d^7 4s^2$ and for Ni are $3d^8 4s^2$ and for Fe are $3d^6 4s^2$ and Pt are $5d^9 6s^1$. Fig 5.1 (a) shows the structure we investigated, and this figure is plotted by the VESTA software [159]. Two Co layers are placed on the body centre cubic (BCC) Pt (111) surface, where the Pt atom's position is fixed, and the Co atom's position is free. The Pt layer's structure is obtained from previous experimental results [160-162]. This structure has 15 layers with 13 layers of Pt. In the self-consistent potential and total-energy calculations, they have been performed with a *k* mesh of $12 \times 7 \times 1$. A lattice mismatch is existed in both experimental measurements and calculations as the radius of Co atom is much smaller than Pt. To simulate the experimental results, we set the *c*-axis as free and fix the *a*, *b*-axis, and calculated the system's free energy as a function of the lattice constant *c* as shown in Fig 5.1 (b). The structure with the lowest free energy will be chosen for the next magnetic properties calculations. This process is just like the growth process with the lattice mismatch in the in-plane direction.

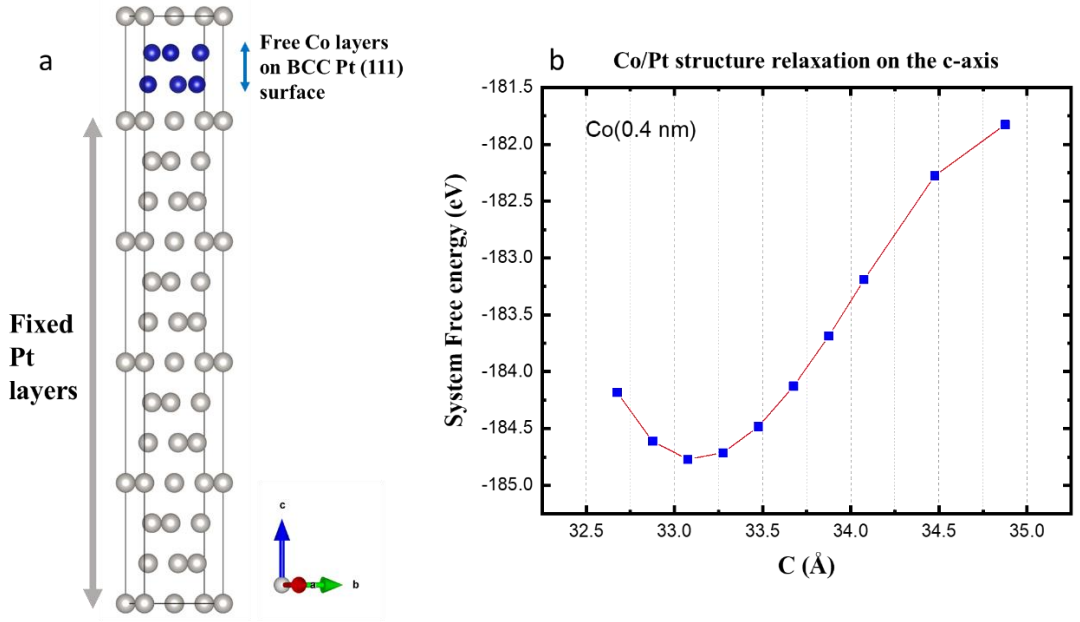

Figure 5.1 (a) The front view of the calculated Co/Pt multilayer structure. 2 Co layers (Blue balls) are placed on the top of (111) surface of 13 layers of Pt (Silver balls) with a BCC structure. Co layers are free while Pt atoms' positions are fixed. And the lattice constants a and b are fixed, and c is free. (b) The system free energy as a function of lattice constant c.

After the first structure optimization step, the structure with the lowest system energy is used for calculating magnetic properties. In this step, the spin-orbit coupling is involved in the

calculation, which will also turn off the collinear calculation and all symmetry. As spin-orbit coupling changes the electron density, old wave functions from step 1 are not read, but we recalculated the electron density from the beginning with the parameter ISTART = 0. 400 energy bands are included in the calculation, and the partial occupancies orbitals are using the Fermi smearing with a width of the smearing in 0.01 eV. As we discussed in the previous section, all the magnetic interactions are very sensitive to the electron-electron distance, and hence, the GGA+U (or LDA+U) parameters play an important role in the magnetic properties' calculation. Hubbard *U* correction is adopted to diminish the error, and the parameter GGA+U determined Hubbard *U* correction is fixed except for specific mentions at 4.2 eV for Co, 4.1 eV for Fe, 4.15 eV for Ni, and 2.9 eV for Pt. The GGA+J parameter specifies the strength of the effective on-site exchange interactions, and it is fixed at 0.8 eV for Co, 0.78 eV for Fe, 0.82 eV for Ni and 0.5 eV for Pt.

5.3 HD-AOS Results

5.3.1 Experimental part

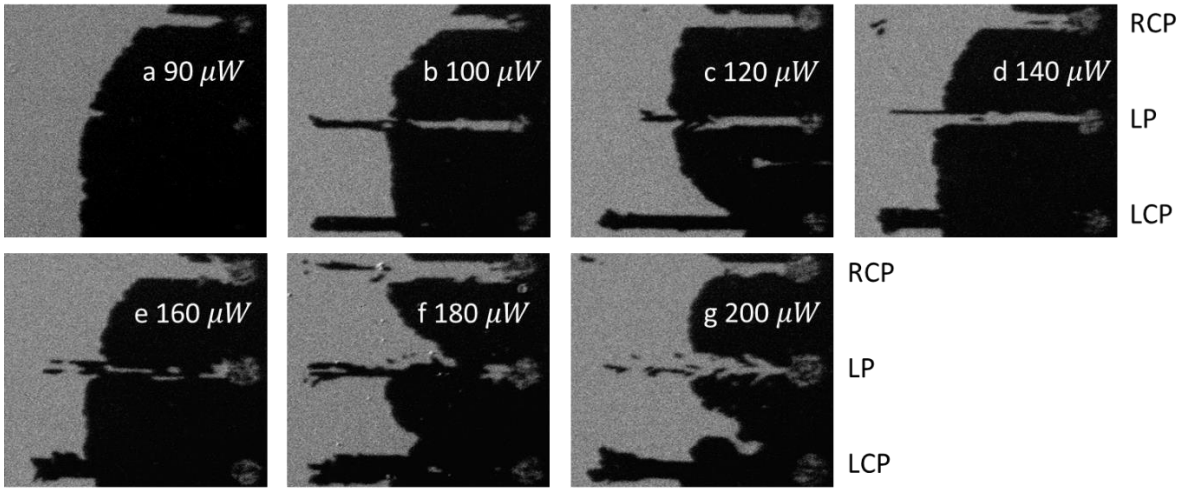

Figure 5.2 Magneto-optical response in zero applied magnetic field of Glass/Ta (5nm)/Pt (2 nm)/Co (0.6 nm)/Pt (2 nm) samples to various laser power and different laser polarization.

Three laser polarization RCP, LP and LCP were used to confirm the helicity dependence. And it is obviously seen from Fig 5.2, that the RCP laser switches the black $M^{\downarrow}$ state to the white $M^{\uparrow}$ state in contrast to the LCP laser. While the LP laser, it induces a multidomain state. It is easy to get lower limit power of HD-AOS about the HD-AOS laser power window. But for the upper limit power of HD-AOS, the situation is more complicated. In most of the case, although HD-AOS was observed, we noticed that when we use a magnetic field very close to the

sample's coercivity, the domain wall motion is always slower in the area exposed to the laser. Further increase of the laser fluence results in a significant coercivity increase even though a fully HD-AOS was observed. As the laser has changed the magnetic properties of the sample, we cannot consider it is a repeatable HD-AOS. Therefore, the upper-limit power of HD-AOS is the laser power that does not change the coercivity of laser scanned area.

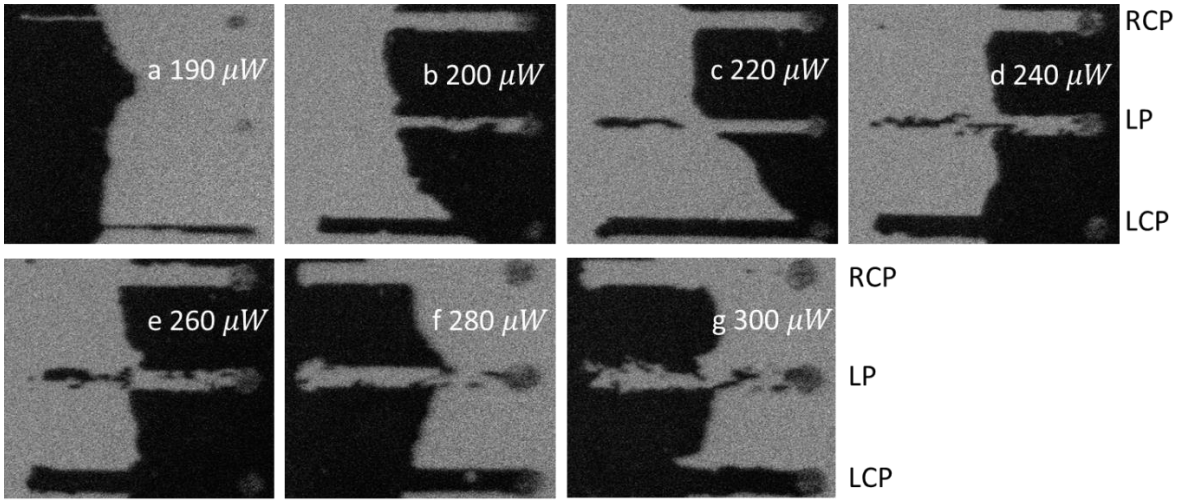

Figure 5.3 Magneto-optical response in zero applied magnetic field of Glass/Ta (5nm)/Pt (5 nm)/Co (0.6 nm)/Pt (5 nm) samples to various laser power and different laser polarization.

The HD-AOS laser power range for different Pt thicknesses shows a significant difference, as shown in Fig 5.4 (a). With the Pt thickness increasing, the HD-AOS power increases, which is due to the Pt layer's high reflection and low absorption. However, the switching ratio of the 5 nm Pt layer is the highest in all the samples. The laser scanned area shows two clear boundaries, as shown in Fig 5.3, and between these boundaries, the switching ratio is very close to 100%. But when the Pt layers' thickness increases to 10 nm, the switching ratio has a slight decrease. Also, the laser power for HD-AOS is very high, which is not energy efficient.

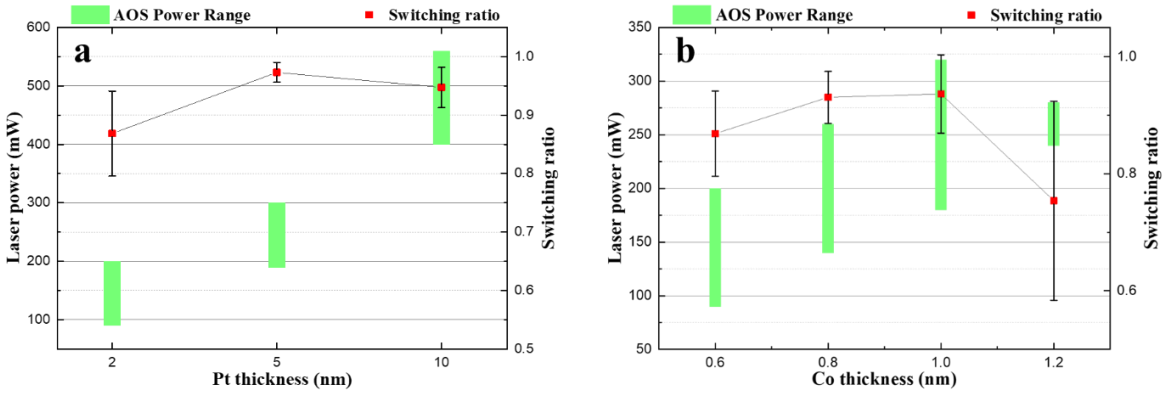

Figure 5.4 Magneto-optical response of Pt/Co/Pt samples to circular polarization light and varying powers. The green bar shows the power window for AOS, and the red dot shows the average switching ratio when AOS happened in the power window. (a) The switching ratio and AOS power range as a function of Pt layers thickness. (b) The switching ratio and AOS power range as a function of Co layers thickness.

As shown in Fig 5.4 (b), the AOS power increases with the Co thickness increase. The switching ratio reaches its highest for Co thickness of 0.8 and 1.0 nm. Then the switching ratio drops obviously for Co thickness of 1.2 nm. And no HD-AOS was observed for Co thickness of 1.4 and 1.6 nm. Fig 5.5 shows the magneto-optical response of 1.4 nm Co sample to various laser power. No difference was observed for different laser polarization at $160\,\mu W$ and $200\,\mu W$ as seen in Fig 5.5 (a) and (b), LCP, LP and RCP all induce a multidomain state without any differences. No helicity dependent difference was observed until the laser power up to $300\,\mu W$. In Fig 5.5 (c), the LCP laser switches the white $M^{\uparrow}$ state to the black $M^{\downarrow}$ state, same as the previous results. However, the RCP laser scanned area is not uniform, the outer boundaries were switched to the black $M^{\downarrow}$ state, but the inner is a multidomain state. And when we used a magnetic field to remagnetise the sample, we found that these areas cannot be switched with the magnetic field up to the limit of our electromagnet's magnetic field (900 Oe), while the sample's original hysteresis is only 90 Oe. We suggest that this phenomenon is due to the fact that the laser's heating effect has permanently changed the sample structure. Since the Co/Pt multilayer structure is not a thermal equilibrium state, the laser's heating gives Co and Pt atoms enough energy to reach this state, such as the $CoPt_3$ alloy state, which has a hysteresis of over 1000 Oe [163]. Finally, one could expect that the HD-AOS in the sample can be achieved at much higher laser power. The helicity effect may switch the magnetic

direction. However, as the laser's heating effect and helicity effect is entangled, the heating effect will demagnetize it again. And therefore, the HD-AOS power window was narrowed.

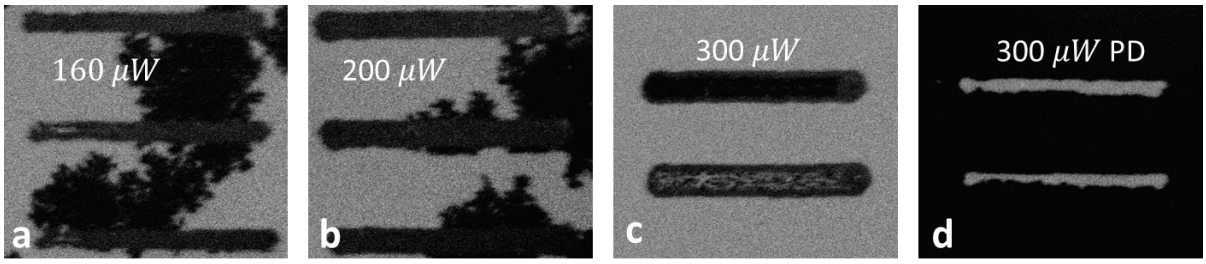

Figure 5.5 Magneto-optical response of Glass/Ta (5 nm)/Pt (2 nm)/Co (1.4 nm)/Pt (2 nm) samples to various laser polarization and power. (a), (b) The laser's polarization from top to bottom is RCP, LP and LCP. And no HD-AOS is observed for the laser power of (a) $160\ \mu W$ (b) $200\ \mu W$. (c) $300\ \mu W$ LCP and RCP (from top to bottom) are used. The laser scanned area shows a difference for LCP and RCP at this laser power, but as shown in (d), this area's hysteresis has permanently increased.

5.3.2 DFT part

For a better understanding of the experimental results, the first-principal calculation in the same structure was done. In most systems, the DFT calculation gives a reliable lattice structure and band structure. However, for the system containing d and f electrons, especially transition metal oxides and nitride compounds, the normal DFT calculation (GGA/ LDA) always cannot give a 'right' result. Even the qualitative judgment of metal/insulator is often wrong. The bandgap of insulators and semiconductors given by LDA or GGA calculation is always smaller than experimental results, and the highest occupied orbital is higher than the Fermi level. Even more, those highest occupied orbitals come from transition metals' d and f orbitals. So, why can the LDA and GGA calculations not deal with the d and f electrons? Firstly, we shall discuss the localized versus itinerant electrons. Since we are considering the distance between the electron and the nucleus, we should separate the time-independent Schrödinger equation:

$$-\frac{\boldsymbol{p}^2}{2m}\psi(\boldsymbol{r}) + V(\boldsymbol{r})\psi(\boldsymbol{r}) = E\psi(\boldsymbol{r}) \qquad \text{Equation 5.1}$$

into two parts, the radial part and the angular part, respectively. We rewrite the electron momentum operator $\boldsymbol{p} = -i\hbar\boldsymbol{\nabla}$ in spherical polar coordinates:

$$\boldsymbol{p}^2 = -\hbar^2\frac{\partial^2}{\partial r^2} - \frac{\hbar^2}{sin\theta}\left(\frac{\partial}{\partial\theta}sin\theta\frac{\partial}{\partial\theta}\right) - \frac{\hbar^2}{sin^2\theta}\frac{\partial^2}{\partial\phi^2} \qquad \text{Equation 5.2}$$

Here, the first term on the right side is the radial part p_r^2, while the rest of the terms is the angular part p_ϕ^2. Corresponding to the classical mechanics, the angular moment part $p_\phi^2 = \boldsymbol{L}^2/r^2$. And $\boldsymbol{L}$ is the angular moment operator, in quantum mechanics, it has the following eigenvalue of

$$\boldsymbol{L}^2 = l(l+1)\hbar^2 \qquad \text{Equation 5.3}$$

where l is the angular quantum number. Also, the total wavefunction is presented in the spherical polar coordinates:

$$\psi_{n,l,m}(\boldsymbol{r}) = R_{n,l}(r)Y_{l,m}(\theta,\phi) \qquad \text{Equation 5.4}$$

Here, n is the principal quantum number, l is the angular quantum number, and m is the magnetic quantum number. Then the radial part of the Schrödinger equation's radial part is given by:

$$-\frac{\hbar^2}{2m}\frac{d^2}{dr^2}R_{n,l}(r) + \left[V(r) + \frac{l(l+1)\hbar^2}{2mr^2}\right]R_{n,l}(r) = ER_{n,l}(r) \qquad \text{Equation 5.5}$$

We know that the coulomb potential provided by the atomic nucleus has a negative sign, and it is related to the distance of the electron. Close to the nucleus, it has the full Coulomb potential:

$$V(r) = -\frac{Ze^2}{4\pi\epsilon_0 r} \qquad \text{Equation 5.6}$$

While in the outmost shell, due to other electrons' screening, it only remains one effective positive core electron, therefore:

$$V(r) = -\frac{e^2}{4\pi\epsilon_0 r} \qquad \text{Equation 5.7}$$

The Coulomb potential has a complex form in the intermediate region, but it always pulls back the electron. On the contrary, as l is equal to or greater than zero (for s orbit, $l = 0$; for p orbit, $l = 1$; for d orbit, $l = 2$; and f orbit, $l = 3$), the angular moment related potential has the positive sign, which pushes the electron away from the nucleus. And the force increases with the angular quantum number increasing.

As discussed in the previous exchange coupling chapter, the relative position of two electrons plays a key role in magnetism. And due to this competitive mechanism, the perfect balance of localization and itinerant gives 3d and 4f electrons special magnetic properties, and their electron-electron interaction is much higher than other orbit's electrons. As we mentioned in

Chapter 2.3, the energy induced by the electron's exchange coupling for Co, Fe and Ni is about 1~2 eV. While the Coulomb interaction between nuclear and electron is about 5 eV. Therefore, the electron-electron interaction for 3d electrons is nonnegligible. Unfortunately, the electron-electron interaction is the weak part of DFT calculation. And the exchange-correlation used by the DFT to calculate electron-electron repulsion is developed on the basis of the single-particle approximation, which approximately treats two spin-paired electrons as a single particle. But as we discussed before, electrons in 3d and 4f orbits are spin polarized when the exchange-coupling has the negative sign. When we deal with d and f electrons, the electron pair must be separated into two particles with spin up and spin down, called open-shell calculation. Moreover, the spin-polarized d and f electrons has a spin-spin repulsion with inner electrons. Again, the interchange-correlation of DFT calculation does not take this effect into consideration. As a result, the calculated orbits are too close to each other, and counts insulators as metals.

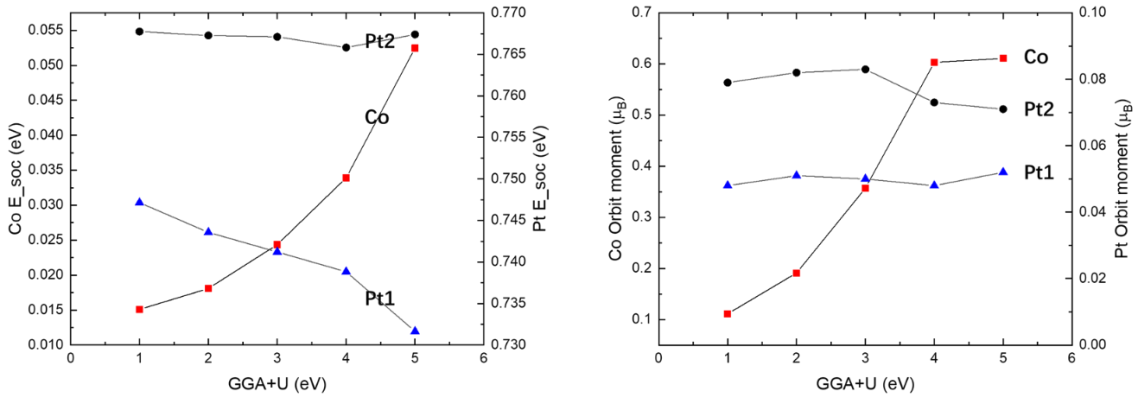

Figure 5.6 The Co and Pt atom's (a) spin-orbit energy and (b) orbit moment as a function of Hubbard U correction. Here the label Pt1 indicates the Co's nearest Pt layer, and the label Pt2 indicates the Co's second nearest Pt layer. Here the left y-axis is for Co and the right y-axis is for Pt.

To solve this problem, the Hubbard U correction was proposed [164], which is derived from the local-density band theory, that provides an excellent agreement with correlated electron quantum chemistry calculations [165]. The 3d electron's localized and delocalized behavior plays an important role on the spin-orbit coupling, while the localization and delocalization are determined by the Hubbard U correction. In this section, Co's Hubbard U correction varies from 1 to 5 eV, while this parameter for Pt is unchanged. And Fig 5.6 shows the Co and Pt's

spin-orbit energy and orbit moment as a function of the Hubbard U correction. It is obvious that the Pt layer enhances the helicity effect, which is also confirmed by both theoretical calculation and experimental measurements [25, 166]. From the first-principal study, we know that the Pt atom's spin-orbit coupling (E_soc = 0.78 eV) is nearly two orders of magnitude greater than the Co atom's spin-orbit coupling (E_soc = 0. 012 eV). As we discussed the IFE in chapter 2.5.3, spin-orbit coupling plays a key role in the Raman scatter IFE model. During the spin flipping process, the angular momentum of the electron system was mainly transferred to the lattice, mediated by the spin-orbit coupling. According to the calculation results, the Pt atom strengthens its nearest Co atom's spin-orbit coupling. The interface Co's spin-orbit energy is about 30% higher than the inner Co atoms. The tendency is evidence that with Co's 3d electrons' localization increases, its spin-orbit energy and orbit moment increase, while its nearest Pt atom's spin-orbit energy. The orbit moment of Pt's 5d electron is much smaller than Co's 3d electron, and it is nearly unchanged with the Hubbard U correction. The second nearest Pt layer's spin-orbit energy and orbit moment have no change, indicating that the Pt enhancing the Co's spin-orbit coupling is a short-range effect that only affects the interface atoms. Compared to the experimental result, the thicker Pt layer provides a higher switching ratio. Therefore, we suggest that although the Co-Pt interface effect could increase the Co's spin-orbit coupling, it does not increase the helicity effect in the Co layer. But the Pt layer itself increases the optical spin-transfer torque. Moreover, the inner Co's spin-orbit coupling is not strengthened, but as we see from Fig 5.4 (b), a thicker Co layer does not decrease the switching ratio. This conclusion is consistent with the previous magnetic dynamic study [167], as they found the IFE was approximately the same in Fe, Ni and Co, but adding a Pt layer could enhance the IFE.

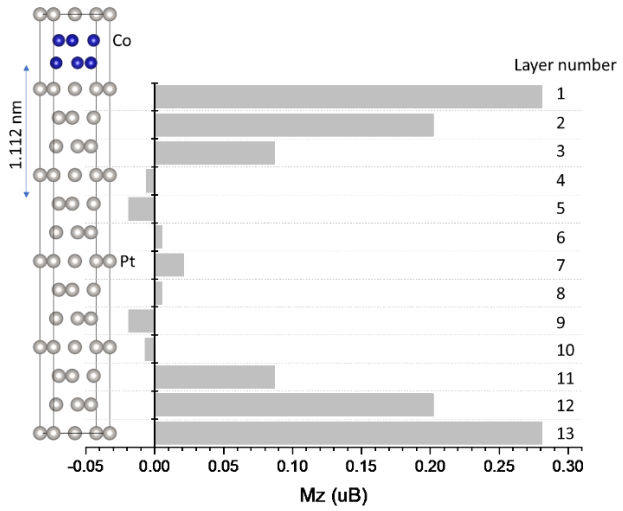

Figure 5.7 The magnetic distribution of Pt layers. Since the periodic boundary condition is used, the magnetic distribution shows symmetry in the c-axis. RKKY induced antiferromagnetic coupling is shown in layer 4, 5 and 9, 10.

RKKY interaction is introduced briefly here. It was first suggested by Ruderman and Kittel in 1954 that a nuclear spin can induce a spin polarization in the surrounding electron sea [87]. The Hamiltonian of this system could be expressed as:

$$H = 2A\delta(r - R)\boldsymbol{S} \cdot \boldsymbol{s} \qquad \text{Equation 5.8}$$

The free electrons as plane waves normalized to a volume V,

$$\psi(r) = \frac{1}{\sqrt{V}} e^{ik \cdot r} \qquad \text{Equation 5.9}$$

The electron kinetic energy by the free electron dispersion relation,

$$E = \frac{\hbar^2 k^2}{2m_e} \qquad \text{Equation 5.10}$$

The total density of states per unit energy is obtained by counting the number of states in the volume V per unit energy and is given by

$$D(E) = \frac{V}{\pi^2 \hbar^2} m_e k = \frac{V}{2\pi^2 \hbar^3} (2m_e)^{3/2} \sqrt{E} \qquad \text{Equation 5.11}$$

If we denote the electron density per unit volume as

$$N_V = \frac{1}{V} \int_0^{E_F} D(E) dE = \frac{(2m_e E_F)^{3/2}}{3\pi^2 \hbar^3} = \frac{k_F^3}{3\pi^2} \qquad \text{Equation 5.12}$$

The RKKY exchange coefficient J(R)

$$J(R) = \frac{16A^2 m_e k_F^4}{(2\pi)^3 \hbar^2}\left[\frac{\cos(2k_F R)}{(2k_F R)^3} - \frac{\sin(2k_F R)}{(2k_F R)^4}\right] \quad \text{Equation 5.13}$$

At large R takes a simple form:

$$J(R) = \frac{2A^2 m_e k_F}{(2\pi)^3 \hbar^2}\frac{\cos(2k_F R)}{R^3} \quad \text{Equation 5.14}$$

As the RKKY coupling is related to the electron's localization and itineration, one could expect the GGA+U parameter will affect the strength of RKKY coupling.

An unexpected discovery in the DFT calculation is that the Co/Pt multilayer system has an RKKY coupling induced interlayer antiferromagnetic coupling. The magnetic moment distribution in the Pt layers is shown in Fig 5.7. Normally, Pt is paramagnetic, but the nearest Pt layers (layer 1 and 13) are magnetized by Co layers which has a magnetic moment of about 0.28 μ_B. The second and third nearest Pt layers' magnetic moment decreases significantly. Then the fourth and fifth layers have a negative magnetic moment. We calculated both the ferromagnetic (FM) and antiferromagnetic (AFM) coupling states in this structure, and the total free energy for FM is higher than the AFM. Hence, the AFM state is more stable in the ground state. However, the AFM coupling is not observed experimentally in most Co/Pt multilayers [168-170]. One of reason that the antiferromagnetic coupling in the Co/Pt multilayer is related to the layer repeat times. As shown in Fig 5.8 (e-f), J. W. Knepper and F.Y. Yang found that the antiferromagnetic coupling is not observed for $\left[Co(4\,\text{Å})/Pt(11\,\text{Å})\right]_N$ with N = 5 and 8 [171]. But when the repeat times increase to 12, the AFM coupling induced subloops were observed. And then, the AFM coupling is significantly enhanced when repeat times increase to 30. In our calculation, the periodic boundary condition gives the structure infinity repeat times, and therefore the calculated RKKY coupling is much larger than the experimental results.

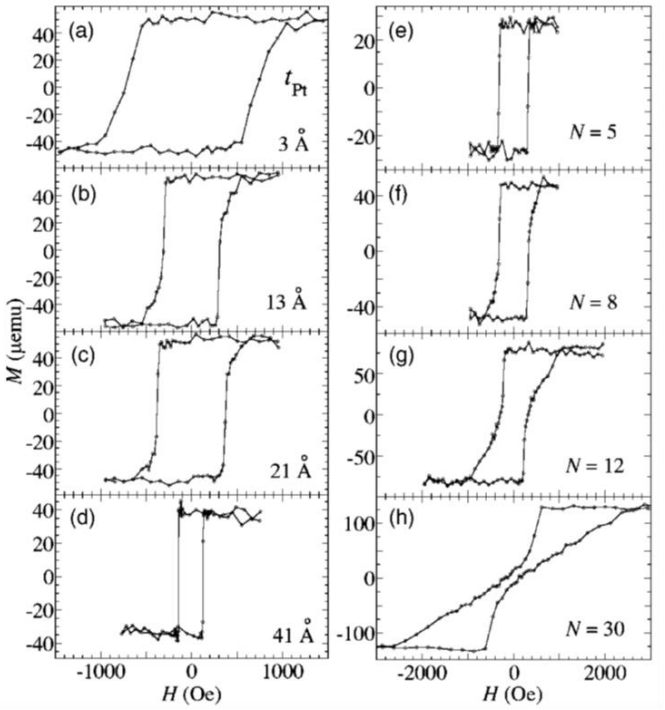

Figure 5.8 (a) to (d) Room temperature hysteresis loops of $[Co(0.4\,nm)/Pt(t_{Pt})]_8$. (e) to (h) Room temperature hysteresis loops of $[Co(0.4\,nm)/Pt(1.1\,nm)]_N$ multilayers *[171]*.

To figure out the relationship between the interlayer antiferromagnetic coupling and the Co/Pt structure's repeat time, a single repeat Pt/Co/Pt sandwich structure with varies Co layers was calculated. This structure has 13 Pt layers on the side of the Co layers. In consideration of the periodic boundary, a vacuum of 50 Å between the structure and the cell constraint at the c-axis are set to eliminate the layer interaction. Fig 5.9 shows the magnetic moment distribution in the Pt layers. It is clear that the antiferromagnetic coupling exists even in the single repeat structure, and more Pt layers have an opposite magnetic direction. However, the situation is slightly different from the previous infinite repeat structure. The distance between the Pt layer with opposite magnetic direction and the Co layer is much longer than in the previous condition. Also, all structures with Co layers from 2 to 6 have the antiferromagnetic coupling. Therefore, we confirmed that the interlayer antiferromagnetic coupling is not related to the Co/Pt structure's repeat time. In 2017, Vomir and *et al.* demonstrated that the magnetization reversal in a Pt/Co/Pt stack can be induced by a single femtosecond laser pulse, which occurs back and forth with subsequent laser pulses and it is helicity-independent [172]. Although they contributed this phenomenon to the size of the switched spot is comparable to the size of the intrinsic magnetic domains, the mechanism is still not clear. As all of the single shot helicity-independent AOS are observed in the ferrimagnetic materials, we suggest that this phenomenon

may be related to the interlayer antiferromagnetic coupling induced by the RKKY effect in the Pt/Co/Pt structure.

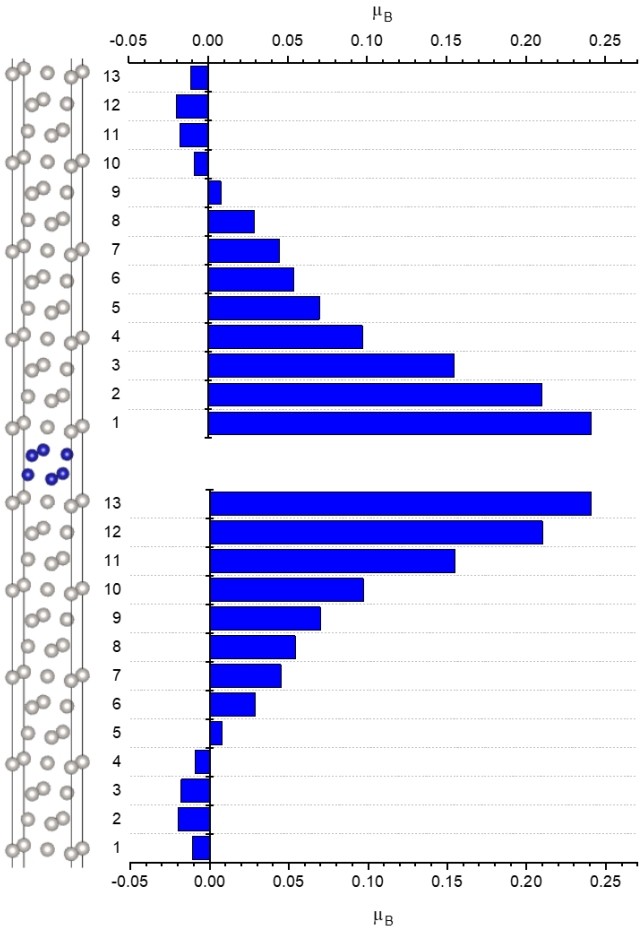

Figure 5.9 Pt/Co/Pt single stack structure and the magnetic distribution in the Pt layers. The magnetic moment of the Co atom is 2.054 μ_B, which is 10 times larger than the Pt.

5.5 Conclusion

In this chapter, two series samples are used to investigate the HD-AOS's power window and switching ratio. All samples were grown by magnetron sputtering system with the same growth condition and the same structure of Glass/Ta/Pt/Co/Pt. HD-AOS is observed for the Co thickness between 0.6 to 1.2 nm and its power window is proportional to both Co's and Pt's thickness. The switching ratio is also related to the Co's and Pt's thickness. The highest switching ratio is observed for the sample with 5 nm Pt layer. The DFT calculation gives a crucial explanation to the experimental results. Moreover, a surprising interlayer antiferromagnetic coupling is found in the Co/Pt multilayer system, which is due to the RKKY coupling. The strength of RKKY coupling is found to be related to the Co's 3d electrons' localization and itineration, which is described by the Hubbard U correction.

Chapter 6 Ultrafast laser-induced spin dynamics in synthetic antiferromagnetic materials

6.1 Introduction

The development of big data, cloud computing, and artificial intelligence require a new memory with high speed, non-volatility, higher density, and lower power consumption [173, 174]. Antiferromagnetic materials have become an important development direction of ultra-fast and ultra-high density information storage due to their advantages of no stray field, high intrinsic frequency and good anti-interference ability to the external magnetic field, and are expected to be applied in high-frequency electronic devices to prevent electromagnetic threats [175]. Since antiferromagnetic materials have zero net magnetic moment and they are insensitive to external magnetic field, how to control and detect the antiferromagnetic moment has become the forefront and research hotspot in the field of spintronics [75, 176]. The discovery of oscillatory interlayer exchange coupling between two ferromagnetic (FM) layers separated by a nonmagnetic (NM) spacer spurred great promotion in the antiferromagnetic (AFM) spintronics applications such as the giant magnetoresistance (GMR) sensor and magnetic random-access memories. Compared with normal AFM materials, SAF systems give more flexibility. By changing the thickness of the NM layer, one could easily tune the strength of the AFM coupling [173, 177]. While the magnetic properties like magnetic anisotropy, coercivity or magnetic moment of each FM layer could be tuned individually, by changing the FM layer's thickness or material. In recent years, synthetic antiferromagnetic (SAF) systems with perpendicular magnetic anisotropy (PMA) have attracted researchers' attention. AFM coupled materials have advantages in the application of spintronics compared with traditional ferromagnetic (FM) materials. Due to the antiparallel aligned magnetic moments, it has high magnetic field stability, negligible stray fields and fast operation speed at THz [79, 178]. Recently study found that this antiferromagnetic interaction can be tuned electrically [90, 179]. By adding a circuit gating voltage, AFM coupling is enhanced or converted into an AFM-FM intermediate state, which paves the way for its potential application in spintronics. Also, the theory describes in-plane current-driven domain wall motions in SAF was developed [180]. Moreover, it was found that the SAF system could lead to double terahertz emission peak amplitude [181].

Spintronics concerns all interactions of the spin system, like the Zeeman effect, spin-orbit torque or RKKY interaction. Researching those interactions provides various ways to

manipulate and detect the spin direction and, therefore, use it to manipulate and store information. Recently, manipulating interlayer exchange coupling (IEC) has drawn much attention. Many new methods were demonstrated, such as accumulating surface charge [182], realizing tri-phase transition by modulating oxygen vacancies in oxide thin films [74] and regulating magnetic properties by changing the electron density at the Fermi level [73, 183]. In this chapter, we will present, for the first time, the ultrafast laser pulse induced IEC dynamics in the SAF system. This method shows many superiorities over previous methods, such as room temperature operation, high energy efficiency and ultrafast manipulating speed. A laser pulse with a central wavelength of 800 nm and pulse width of 50 fs is used to excite the SAF system, and another 400 nm laser pulse is used to probe the transient magnetic properties of the SAF system. All measurements were done at room temperature. Time-resolved MOKE spectroscopy is usually used for investigating the magnetic dynamic properties in the time domain, which contains the ultrafast laser-induced ultrafast demagnetization. This process takes place within 1 ps for Fe, Co, Ni's 3d electrons[136, 184-186]. Then if the applied magnetic field is not in the easy axis, there will be a subsequent precession process due to the changing of the magnetic anisotropy. This process's duration varies from ten to hundreds of picoseconds depending on materials' magnetic damping factor [187-189]. Here, three series of AFM samples with three different interlayers are investigated. SAF samples based on the Co/Pt structures as that in the previous chapters were grown by magnetron sputtering. Antiferromagnetic IEC with PMA is observed in all spacers, including MgO, Ru and NiO, which is confirmed by VSM measurements. The sample structure is shown in Fig 6.1. Also, the relationship between IEC strength and spacer's thickness is investigated. The transient hysteresis loop induced by laser pulse shows that the AFM coupling in SAF with MgO spacer can be temporarily suppressed by laser. Time-resolved MOKE results further prove that this AFM coupling is temporary suppressed by laser in SAF with NiO or Ru spacer. Moreover, these results provide an AFM coupling dynamic changes in an ultrafast timescale.

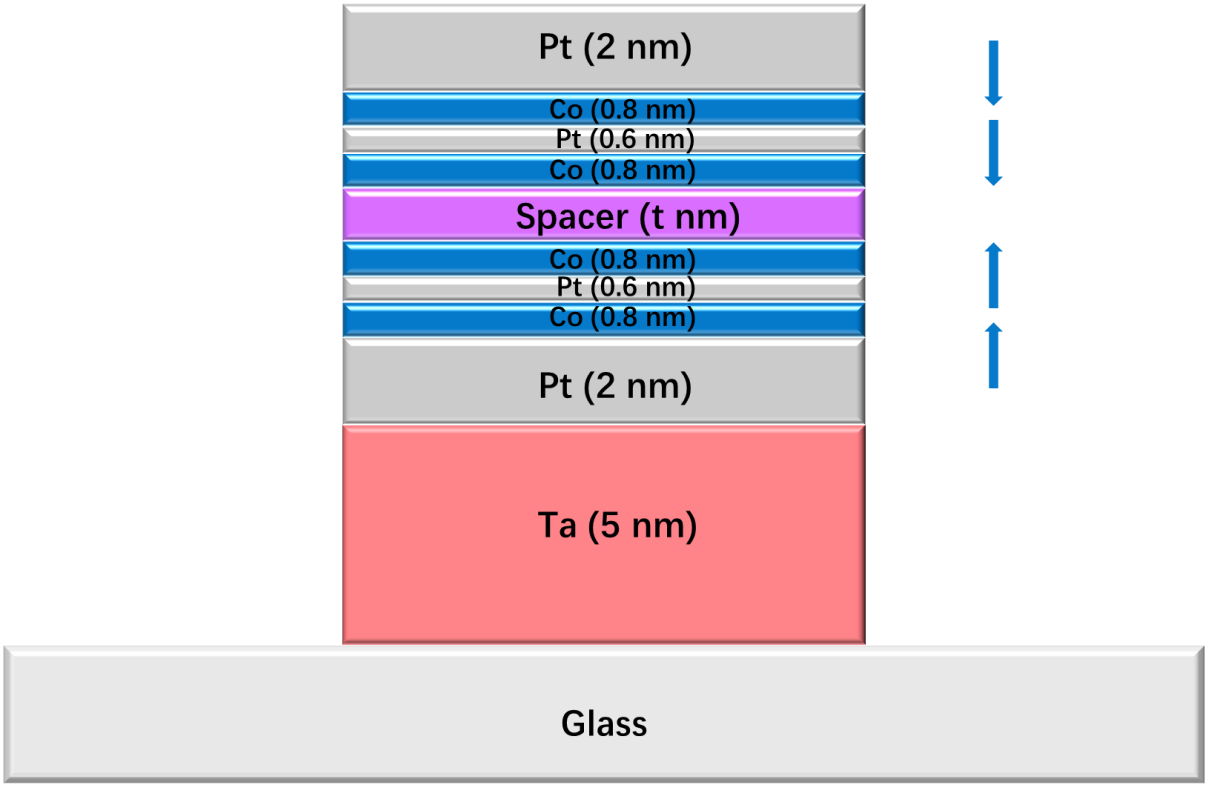

Figure 6.1 Schematic of Co/Pt SAF sample's structure with PMA.

6.2 Sample details

All of them have the same layers' structure: Glass/Ta (5 nm)/Pt (2 nm)/Co/ (0.8 nm)/Pt (0.6 nm)/Co (0.8 nm)/Spacer (t nm)/Co (0.8 nm)/Pt (0.6 nm)/Co (0.8 nm)/Pt (2 nm). These samples were deposited on Corning glass with a thickness of 0.13 nm at room temperature by DC and RF magnetron sputtering from separate Co, Pt, Ta, MgO, NiO and Ru targets. The base pressure of the sputtering system was better than $4 \times 10^{-5}\ Pa$, and the working Ar pressure was $0.5\ Pa$. The sputtering rate with a DC current of 40 mA was 0.41, 0.84, and 0.48 $Å/s$ for Ta, Pt, and Co, respectively. The first 5 nm Ta buffer layer was employed to improve the smoothness of the substrate, the Pt/Co interface smoothness and the (111) orientation, and thereby enhance the perpendicular magnetic anisotropy (PMA) of the Co layer. The Co layers between the spacer provide the important interlayer exchange coupling, while repeated Co/Pt layers provide PMA of the system. The top 2 nm Pt layer protects the sample from oxidation. There are three different spacer layers, Ru, MgO and NiO, with a sputtering rate of 0.52, 0.1 and 0.19 $Å/s$, respectively.

For those three types of SAF systems, the strength of IEC is determined by the following equation:

$$J_{IEC} = H_{ex} M_S t_{Co} \qquad \text{Equation 6.1}$$

where M_S is the saturation magnetization of two Co layers between spacer, t_{Co} is the thickness of Co layers between spacer, and H_{ex} is the shift step length in the two steps hysteresis loop. Here we determined the sign of the J_{IEC} to the type of the coupling: for ferromagnetic coupling $J_{IEC} < 0$ and for antiferromagnetic coupling $J_{IEC} > 0$. Fig 6.1-6.3 shows the hysteresis loops of all samples, measured by VSM. The difference in the IEC mechanism provides varied properties of the SAF system. For example, the IEC strength for insulating spacers increases with the increase of the temperature in contrast to the case for metallic spacers [190]. Since M_S and t_{Co} are the same for all samples, the strength of IEC could be directly compared by the H_{ex}, as shown in table 6.1.

Table 6.1 Three different spacers' hysteresis loop shift H_S as a function of thickness.

Ru(nm)	0.4	0.6	0.8	0.9	1.0	1.1	1.2
$\boldsymbol{H_{ex}}$ (Oe)	9000	3800	2700	3900	3300	3100	**FM**
MgO(nm)	0.8	1.0	1.2	1.4	1.6	1.8	2.0
$\boldsymbol{H_{ex}}$ (Oe)	**FM**	**FM**	**FM**	240	230	**FM**	250
NiO(nm)	0.9	1.0	1.1	1.2	1.3	1.4	1.5
$\boldsymbol{H_{ex}}$ (Oe)	360	800	**FM**	686	200	300	**FM**

The first one is the well-explored metallic spacer, Ruthenium. This type shows a magnetic oscillation coupling, which origins from the spin-dependent reflectivity of conduction electrons at the FM/NM interface, as explained by the Ruderman-Kittel-Kasuya-Yosida (RKKY) theory [87, 88, 191, 192]. The IEC induced by metallic spacers has been subsequently studied in both theory and experiment [171, 173, 177, 193]. As early as 1989, Slonczewski first proposed the IEC theory for the non-metallic spacer, and he calculated the charge and spin-current through a rectangular barrier in FM/insulator/FM structure and got the IEC strength J_{IEC}. Several years later, in 1994, Bruno unified the metallic and insulating spacer by the terms of quantum interferences due to confinement in ultrathin layers and also introduced the concept of the complex Fermi surface to explain the origin of IEC [194, 195]. But for an antiferromagnetic

spacer NiO, the IEC comes from the antiferromagnetic nature of the spacer as suggested by Liu and Adenwalla [84].

The IEC strength has an oscillatory decay with the increase of the spacer thickness for the metallic spacers such as Ru, but a nonmonotonic oscillatory coupling and nonoscillatory decay of IEC strength for the insulating spacer is observed, which is consistent with previous reports [196, 197]. The strongest AFM coupling observed with a Ru thickness of 0.4 nm corresponds to the first oscillation IEC peak [198]. It should be noted that the AFM coupling field observed with a Ru thickness of 0.4 nm is normally less than 3 kOe [199]. This is attributed to the roughness and intermixing at the interfaces of the spacer layer. If a uniform spacer layer can be formed under 0.5 nm, stronger AFM coupling can be achieved at the RKKY's first peak. Also, there is a minor loop in some samples with Ru spacer, and their M_s and H_c are different from each other. This is also attributed to the roughness of the Ru layers, and an annealing process may avoid this effect. The IEC is much weaker for MgO spacer, and AFM coupling is observed until the thickness is up to 1.4 nm.

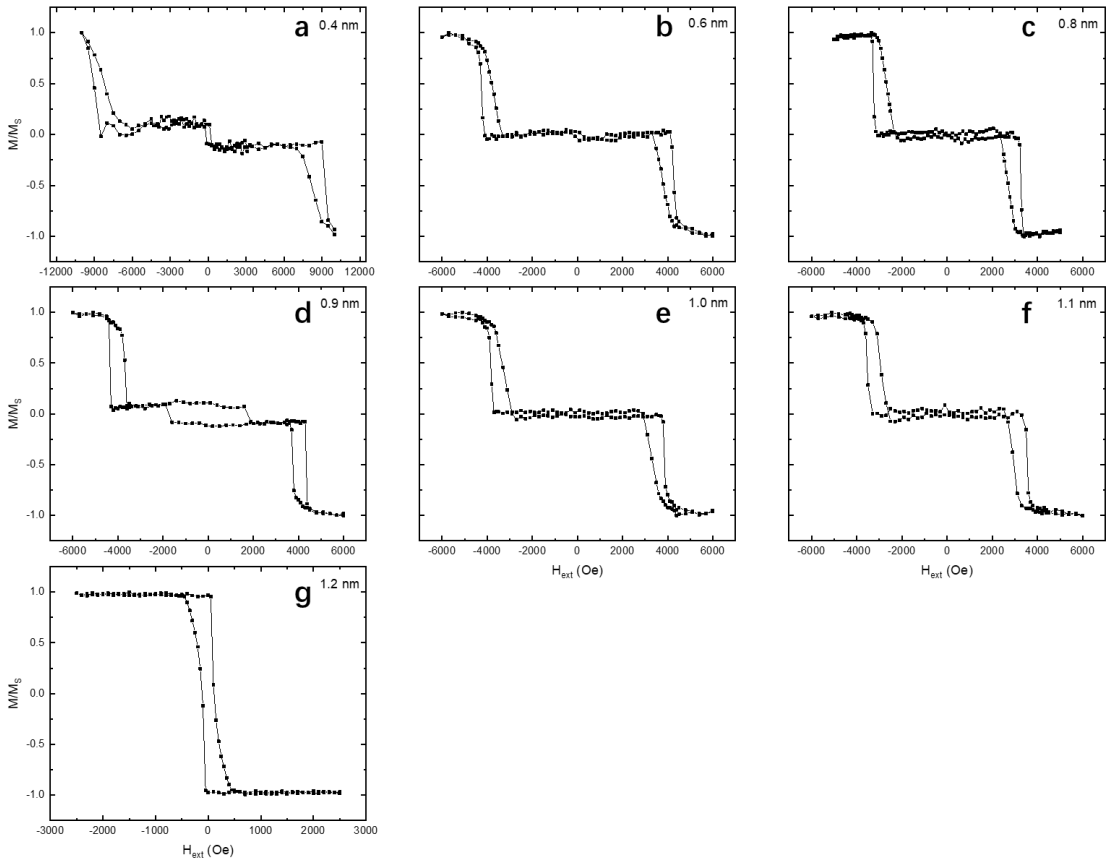

Figure 6.2 Magnetic hysteresis loop for Glass/Ta (5 nm)/Pt (2 nm)/Co (0.8 nm)/Pt (0.6 nm)/Co (0.8 nm)/**Ru** (t nm)/Co (0.8 nm)/Pt (0.6 nm)/Co (0.8 nm)/Pt (2 nm) measured by VSM.

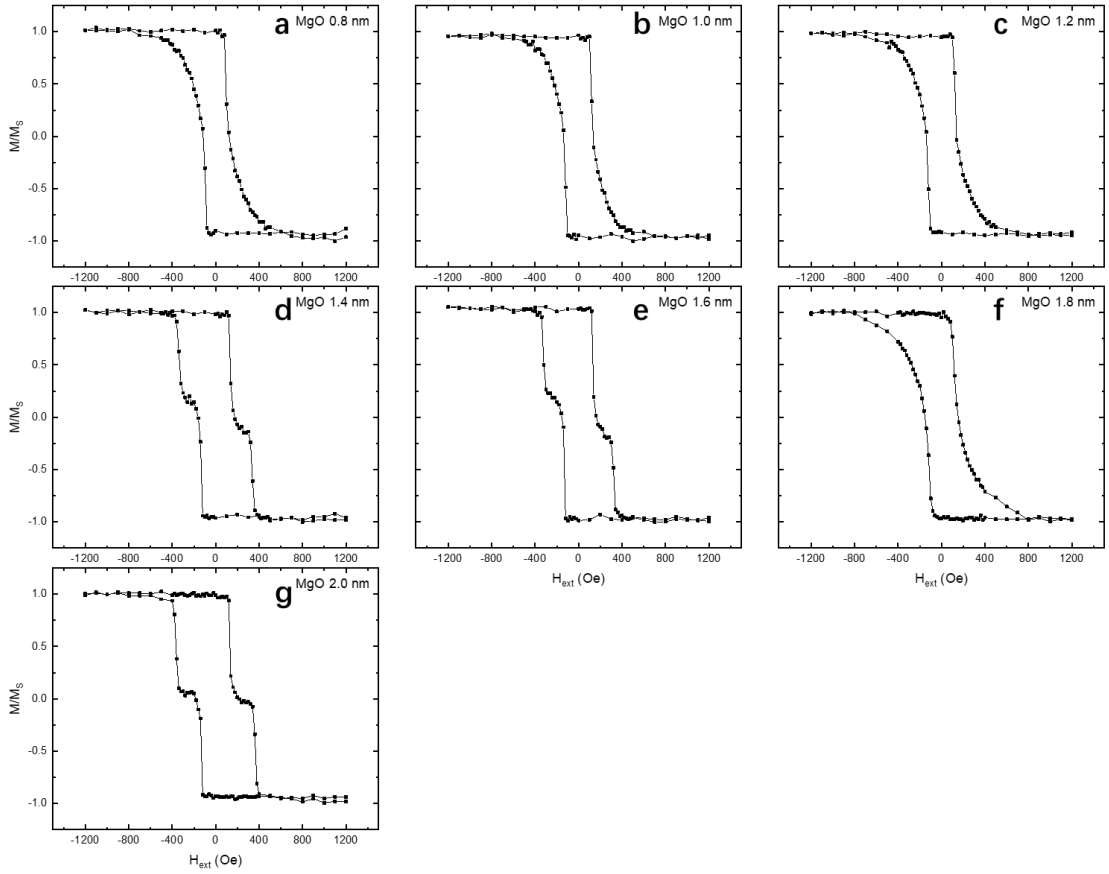

Figure 6.3 Magnetic hysteresis loop for Glass/Ta (5 nm)/Pt (2 nm)/Co (0.8 nm)/Pt (0.6 nm)/Co (0.8 nm)/**MgO** (t nm)/Co (0.8 nm)/Pt (0.6 nm)/Co (0.8 nm)/Pt (2 nm) measured by VSM.

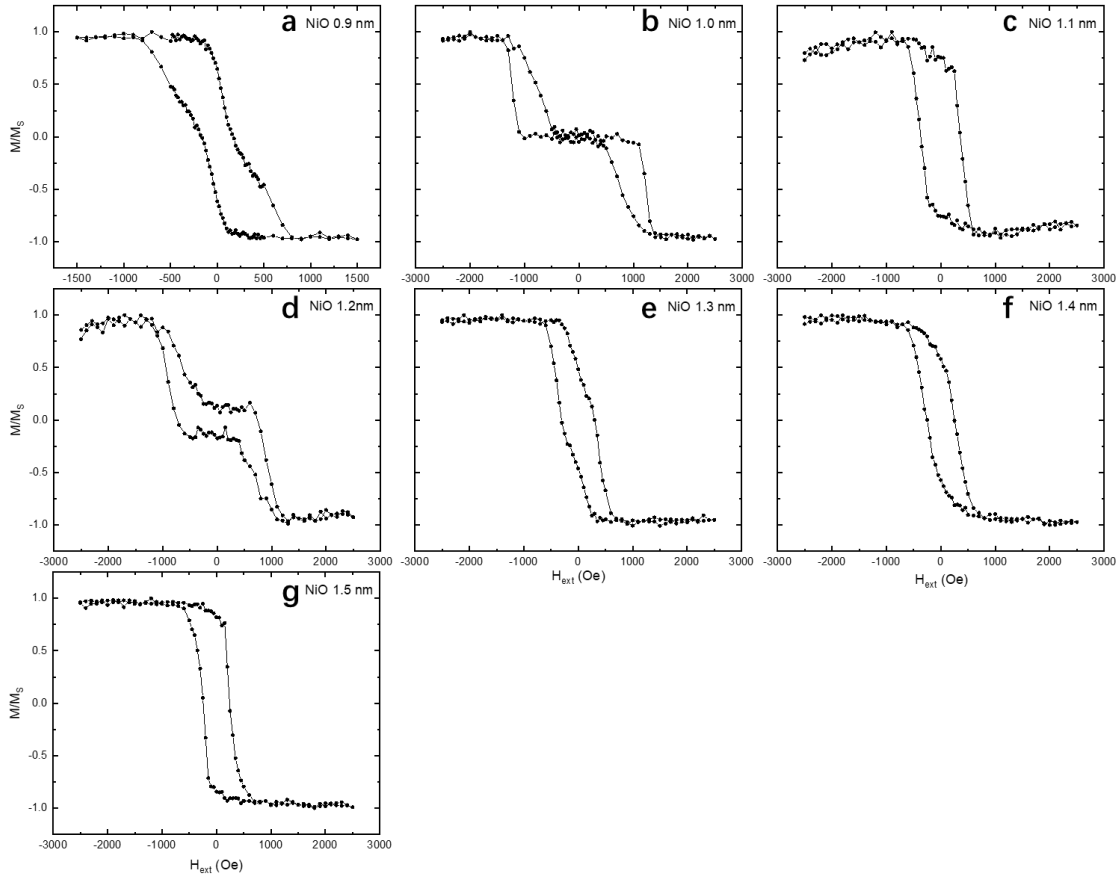

Figure 6.4 Magnetic hysteresis loop for Glass/Ta (5 nm)/Pt (2 nm)/Co (0.8 nm)/Pt (0.6 nm)/Co (0.8 nm)/**NiO** (t nm)/Co (0.8 nm)/Pt (0.6 nm)/Co (0.8 nm)/Pt (2 nm) measured by VSM.

6.3 Time-resolved MOKE experimental details

The experimental configuration used to perform the time-resolved MOKE measurements was described in Chapter 3.2. As all the samples have perpendicular magnetic anisotropy, the experimental setup was adjusted to make it sensitive to the out of plane magnetic direction as shown in Fig 6.5. To improve the time resolution, 50 fs pulses were used, coming from a Ti:Sappire amplified at 1 kHz with a central wavelength of 800 nm. The pump beam's wavelength is 800 nm, while the probe beam goes through a barium boron oxide (BBO) crystal, and therefore, its wavelength is 400 nm. Both were focused onto the sample with respective spot diameters of $\sim 400\ \mu m$ for the pump beam and $\sim 200\ \mu m$ for the probe. The intensity of the probe beam is fixed at $30\ \mu W$, while the pump beam's intensity varies from $1\ mW$ to $12\ mW$. The polarization of the pump beam is s, whereas the polarization of the probe beam is p. After being reflected by the sample, the probe beam is divided into s and p components

by the Wollaston crystal. By tuning the fast-axis of the half-wave plate before the Wollaston crystal, the signal of the bright detector is zero without the pump pulse's excitation. This kind of detection significantly improves the signal-noise ratio.

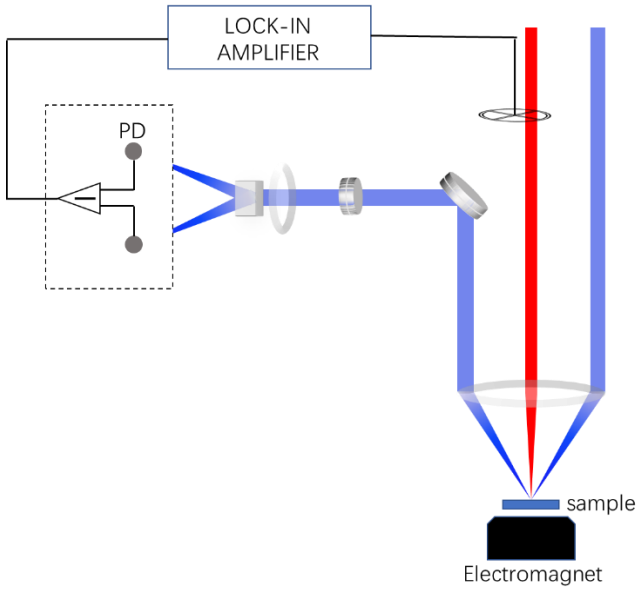

Figure 6.5 Schematic geometry of pump-probe TR-MOKE measurements.

6.4 Ultrafast laser-induced magnetization dynamics in SAF

Firstly, the laser pulsed induced ultrafast demagnetization was measured in the SAF sample. The MOKE signal has been measured continuously as a function of the pump-probe delay. Samples used in this section include $[Pt/Co]_2$/Ru (0.8 nm)/$[Co/Pt]_2$, $[Pt/Co]_2$/NiO (1.0 nm)/$[Co/Pt]_2$, and $[Pt/Co]_2$/MgO (2.0 nm)/$[Co/Pt]_2$, and all have an interlayer antiferromagnetic coupling confirmed by the VSM measurements. All TR-MOKE results were measured twice with opposite magnetic field directions, and then the subtraction of them could eliminate the nonmagnetic noise. This method was widely discussed by Koopmans and Bigot [200, 201], as they demonstrated that the true demagnetization takes approximately 0.5-1 ps after the pump pulse. The subtraction curve of demagnetization in the positive and negative magnetic fields is shown in Fig 6.6. Compared with ultrafast demagnetization in ferromagnetic materials, no significant differences were observed at a high magnetic field, as seen in Fig 6.6 (a). The pump pulse fluence is 12 mW, and the bottom curve was measured in an out of plane magnetic field of 3500 Oe. In such a high magnetic field, all spins are aligned to the field direction since this sample's H_{ex} is 2700 Oe. The ultrafast laser first induces an ultrafast demagnetization followed by a fast remagnetisation process. And the same dynamic properties were observed in other samples with different thicknesses and types of spacers. Since the

applied magnetic field easily aligns all spins in the same direction, that makes the system the same as the ferromagnetic system. And hence, there is no interatomic transfer of angular momentum within the spin system.

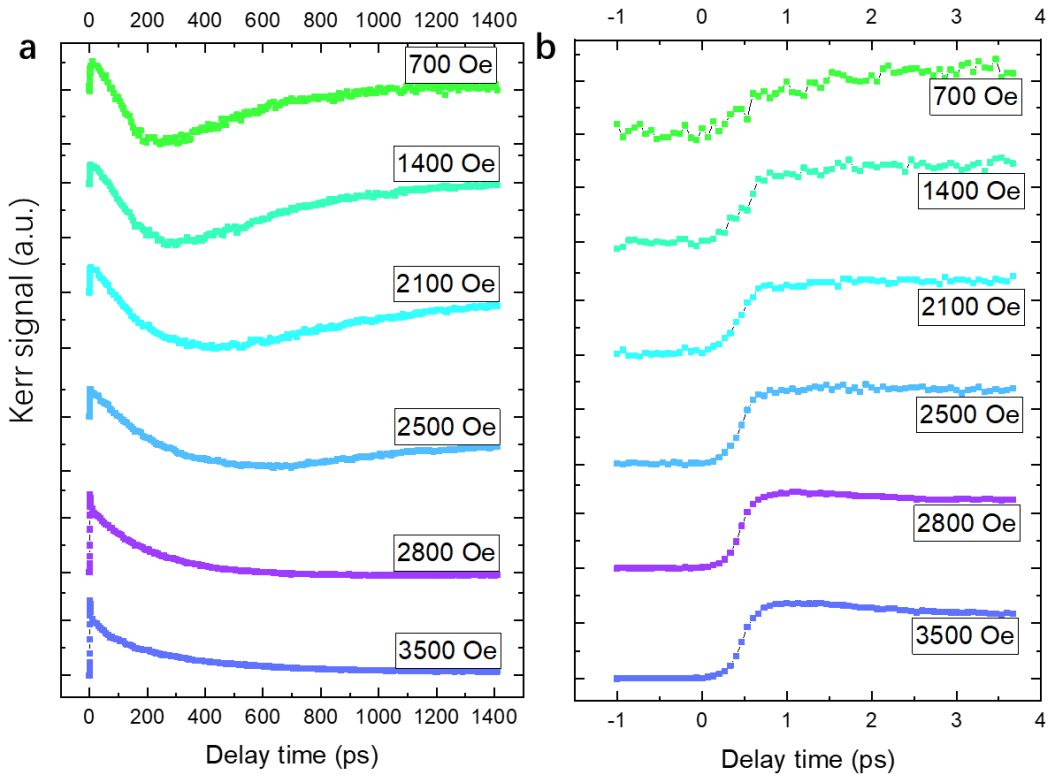

Figure 6.6 Normalized dynamic MOKE signals for $[Pt/Co]_2$/Ru (0.8 nm)/$[Co/Pt]_2$ measured at different applied fields with a pump fluence of 12 mW. (a) shows the whole dynamic process up to 1.4 ns. (b) shows the first 3.5 ps demagnetization process.

When the applied field is smaller than the sample's H_{ex}, the situation becomes much different, as shown in Fig 6.6. Although the penetration depth of the 400 and 800 nm laser is longer than our samples' thickness and the measured MOKE signal comes from all layers, the different Kerr sensitivities of each layer provide a non-zero MOKE signal, and the top Co-Pt multilayer contributes about 60% of the total Kerr signal seen from the MOKE signal in zero magnetic field. Hence, a demagnetization process is observed even at an antiferromagnetic state. A dramatic point in Fig 6.6 (a) is the reverse of the Kerr signal ($\Delta\theta_K$) at the antiferromagnetic state, which indicates that after the demagnetization the laser could induce a magnetization increasing when the sample is at antiferromagnetic state. Also, if one compares the 2500 Oe result with the 2800 Oe result, it is obviously that this ultrafast magnetization increasing

process speeds up the remagnetization process. This magnetization increase has a recovery process as well, and its relaxation time is related to the applied field as well. The relaxation time is much shorter for 700 Oe than 2500 Oe. Moreover, the applied field also affects the demagnetization time while longer demagnetization time is observed at smaller field seen in Fig 6.6 (b). But this effect is not suitable for ferromagnetic state, as the demagnetization and remagnetization time is nearly the same for 2800 Oe and 3500 Oe.

The reverse of $\Delta\theta_K$ is not only related to the applied field but also the pump fluence, as shown in Fig 6.6 and Fig 6.7, respectively. The reverse of $\Delta\theta_K$ is faster with the decrease of the applied field and the increase of the pump fluence. This phenomenon also appears in the sample with 1.0 nm NiO spacer as shown in Fig 6.8. But the pump fluence threshold value is different for Ru and NiO. In Ru case, the reverse of $\Delta\theta_K$ is not observed when the pump fluence goes down to 7 mW. While in NiO case, the pump fluence needed to reverse $\Delta\theta_K$ is only 2.5 mW. The pump fluence threshold value will be discussed in detail in the next section. However, the reverse of $\Delta\theta_K$ is not observed in the sample with MgO spacer.

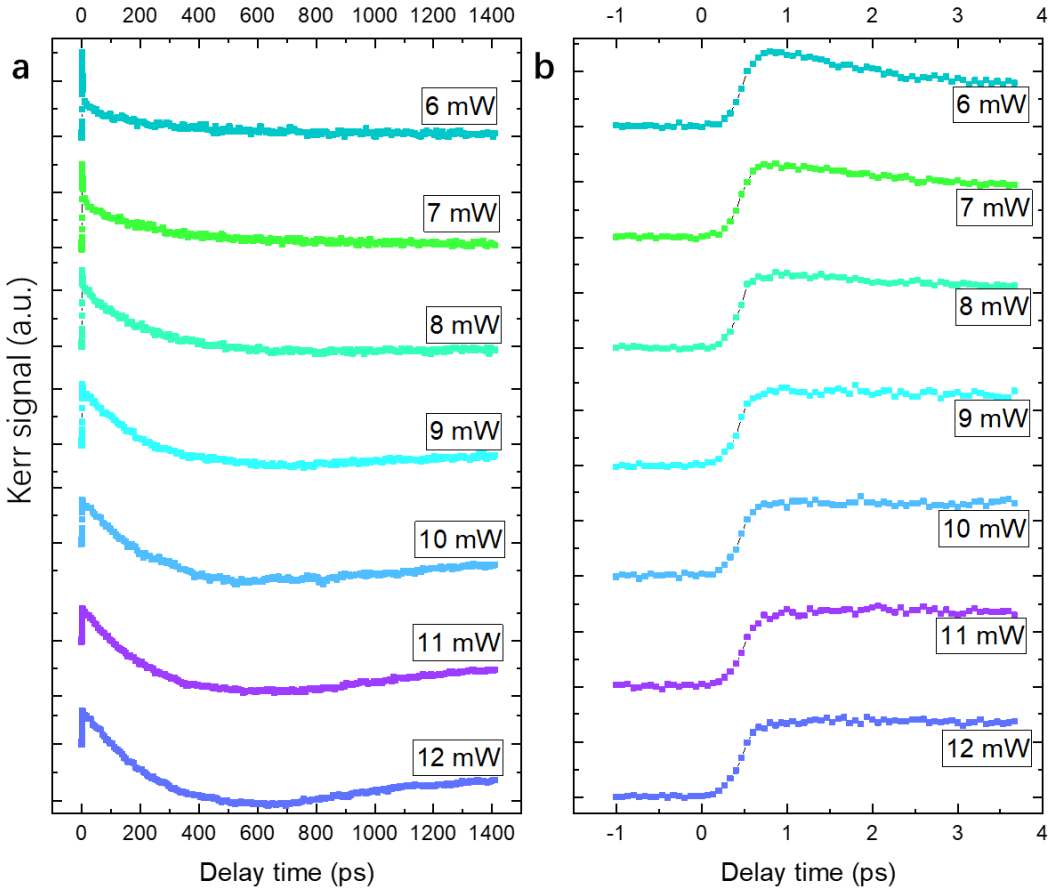

Figure 6.7 Normalized dynamic MOKE signals for $[Pt/Co]_2/Ru$ (0.8 nm)/$[Co/Pt]_2$ measured at different pump fluence with an applied field of 2500 Oe. (a) shows the whole dynamic process up to 1.4 ns. (b) shows the first 3.5 ps demagnetization process.

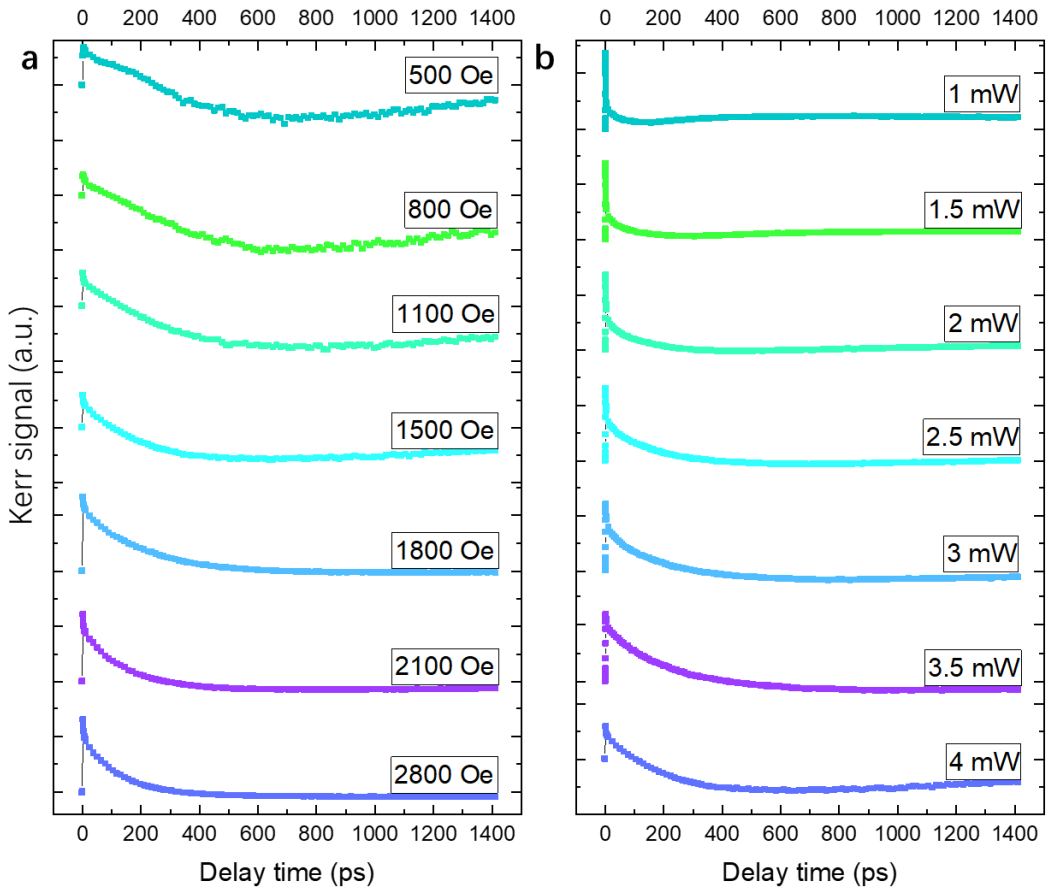

Figure 6.8 Normalized dynamic MOKE signals for $[Pt/Co]_2/NiO$ (1.0 nm)/$[Co/Pt]_2$ measured at: (a) different applied field with a pump fluence of 4 mW and (b) different pump fluence with an applied field of 1500 Oe.

The transient hysteresis loop induced by the pump pulse provides the direct IEC information of the system. The full transient hysteresis loop was measured at a fixed delay time by sweeping the magnetic field and recording the MOKE signal. As early as 1998, this method was used to show the magnetic phase transition in $CoPt_3$ [163]. Ultrafast spin precession was also used to study the antiferromagnetic interaction dynamics [202]. When all spins in SAF are aligned to the same direction by the applied magnetic field, the spin precession shows an acoustic mode. With the applied magnetic field decreasing to lower than the IEC, the opposite direction spins at the top and bottom layers have an optical precession mode. However, this method could not give the IEC strength changing at different power, and the IEC strength was totally controlled by the applied magnetic field.

For each sample, the transient hysteresis loop is modified by varying the pump fluence at a fixed delay time of 1 ps. It can be seen that the transient hysteresis loop is significantly different for the three different samples. Fig 6.9 shows 0.8 nm Ru spacer results. After being excited by

a lower fluence laser pump, the original double hysteresis loop changes to a triple-state pattern. The triple-state pattern comes from the different absorption of the top and bottom Co/Pt layers. As the top one absorbs more laser energy than the bottom one, $\Delta\theta_k^t$ is larger than $\Delta\theta_k^b$. Hence, the change of the net Kerr signal is not zero. Even the top and the bottom layer is antiparallel. With the laser pump increasing, both Co/Pt layers reach their absorption limitation, and this phenomenon vanishes. With the pump fluence up to 8 mW, the transient loop shows a 4 stage behaviour, which has never been reported before. Also, compared with the original hysteresis loop, the strength of the interlayer antiferromagnetic coupling of $\Delta\theta_k$ is not changed for all pump fluence. In general, the interlayer antiferromagnetic coupling is not suppressed for the Ru spacer at this delay time. The situation for MgO spacer is very different. The interlayer antiferromagnetic coupling and PMA are both suppressed when the pump power is increased to 6 mW. While for the NiO spacer, the original double-loop pattern is converted to a triple-loop pattern when the pump power is increased to 4 mW pump power. And with the pump power increasing, the triple-loop pattern becomes more obvious. This effect also relates to the time delay, which will be discussed later.

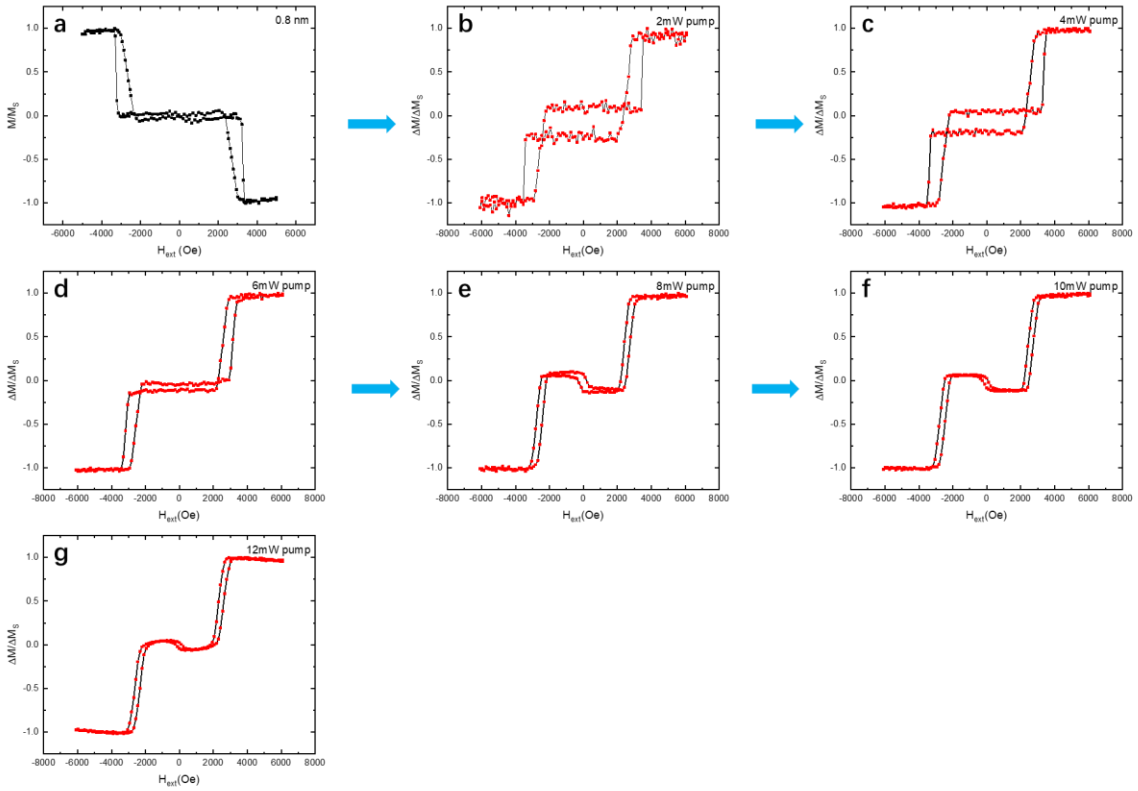

Figure 6.9 Transient magnetic polar Kerr loops of the $[Pt/Co]_2$/Ru (0.8 nm)/$[Co/Pt]_2$ thin film excited by 6 different pump fluence at the same delay of 1 ps.

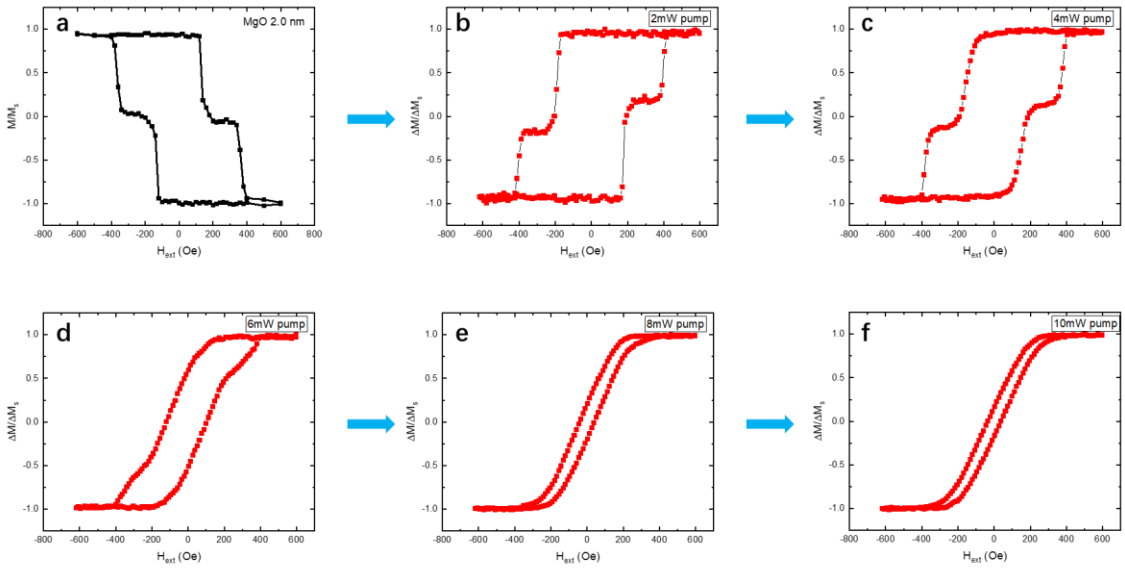

Figure 6.10 Transient magnetic polar Kerr loops of the $[Pt/Co]_2/MgO$ (2.0 nm)/$[Co/Pt]_2$ thin film excited by 5 different pump fluence at the same delay of 1 ps.

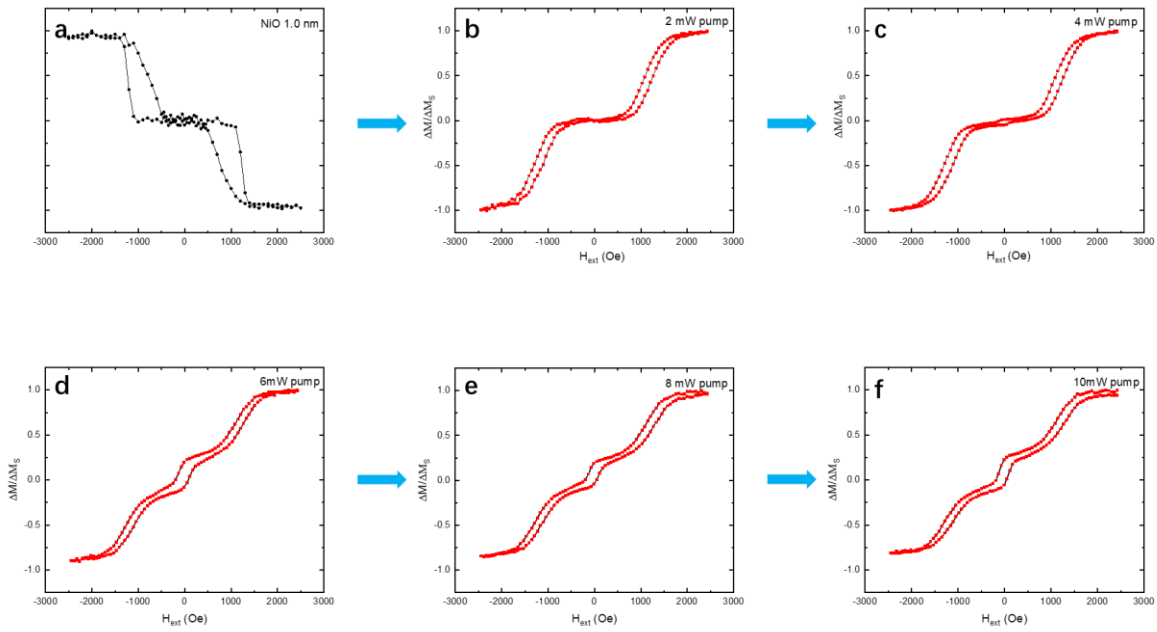

Figure 6.11 Transient magnetic polar Kerr loops of the $[Pt/Co]_2/NiO$ (1.0 nm)/$[Co/Pt]_2$ thin film excited by 6 different pump fluence at the same delay of 1 ps.

As shown in Fig 6.12, there are 9 delay time points chosen to discuss the IEC's dynamic process. The first 4 delay points present the ultrafast demagnetization process, while the following 5 delay points present the magnetic relaxation process. When measuring the transient hysteresis loop, the lock-in system's input reference frequency is the optical chopper frequency in the pump beam. Therefore, the MOKE signal measured is not the Kerr signal of the whole magnetic moment θ_K, but the pump-pulse induced magnetic moment variation $\Delta\theta_K$.

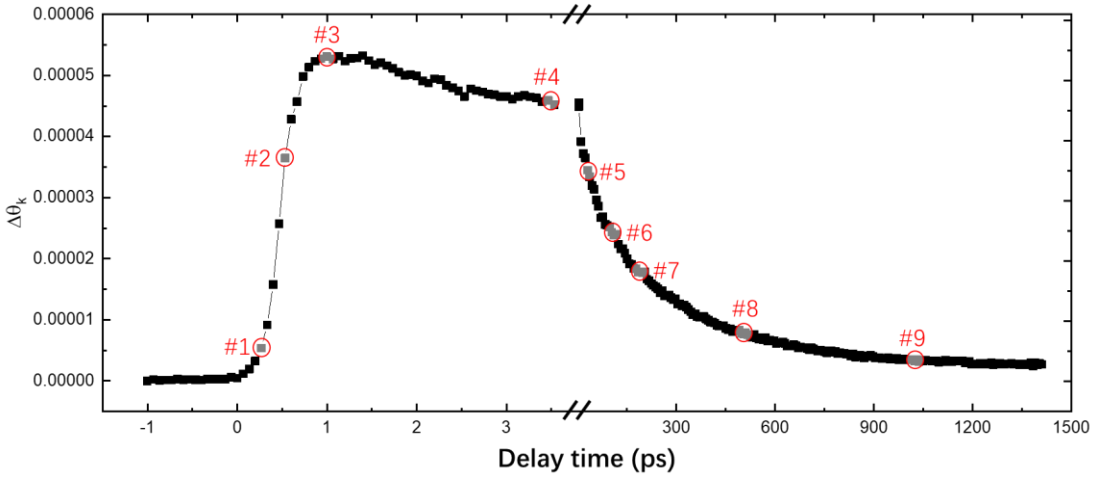

Figure 6.12 Magnetic dynamic MOKE signal for the $[Pt/Co]_2$/Ru (0.8 nm)/$[Co/Pt]_2$ pumped by a laser fluence of 12 mW. The numbered cycles in the curve indicate the delay time when the transient hysteresis loop was measured.

Fig 6.13 shows these 9 transient loops in Pt/Co/Pt/Co/Ru (0.8 nm)/Co/Pt/Co/Pt thin film with a pump fluence of 12 mW. The number in each figure's right-bottom corner shows the delay time. It is obvious that the interlayer antiferromagnetic coupling still exists at this laser pump power. The transient loop shows no obvious difference in the demagnetization process except the amplitude of $\Delta\theta_K$. With the delay time increase, the shape of the loop changes. In the first part with the field over H_{ex}, the $\Delta\theta_K$ decreases with the increase of the field, which is counterintuitive compared with the normal hysteresis loop. The normal hysteresis loop is proportional to *M*, while the transient loop is proportional to ΔM, which is the demagnetization induced by laser pulse at the high field situation. Since the field could assist the remagnetization process, the ΔM is smaller at a higher field, and the effect of the field becomes more obvious with the delay time increasing. When the applied field is slightly smaller than the sample's H_{ex}, two peaks appear for the delay time up to 200 ps. In this situation, the effect of field is

more important. Since the interlayer antiferromagnetic coupling could be suppressed by the laser pulse, those spins whose direction is opposite to the field direction will be dragged by the field to the field's direction. Hence, the laser pulse combined with the applied field could induce a magnetization increase, which is also confirmed by TR-MOKE results seen in Fig 6.6.

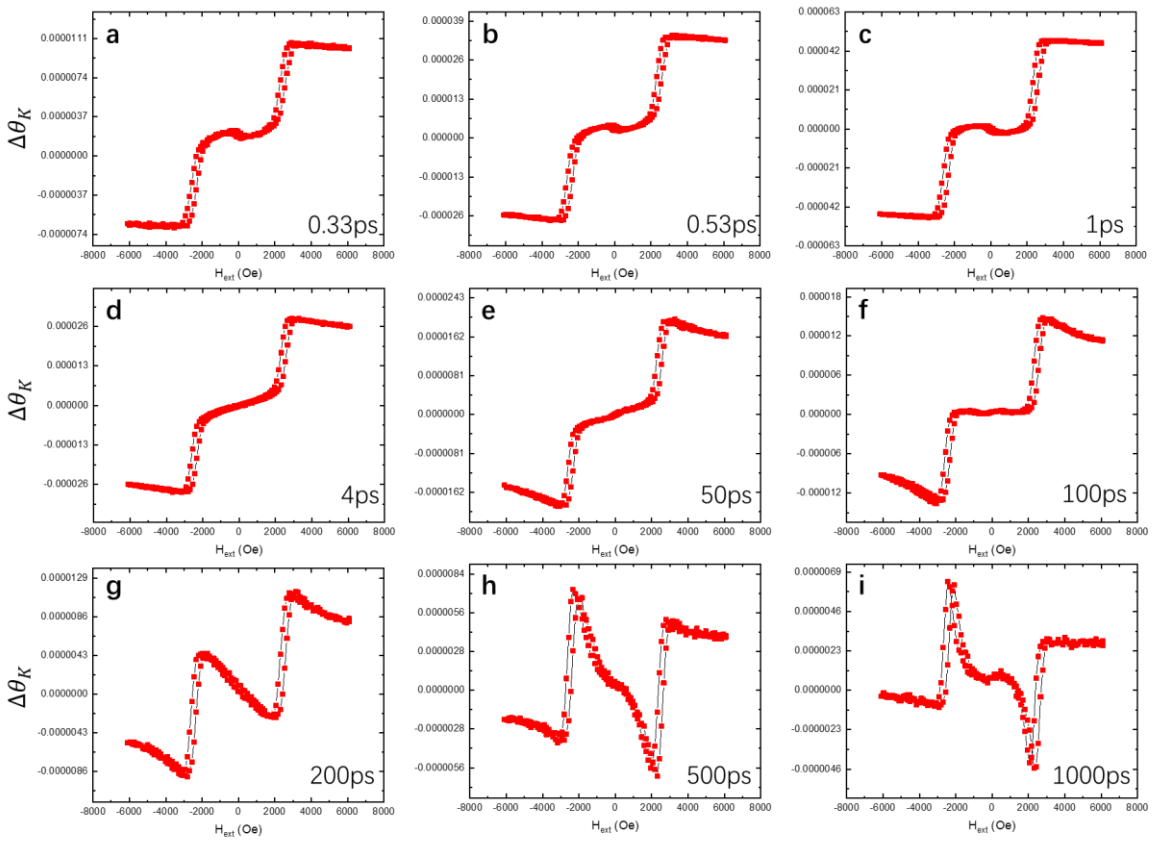

Figure 6.13 Transient magnetic polar Kerr loops of Pt/Co/Pt/Co/Ru (0.8 nm)/Co/Pt/Co/Pt thin film at 9 selected pump-probe delays as shown in Fig 6.12. The pump power is 12 mW, and the interlayer antiferromagnetic coupling exists at this pump power.

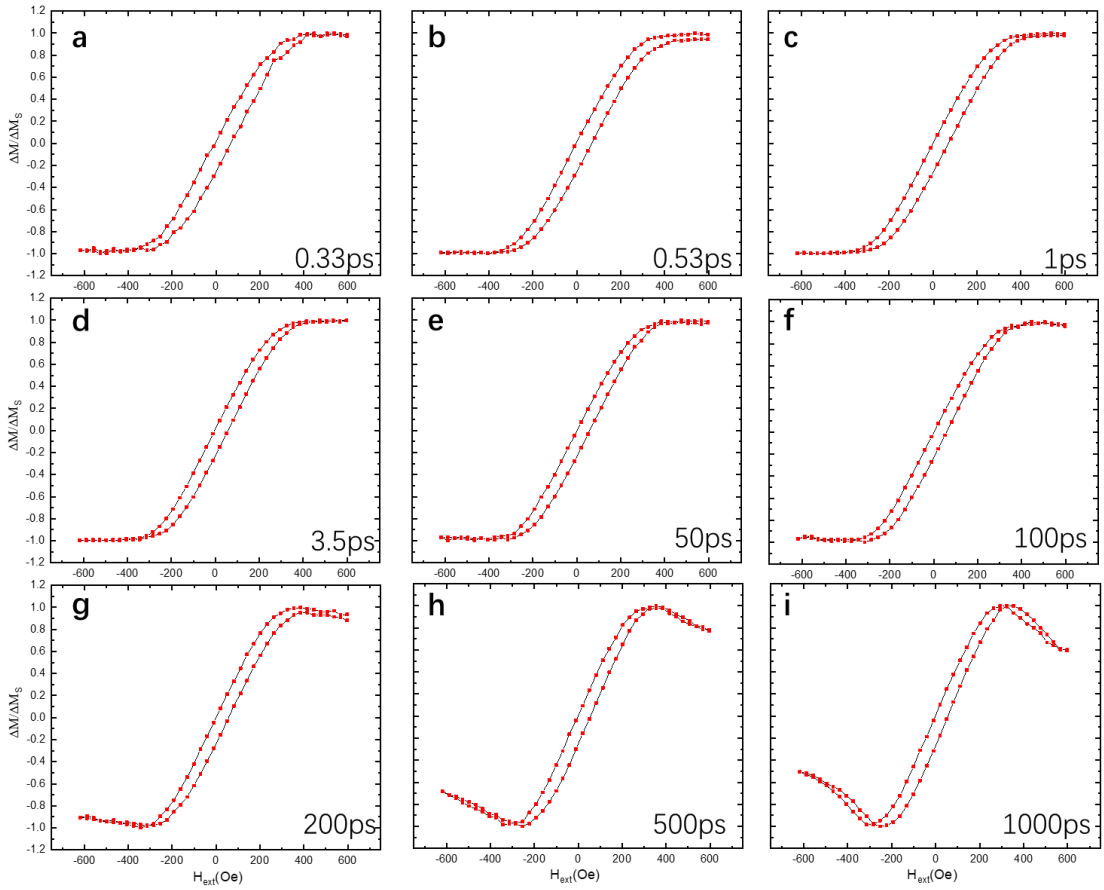

Figure 6.14 Transient magnetic polar Kerr loops of Pt/Co/Pt/Co/MgO (2.0 nm)/Co/Pt/Co/Pt thin film at 9 selected pump-probe delays as shown in Fig 6.12. The pump power is 8 mW, and the interlayer antiferromagnetic coupling exists at this pump power.

The interlayer antiferromagnetic coupling in the MgO spacer sample vanishes when the pump power exceeds 6 mW, as seen in Fig 6.10. One may concern about the dynamic process of this effect. However, the transient loop shows no interlayer antiferromagnetic coupling from the first point, as shown in Fig 6.14 (a), and the PMA vanishes as well. Therefore, the antiferromagnetic coupling induced by the 2 nm MgO spacer can be turned off at a pump power equal to and greater than 8 mW. It is necessary to point out here, that this antiferromagnetic coupling can recover before the next pulse arrives. As discussed in Chapter 3.2, the time-resolved MOKE measurement is based on a pulse-pulse repeatable signal. Limited by the length of our delay line, we can only confirm that the interlayer antiferromagnetic coupling is not recovered within 1 nanosecond. And it is recovered between each laser pulse, where in our experimental setup it is 1 ms. The IEC dynamic process is observed in the NiO spacer SAF sample. Before 1 ps delay time, the transient loop has the same pattern as the original hysteresis

loop. Up to 1 ps, a minor loop appears in the mid, and it becomes bigger with the increase of delay time. The coercivity of this minor loop is very close to that of the Co/Pt ferromagnetic state sample which is about 100 to 200 Oe. A small part of laser-induced spins no longer have the interlayer antiferromagnetic coupling, but the magnetic properties coming from Co/Pt interface still exist, therefore, the minor loop appears. Two peaks near the sample's H_{ex} are observed for NiO and MgO spacers when the delay time is over 200 ps, which indicates the interlayer antiferromagnetic coupling is suppressed. It is important to mention here, that although these peaks are not observed until 200 ps delay time, the antiferromagnetic coupling is suppressed once the laser pulse arrives. As discussed before, the remagnetization time is shorter with the increase of the applied field. But it is seen from the TR-MOKE results (Fig 6.6 and 6.7) that the remagnetization time is much shorter when the applied field is slightly smaller than the sample's H_{ex}. This is because the magnetization increase due to the applied field and laser heating speeds up the remagnetization, and therefore, the suppression of antiferromagnetic coupling exists after the laser pulse arrives. It is just covered up by the demagnetization and remagnetization process.

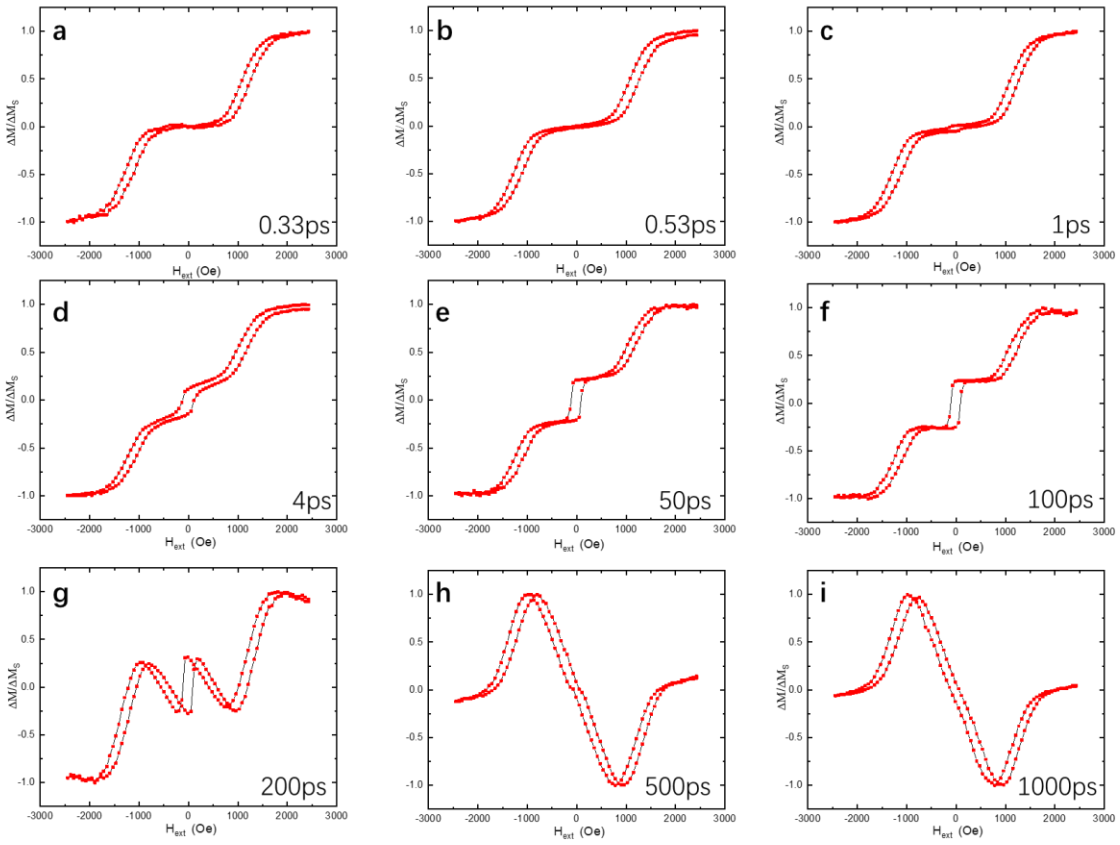

Figure 6.15 Transient magnetic polar Kerr loops of Pt/Co/Pt/Co/NiO (1.0 nm)/Co/Pt/Co/Pt thin film at 9 selected pump-probe delays as shown in Fig 6.12. The pump power is 4 mW, and the interlayer antiferromagnetic coupling exists at this pump power.

6.6 Discussion and Conclusion

The origin of different shapes of hysteresis loops should be discussed before its dynamic process aspect. Since the materials we studied have 4 ferromagnetic layers, their interaction is the key to explaining it. Three important parameters are introduced, including the coercivity of FM layers (H_c), the interlayer ferromagnetic coupling (H_{IFC}) and the interlayer antiferromagnetic coupling (H_{AFM}) as shown in Figure 6.16. To simplify this model, these interactions are presented in units of field, which indicates the field needed to overcome them and switches the magnetic direction to the field's direction. Firstly, if the AFM did not exist, the two-step hysteresis loop could still be observed when those four FM layers have different H_c and $H_c > H_{IFC}$. But this case can be excluded. H_c and H_{IFC} would not change with the thickness of the spacer changes. If this case was real, then all loops will have two steps. But it was not right. Also, we show in figure 6.17 that the coercivity of single layer Co/Pt was close

to 50 Oe, and all of the interlayer AFM is larger than it. Therefore, we confirm that the two steps loops come from the antiferromagnetic coupling.

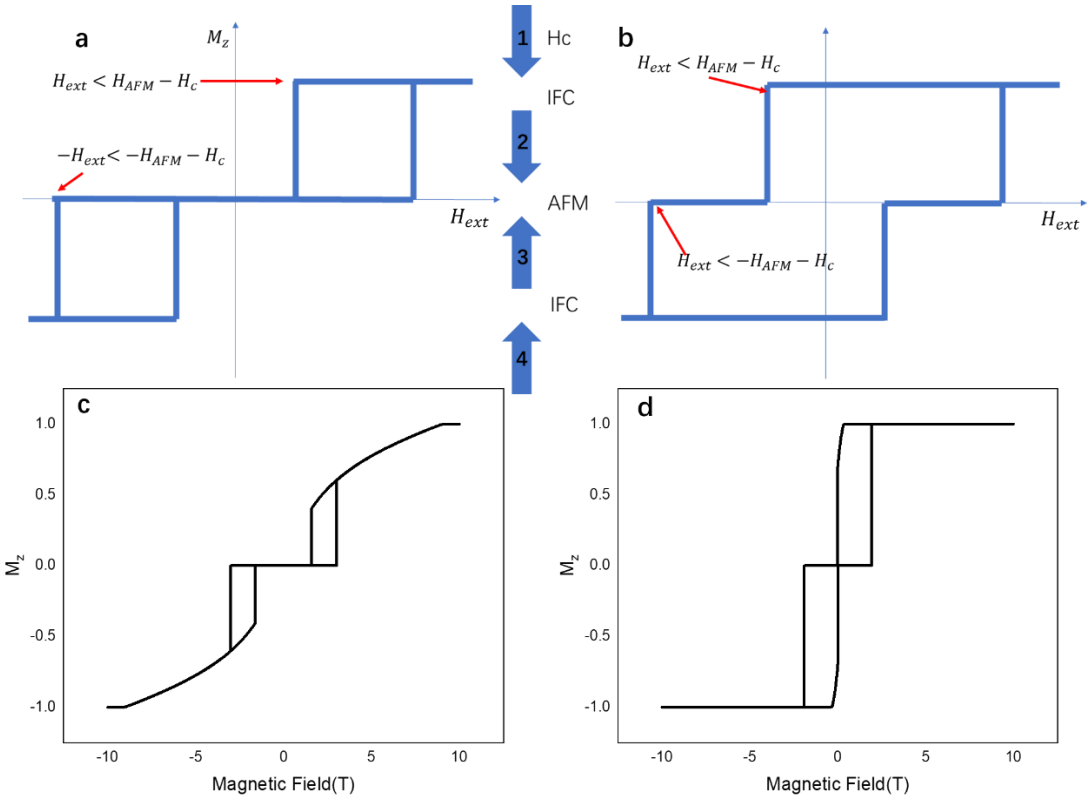

Figure 6.16 Three important parameters to explain different shapes of hysteresis loops. (a) The hysteresis loop of $H_{IFC} > H_{AFM} > H_c$. (b) The hysteresis loop of $H_{IFC} > H_c > H_{AFM}$. (c) and (d) shows the atomic simulation results.

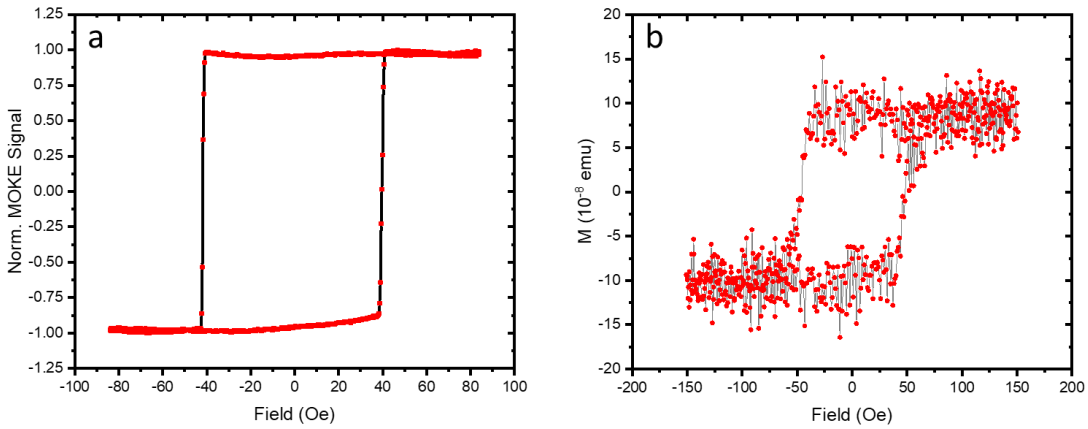

Figure 6.17 The single hysteresis loop of the out-of-plane Co/Pt multilayer sample. (a) was taken from MOKE image system, and (b) was taken from the VSM.

The switching process for $H_{IFC} > H_{AFM}\ and\ H_c$ is given here. When the magnetic field is high enough, all layers' magnetic direction is dragged to the external magnetic fields' direction. With the magnetic field decreased to $H_{AFM} - H_c$, layer 2 or 3 will be firstly switched. If $H_{AFM} < H_c$, then it was switched due to the AFM effect and the applied field, as shown in figures 6.16 b and d. Otherwise, it can be switched by AFM effect alone as shown in Figure 6.16 a and c. As the IFC effect is larger than the AFM effect, layer 1 or 4 will be switched by the IFC effect. After the external field could overcome the AFM and coercivity effect, all layers switched to the external field's direction. Therefore, there are only two steps in the hysteresis loop.

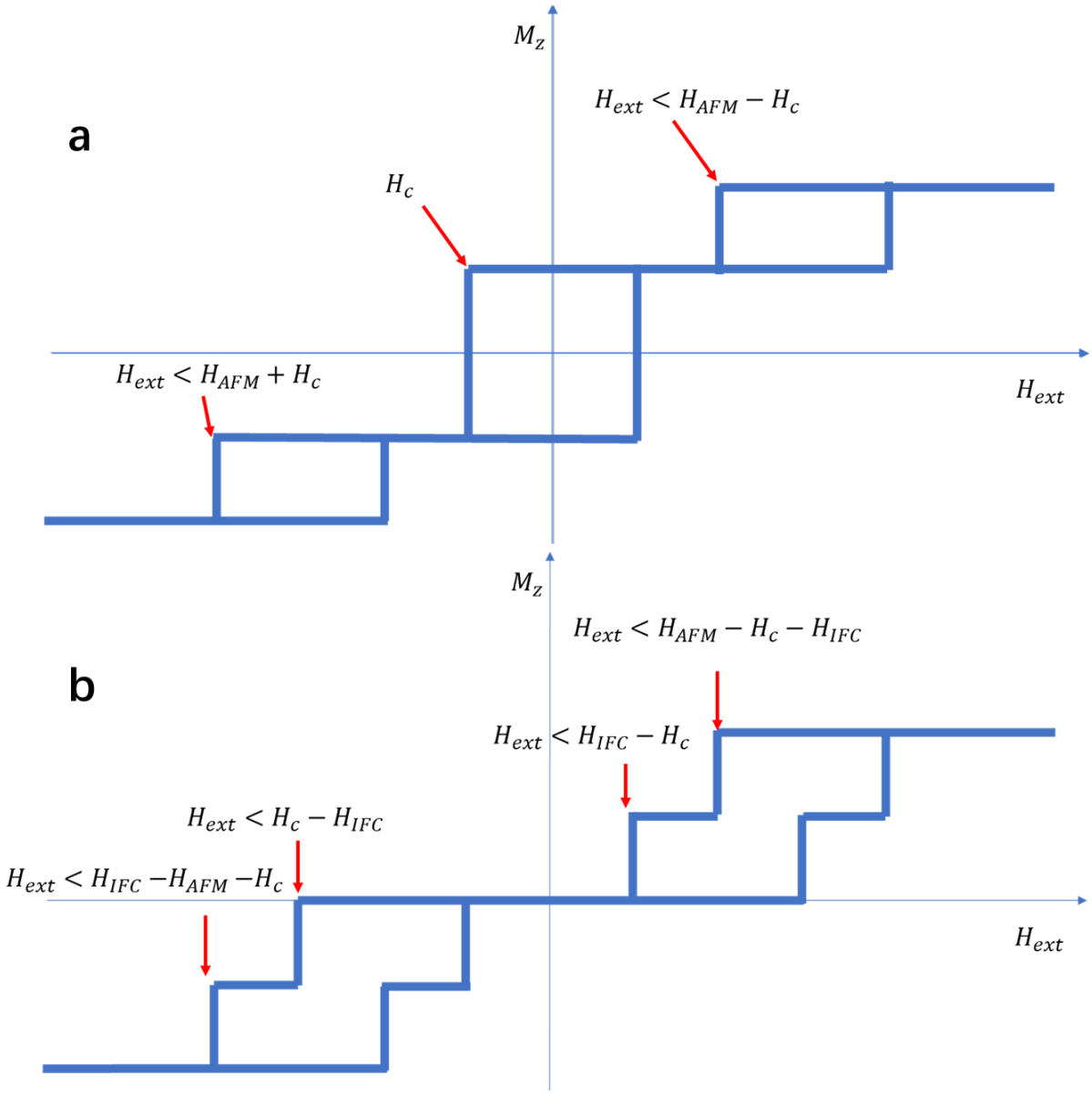

Figure 6.18 The schematic hysteresis loop for $H_{AFM}\ and\ H_c > H_{IFC}$ and (a) $H_{IFC} = 0$ (b) $H_{IFC} \neq 0$.

More steps in the hysteresis loops will be observed in the situation for $H_{AFM}\ and\ H_c > H_{IFC}$. We start with the switching process of Figure 6.18 (b) step by step. At first, all layers align with the external field. When the external field is lower than $H_{AFM} - H_c - H_{IFC}$, layer 2 will be switched due to the AFM effect. With the field decreasing to $H_{IFC} - H_c$, layer 2 will switch layer 1 due to the IFC effect. Then the field is lower than $H_c - H_{IFC}$, and layer 4 will be switched. Layer 3 is not switched until the field is lower than $H_{IFC} - H_{AFM} - H_c$. Since 4 layers switch independently, there are 4 steps in the hysteresis loop. It is important to mention that the shape of Figure 6.18 (a) is close to the Figure 6.15 (e), which proves that not only the interlayer antiferromagnetic coupling but also the interlayer ferromagnetic coupling will be decreased by the laser's heating effect, even though one of the spacers is metal and another is insulator.

The laser's heating effect is normally considered to demagnetize the sample, but the unusual magnetization increasing at such long timescale in SAF has not been reported before. This effect is attributed to AFM IEC suppressed by the laser heating effect, and this process is explained in Fig 6.16. We suggest that both AFM and IEC are suppressed once the laser pulse arrives. However, in the case of strong AFM and IEC, for example, in Ru and NiO spacer, the AFM IEC is just suppressed partly, while in the case of weak AFM IEC with MgO spacer, the AFM IEC can be fully suppressed. Since the AFM IEC is suppressed, the applied field will drag the spins to its direction, which results in a Kerr signal increasing. But in Fig 6.16 (b), all the spins are dragged to the field direction before laser's excitation. Therefore, no Kerr signal increase was observed.

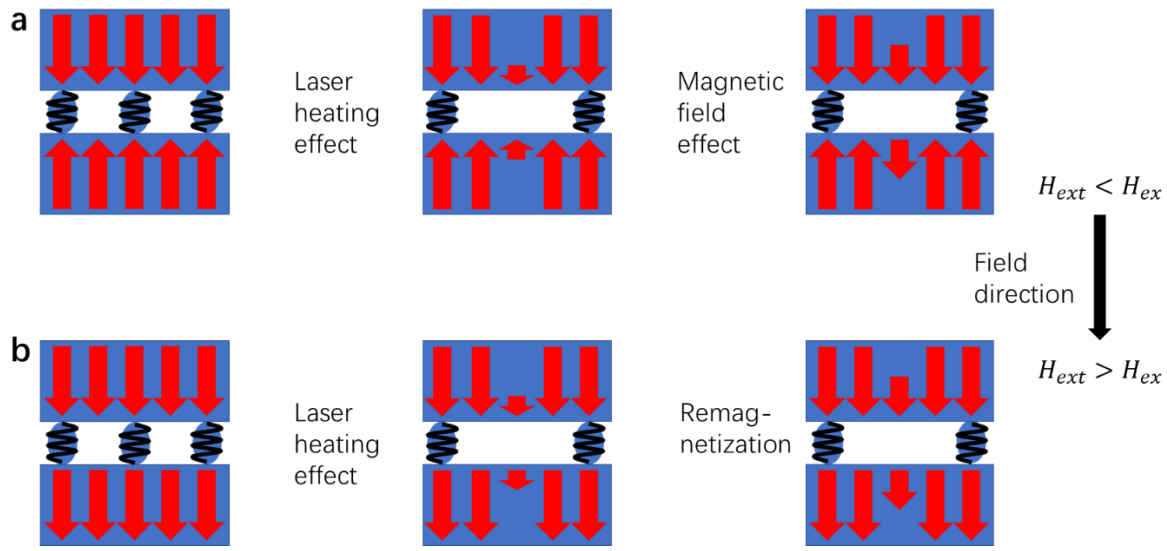

Figure 6.19 Schematic diagrams AFM IEC suppressed by laser heating effect. (a) Diagram for the applied magnetic field is smaller than H_{ex} and (b) the applied magnetic field is greater than H_{ex}.

The ultrafast demagnetization and relaxation process are usually described by the well-known phenomenological thermodynamic model, called three-temperature model [15, 203, 204]. These three subsystems include the electron, lattice and spin system, while their characterized relaxation times are described by τ_E, τ_M. Under the low-laser-fluence limit, which means the electron temperature rises instantaneously, the dynamic behaviour of a ferromagnetic system is described by the following differential equation [203]:

$$-\frac{\Delta M_z}{M_z} = \left[\left(\frac{A_1}{(t/\tau_0+1)^{1/2}} - \frac{(A_2\tau_E - A_1\tau_M)e^{-t/\tau_M}}{\tau_E-\tau_M} - \frac{\tau_E(A_1-A_2)e^{-t/\tau_E}}{\tau_E-\tau_M}\right)\Theta(t) + A_3\delta(t)\right] \otimes \Gamma(t)$$

Equation 6.2

Here the laser pulse duration is presented by the Gaussian function $\Gamma(t)$, and $\Theta(t)$ is the step function. These constants A_1, A_2, and A_3 are related to the system's intrinsic properties. And as early as 2008, TR-MOKE was used to measure the ultrafast demagnetization in SAF by Koopmans' group [205]. By fitting with the equation 6.2, they demonstrated that an interlayer transfer of spin angular momentum increases the demagnetization process speed in SAF system with conductive spacer Ru, while not in insulating spacer NiO. Also, a previous study found that the demagnetization in an antiferromagnetic state is much faster than a ferromagnetic state in one and same material – metallic dysprosium, and they suggested that it is due to the interatomic transfer of angular momentum with the spin system [206]. Moreover, it was

reported that three different demagnetization processes were observed in the thin $[Ni/Co]_4/Ru/[Co/Ni]_3$ SAF system [83] related to the applied magnetic field. Our results are not consistent with the previous study, and clearly, the ultrafast demagnetizing time increases with the decrease of the applied field, as shown in Figs 6.6 and 6.7 (b)

The phenomenological bi-exp and Tri-exp decay models were used to fit the TR-MOKE results. Although the bi-exp decay model fits the TR-MOKE results with an applied field greater than H_{ex} very well, both models cannot fit the results with an applied field smaller than H_{ex}. The previous models might not be suitable to explain our observations. To explain this new phenomenon, the suppression of the interlayer antiferromagnetic coupling by the laser's heating effect should be added to the model. Since the demagnetization process is in the picosecond timescale, the applied field's impact is ignorable. The original demagnetization time constant (τ_m^o) is provided by the TR-MOKE results in the high field ($H_{ext} > H_{ex}$). For the antiferromagnetic state, the demagnetization signal can be considered separately. The Kerr signal comes from both top and bottom Co/Pt multilayer. In the antiferromagnetic state, M_s^t is the same size as M_s^b, but their direction is opposite. As θ_K^t is greater than θ_K^b, and therefore $\Delta\theta_K = \Delta\theta_K^t + \Delta\theta_K^b > 0$, since all experimental conditions are not changed except the applied field (which has negligible affection to the demagnetization), the τ_m^o should be the same for different applied fields. Therefore, the difference of demagnetization comes from the interlayer antiferromagnetic coupling, where the remagnetization process is affected by both applied field and interlayer antiferromagnetic coupling. To describe the SAF system's dynamic process, the interlayer antiferromagnetic coupling should be added. The relaxation of IEC is much longer than the lattice relaxation time when comparing Fig 6.17 (a) with Fig 6.7 (a). For the same pump power of 12 mW, it is obvious that the relaxation time of $\Delta\theta_k$ is longer than 1 ns, while ΔR recovers within 400 ps. This comparison of $\Delta\theta_k$ and ΔR indicates that IEC is much more sensitive to temperature. It is important to note that the second peak was observed in the transient reflectivity, as shown in Fig 6.17(b). We suggest that this peak comes from the hot electron reflected by the Pt/Ru interface.

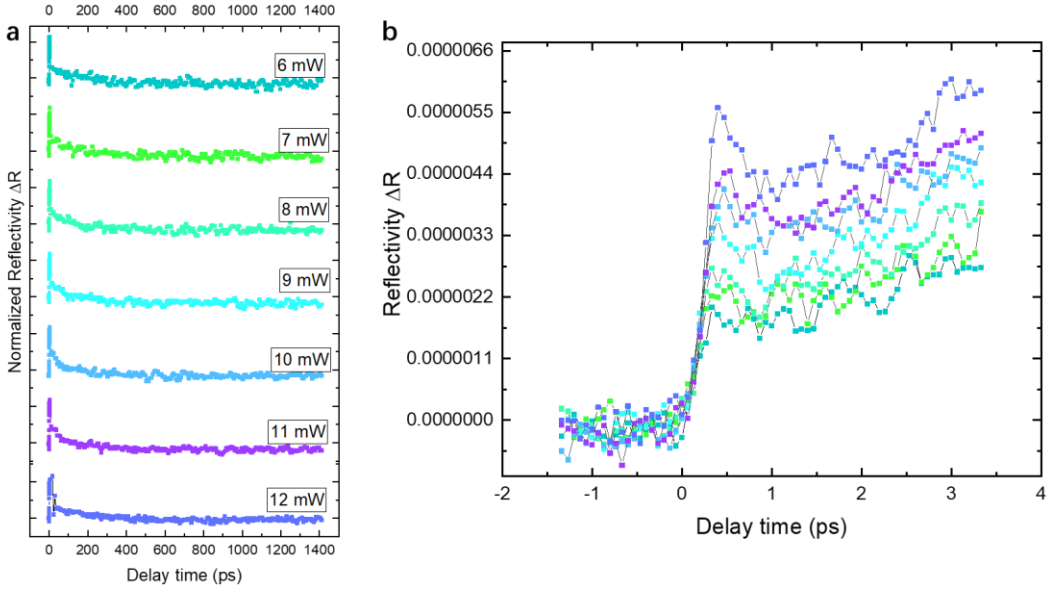

Figure 6.20 (a) Normalized dynamic reflectivity signals for $[Pt/Co]_2/Ru$ (0.8 nm)/$[Co/Pt]_2$ measured at different pump fluence without applied field. (b) shows the first 3.5 ps process.

In conclusion, three series of SAF samples with three types of IEC were grown by magnetron sputter system to study the IEC dynamic process. The strength of IEC varies with the types and thickness of spacers. Both time-resolved MOKE measurements and transient hysteresis loops prove that the laser pulse can suppress the interlayer antiferromagnetic coupling. Especially for the SAF sample with MgO spacer, the interlayer antiferromagnetic coupling could be totally quenched by the laser pulse with a pump power equal to and greater than 8 mW. At high pump fluence, the film is driven from the antiferromagnetic coupling to the ferromagnetic coupling with a characteristic time comparable to the pulse duration in the SAF sample with an MgO spacer. These results demonstrate that the laser pulse could manipulate IEC in the SAF system. While for the SAF sample with NiO spacer, some of the laser-induced spins show no antiferromagnetic coupling, which induces a triple-loop pattern after 1 picosecond. Moreover, compared with the e-field manipulation, IEC is quite fragile under ultrafast laser heating, while about 5% of laser power for all-optical switching (AOS) is enough to temporarily turn it off even though the AFM coupling effective field is up to 2 kOe. However, to fully describe the ultrafast dynamic properties of SAF, a new theoretical model might be needed.

Chapter 7 Future work

7.1 Potential of enhancing AOS with 2D $MoSe_2$

As promising candidates for the next generation spintronic and valleytronics devices, TMDC materials have cut a conspicuous figure. The multitudinous exotic physical phenomenon can emerge leading from the varieties in the bandstructure when materials change from the bulk to a few layers [39]. The electron's spin degree of freedom (DOF) was discovered with the development of quantum physics. While for the valley DOF, it was first discovered in 2004 when researchers at the University of Manchester first mechanically exfoliated the monolayer graphene from bulk graphite [207]. The valley DOF is regarded as pseudospin, which could be a potential information carrier. Two-dimensional (2D) materials, such as graphene and TMDC, provide a stage to study the valley DOF. Compared with graphene, monolayer TMDC has a strong spin-orbital coupling, and broken inversion symmetry and these two lead to coupled spin and valley [208]. Moreover, monolayer TMDC has a direct bandgap at the K point.

Those characteristics attract researchers to focus on its electron properties, such as the spin and valley relaxation channel [52, 209], the electrical mobility [38, 42], and the transport properties [210]. However, as TMDC materials are ionic solid, long-range macroscopic electric fields arise that are associated with long wave longitudinal optical phonons. These fields have an important impact on the transport properties of the monolayers [211]. More importantly, this leads to splitting between the LO and TO modes, driven by the long-ranged Coulomb interactions and electronic screening [212]. The relative vibration between positive and negative ions produces an electric dipole moment, which can interact with an electromagnetic wave. This interaction induces a strong absorption in the far-infrared region. In this section, we have proposed to use the TMDC material such as $MoSe_2$ to enhance the HD-AOS. MoSe2 is a 2D material with a bandgap close to 800 nm, and its most important feature is that the valley and spin degree is coupled in this material [61, 213]. Using a circularly polarized laser could excite 100 % spin polarization electrons. Therefore, integrating MoSe2 with the HD-AOS materials may improve efficiency. In this section, we tested the 2D TMDC material – $MoSe_2$ – which has a theoretically 100% optical controlled spin polarization. We observed the laser-induced spin polarization, and its relaxation time is susceptible to the temperature. Also, the temperature-dependent transition behaviour was observed, which is due to the phonon-assisted transition.

7.1.1 Method

All the calculations are based on the local density approximation (LDA) as implemented in the plane wave code CASTEP[214], and the version is 7.03. As the phonon calculation cannot use the ultrasoft pseudopotential, the keyword NCP is used to generate the pseudopotential automatically. In consideration of the periodic boundary, a vacuum of 20 Å between the layer and the cell constraint at the C axis is set to eliminate the layer interaction. First, the geometry optimisation task is done to get the structure relaxed, with the forces becoming smaller than 0.05 $\mathrm{eV\AA^{-1}}$ and the energy tolerances being less than $2 \times 10^{-5}\ \mathrm{eV/atom}$. The geometry optimisation for monolayer $MoSe_2$ is very sensitive to the k point grid parameter and the cut off energy, and here $8 \times 8 \times 2$ Monkhorst-Pack K-points with a plane wave cut off energy of 1240 eV (PRECISE) is used to get a successful geometry optimisation. Then the geometry optimisation gives the check file, which is used for the DFPT and bandstructure calculation. Also, the DFPT's check file is used to do the phonon dispersion calculation. In that way, we can avoid doing the expansive DFPT calculation.

7.1.2 Preliminary Results

Fig 7.1 shows the unit cell of $MoSe_2$ with the left is the bulk and the right is monolayer. It is obviously that centrosymmetry is broken in the monolayer $MoSe_2$. The lattice vector for monolayer $MoSe_2$ is slightly smaller than the bulk $MoSe_2$. As shown in Fig 7.1 (b), the bandgap of the monolayer becomes a direct bandgap, while it is an indirect bandgap in bulk $MoSe_2$. The bandgap here is 1.570 eV, which is consistent with our experimental result (1.569 eV). Another important thing about the bandstructure of monolayer $MoSe_2$ is that, according to the theory calculation [215], there is the Dirac cone in the K point of the Brillouin zone. However, the energy dispersion near the K point is flat. The reason is that we set a wrong Brillouin zone path for monolayer $MoSe_2$. Because for monolayer $MoSe_2$, the Brillouin zone should be two dimensional as well, and the energy dispersion for H point is the same as the K point. Therefore, the energy dispersion between the H and K points is flat. This phenomenon also appears in the phonon spectra, as shown in Fig 5.11.

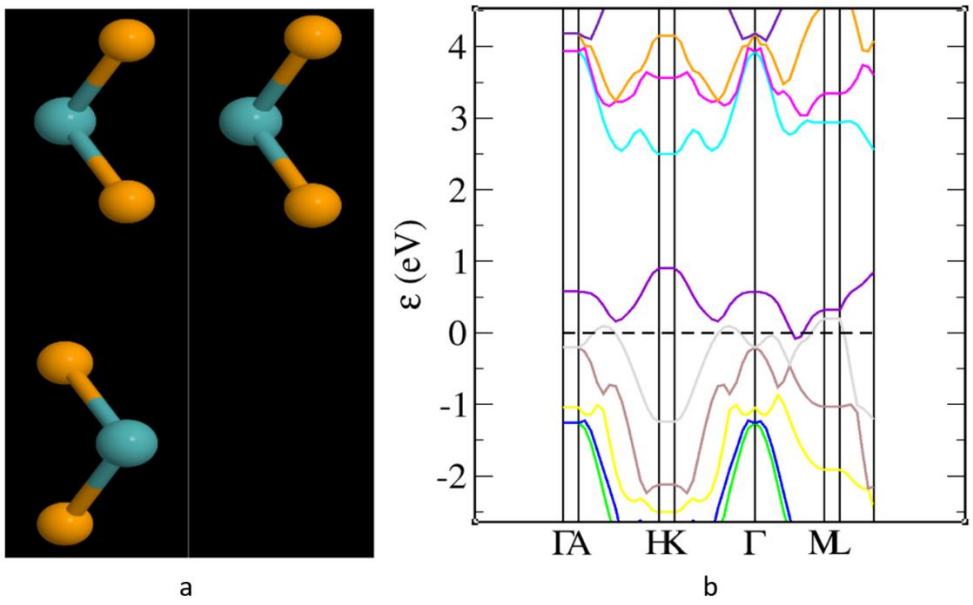

Figure 7.1 The front view of the 2H-$MoSe_2$ unit cell, the left is the bulk, and the right is the monolayer. (b) The bandstructure of monolayer $MoSe_2$.

Table 7.1 Born effective charges in the monolayer $MoSe_2$.

	$Z_{\kappa,\beta,\alpha}$(e)			Z_{av}(e)
	0.90705	0.00000	0.00000	
Se	0.00000	0.90705	0.00000	0.63599
	0.00000	0.00000	0.09388	
	-1.81409	0.00000	0.00000	
Mo	0.00000	-1.81409	0.00000	-1.27198
	0.00000	0.00000	-0.18776	
	0.90705	0.00000	0.00000	
Se	0.00000	0.90705	0.00000	0.63599
	0.00000	0.00000	0.09388	

Table 7.1 shows the Born effective charge of monolayer $MoSe_2$. Obviously, the average effective charge for the Mo atom is positive, -1.27198 e, while for the Se atom is negative,

0.63599e. This confirms that $MoSe_2$ is polar material, and the average effective charge is huge compared with other materials, which will induce a strong dipole-dipole interaction. Also, the effective charge at the x and y-axis is larger than it at the z-axis, which is due to the mirror symmetry in the z-direction. Therefore, this asymmetry will induce a significant LO-TO splitting.

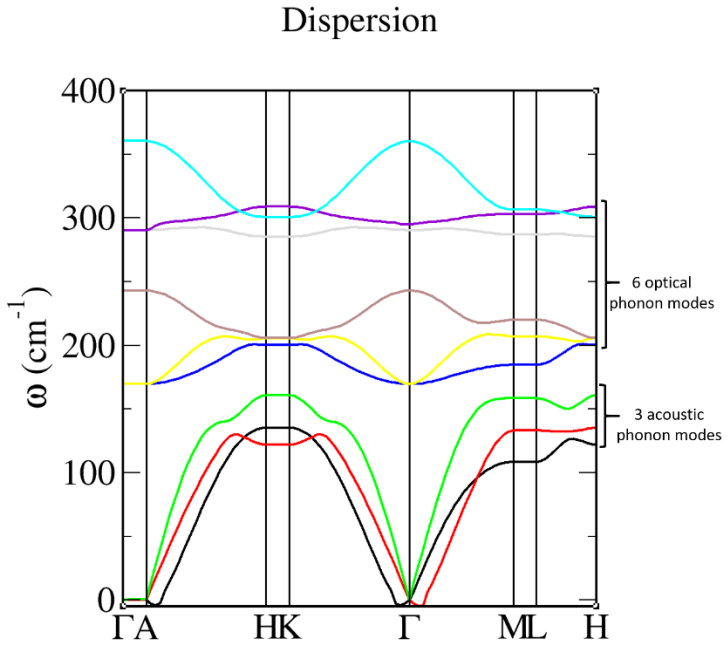

Figure 7.2 The phonon dispersion of the monolayer $MoSe_2$.

Fig 7.2 gives all 9 phonon modes' frequency at the Γ point, here mode 1,2,3 are the acoustic phonon mode, which corresponds to the motion of the unit cell as a whole. While mode 4 to 9 are the optical mode, corresponding to the relative motion with the centre of mass having no motion. Normally, acoustic mode frequency should be zero at the Γ point, but it is unusual that the frequencies of mode 1 and 2 are negative. Here I suppose it is due to the calculation error. For the optical phonon modes 4 to 6, the Mo atom does not move, and two Se atoms have relative motion. Mode 4 and 5 motions are at the x-y plane, the TO phonon mode, and Mode 6 motion is at the z-direction, the LO phonon mode. Mo atom and two Se atoms have the relative motion for Mode 7 to 9, and their frequencies are much higher than in the previous mode. Here mode 7 to 8 are the TO phonon mode and mode 9 is the LO phonon mode. There is a large LO-TO splitting in the monolayer $MoSe_2$ due to the large difference in the Born effective charge in different directions.

Phonon mode	$\omega(cm^{-1})$
1	-0.017188
2	-0.017188
3	0.011284
4	169.609590
5	169.609590
6	243.008150
7	290.413379
8	290.413379
9	360.492735

a

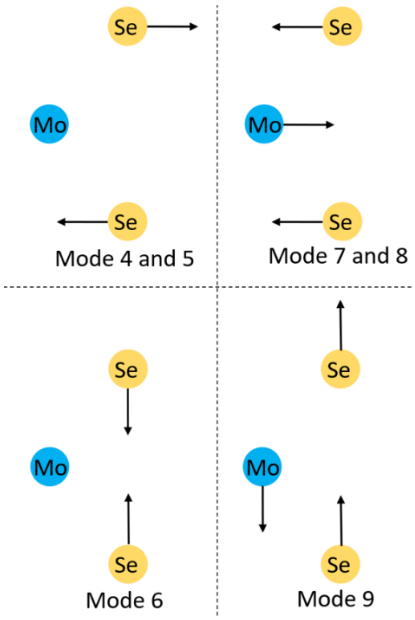

b

Figure 7.3 (a) The 9 phonon modes' frequency at the Γ point. (b) The schematic diagram of the different phonon modes.

Fig 7.3 (a) shows the sample we used in our measurements, grown by the chemical vapor deposition (CVD) method with a size length of about 75 μm. The optical contrast confirms that the sample comprises a monolayer $MoSe_2$ crystal with a tiny region of bilayer or multilayer $MoSe_2$ and several defects. Furthermore, Raman spectra also will be used to confirm the layer number of our sample. Typically, the scale of CVD-grown monolayer $MoSe_2$ is larger than the mechanical exfoliated $MoSe_2$. However, it may interact with the substrate and has more defects, which considerably affects to the band structure [216].

a b

Figure 7.4 (a) The optical microscope image of monolayer $MoSe_2$. The magnification times of the microscope are 500, and the monolayer triangle's side length is about 75 micrometres. (b) Diagram of the experimental geometry. Both wavelengths of the pump and the probe are the same, and the incident angle of the pump beam is about 45°.

Fig 7.4 (b) shows the experimental geometry, the laser source used in the measurements is an 80 MHz pulse laser and a pulse width of fewer than 200 femtoseconds. The wavelength of the pump and the probe beam is the same, and it is tuned from 760 nm to 860 nm with an average power of 0.8 W. The sample was put into a microcrystal, while liquid nitrogen is used to cool it.

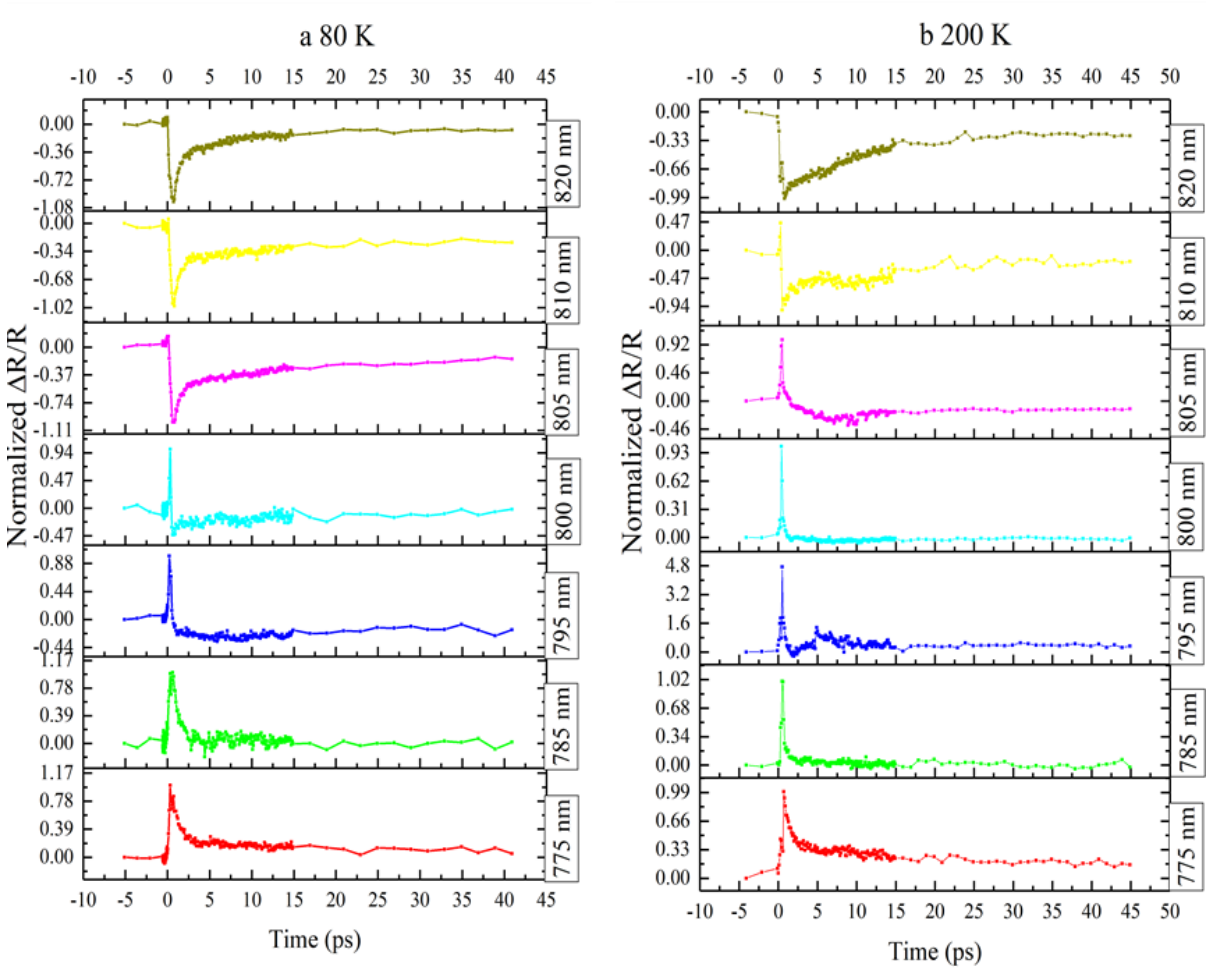

Figure 7.5 Wavelength dependence of electron relaxation time in monolayer $MoSe_2$ based on the degenerate time-resolved pump-probe measurement. (a) the transient reflection induced by the pump beam decreases with the wavelength increase, and it downs to negative when the wavelength is greater than 785 nm at 80 K. (b) the reflection decreases to negative at 805 nm.

Fig 7.5 shows results for the 2D TMDC sample. The transient reflection induced by the pump pulse is positive when the photon energy is higher than the bandgap, which is about 1.55 eV (790 nm) at room temperature confirmed by PL [217]. When the wavelength rises to 795 nm, the transient reflection at 80 K goes negative at only several picoseconds after the zero delays. While at 200 K, it keeps positive all the time. Since the bandgap of $MoSe_2$ is dependent on the temperature [218], this phenomenon can be easily understood. With the photon energy decreasing consistently, the transient reflection goes down to negative quickly. And when the photon energy is much lower than the bandgap, the reflection only has a negative part.

Fig 7.6 shows the transient Kerr signal pump by circularly polarized laser pulses. It is important to note that the Kerr signal is different from the previous magneto-optical effect, but it comes from the selective absorption of the monolayer $MoSe_2$. As shown in Fig 7.6 a and b, a strong Kerr signal is observed at the first 2 picoseconds, and its direction is related to the pump's polarization. The relaxation time of the Kerr signal is inversely proportional to the temperature.

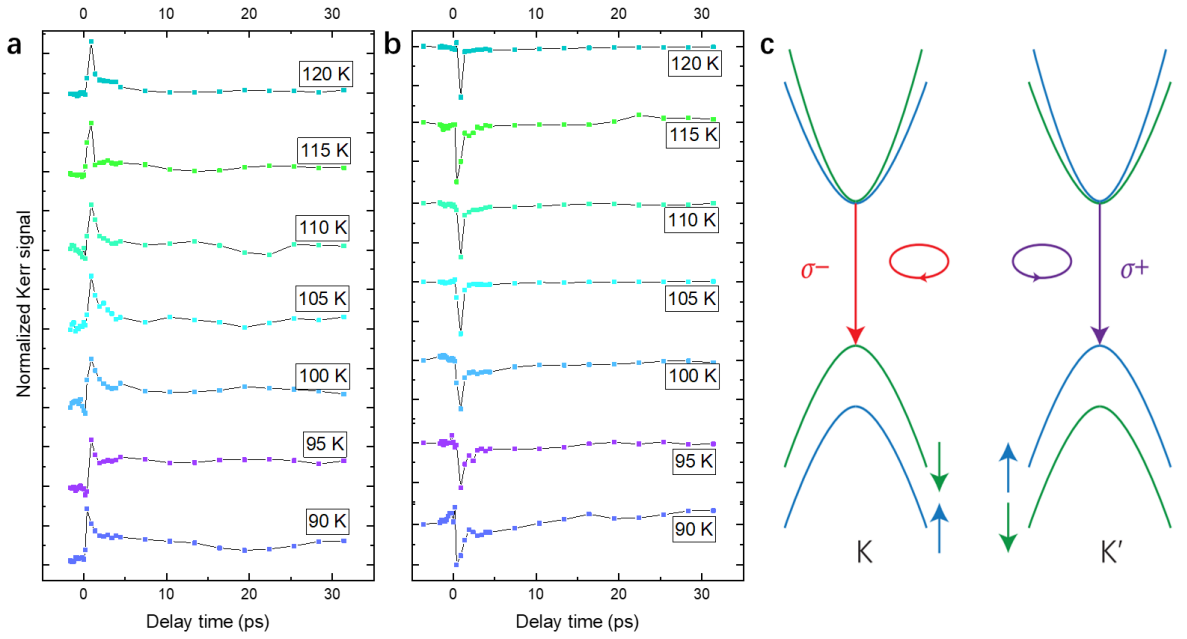

Figure 7.6 Temperature dependence of Kerr signal relaxation time in monolayer $MoSe_2$ based on the degenerate time-resolved pump-probe measurement. (a) pumped by 800 nm left-handed circularly polarized laser pulse. (b) pumped by 800 nm right-handed circularly polarized laser pulse.

In conclusion, according to the first principle calculation, after being excited by an 800 nm circularly polarized laser, monolayer $MoSe_2$ will have 100 % spin polarization. This phenomenon was observed at low temperatures. With the temperature lower than 100 K, spin relaxation time is longer than 30 ps. In the next step, after being grown by the magnetron sputtering system, the Pt/Co/Cu sample will be moved to the chemical vapor deposition chamber, and the monolayer $MoSe_2$ will be grown at the top of the Pt/Co/Cu layer. The final sample structure will be Glass/Ta/Pt/Co/Cu/$MoSe_2$. The top Cu layer was used to improve the spin injection from $MoSe_2$ to the Co layer since the Cu layer has a longer spin relaxation length than the Pt layer. After being excited by the laser pulse, the top $MoSe_2$ will have a 100 % spin polarization. And those itinerant spin polarized electrons will transport to the Co layer, as the

latter has a lower Fermi level. Although the spin relaxation is shorter than 2 ps at high temperature, the optical spin injection will help all-optical switching. We expect that this optical spin injection could improve the energy efficiency of AOS.

7.2 Potential of dual-pulse AOS in SAF materials

Single-pulse HD-AOS has not been observed until today. Multi-pulse all-optical switching is not energy efficient, so single-pulse HD-AOS becomes a key goal. Previous single-pulse AOS is based on ferrimagnetic materials, including GdFeCo, Co/Gd multilayer, MnRuGa. Therefore SAF is considered a great candidate for single-pulse AOS. As the laser pulse can suppress the RKKY coupling, as shown in chapter 6, the SAF system effectively allows all-optical switching. Also, the dual-pulse experiment in chapter 4 shows that the laser pulse's heating effect could assist the HD-AOS. Therefore, we consider building a dual-pulse system to switch the SAF sample. The first linearly polarized pulse could turn off the AFM coupling between two FM layers. As the required power for the first pump pulse is much lower than the full demagnetization power, M_1 and M_2 should not be decreased significantly. Therefore, after the AFM coupling is turned off, the antiparallel aligned moment system is extremely unstable. A small perturbation may be required to switch one of the FM layer's magnetic directions. The second circularly polarized pulse provides helicity effect, which could be regarded as an effective magnetic field. Although this field duration has the same time scale as pulse duration, we expect it is high enough to convert the system to a transient FM state since this field is expected to be larger than 10 Tesla [30] when the pulse fluence is $10\ mJ/cm^2$. According to a previous study, this system converts to parallel aligned under 2 ps with a 1 kOe external magnetic field [83]. After that, the RKKY recovers with the system temperature decrease. Then the FM layer with lower magnetic anisotropy energy will be switched, and the system will go back to an AFM state.

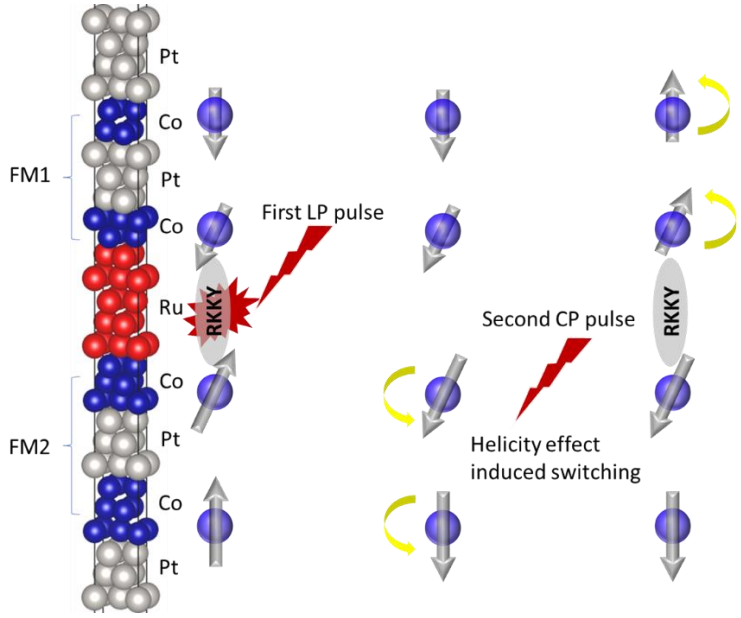

Figure 7.7 The SAF structure for all-optical switching and the switching process.

List of abbreviations

2D	two-dimension
3TM	three temperature model
AD	areal density
AFM	antiferromagnetic
AOS	all-optical switching
BCC	body centre cubic
BBO	Beta barium borate
CCD	charge-coupled-device
CMOS	complementary metal-oxide-semiconductor
CP	circularly polarized
DC	direct current
DOF	degree of freedom
DFT	Density Functional Theory
FWHM	Full width at half maximum
FM	ferromagnetic
GGA	Generalized Gradient Approximation
GMR	giant magnetoresistance
HAMR	heat-assisted magnetic recording
HD-AOS	helicity-dependent all-optical switching
HDD	hard disk drive
HID-AOS	helicity-independent all-optical switching
IFE	inverse Faraday effect
IEC	interlayer exchange coupling
LCP	left-handed circular polarized laser
LDA	Local Density Approximation
LED	light-emitting diode
LLG	Landau–Lifshitz–Gilbert
LP	linearly polarized
M3TM	microscopic 3 temperature model
MCD	magnetic circular dichroism
MOKE	magneto-optical Kerr effect
MR	magnetoresistance

MRAM	magnetic random-access memory
MRG	Mn_2Ru_xGa
NM	nonmagnetic
PBE	Perdew-Burke-Ernzerhof
PL	photoluminescence
PMA	perpendicular magnetic anisotropy
PRML	partial response maximum likelihood
RAMAC	random access method of accounting and control
RKKY	Ruderman-Kittel-Kasuya-Yosida
SAF	synthetic antiferromagnetic
SRC	stimulated Raman scattering
TMC	transition metal carbides
TMDC	transition metal dichalcogenides
VASP	Vienna Ab initio Simulation Package
VSM	vibrating-sample magnetometer
XMCD	X-ray magnetic circular dichroism

List of symbols

β	Faraday rotation
δ	skin depth
ε	permittivity tensor
h	Planck's constant
$\hbar$	reduced Planck's constant
θ_k	Kerr rotation
η_k	Kerr ellipticity
γ	gyromagnetic ratio
ρ	resistivity
μ_r	relative magnetic permeability
μ_0	permeability of free space
μ_B	Bohr magneton
λ	wavelength of light
ω	angular frequency of the magnetisation precession
τ	precession decay time
τ_E	electron scattering time
τ_M	ultrafast demagnetisation time
$\langle \boldsymbol{S} \rangle$	spin operator
$\mathcal{H}$	Hamiltonian
$\mathcal{J}_{ij}$	exchange integral
a_0	lattice constant
g	Landé g factor
$\boldsymbol{k}$	wave vector
k_B	Boltzmann constant
m	magnetic moment
n	refractive index
s	total spin number
z	nearest-neighbour number
B	magnetic flux density

G_{ij}	coupling constant between electrons, spins, and lattice
$\boldsymbol{H}$	magnetic field
$\boldsymbol{H_{\mathrm{eff}}}$	effective magnetic field
I	light intensity
J	exchange constant
K_{u}	uniaxial anisotropy constant
K_1	first-order cubic anisotropy constant
M_s	saturation magnetisation
$\boldsymbol{M}$	magnetization
N	complex indices of refraction
N_v	number of nearest-neighbour moments per unit volume
Q	complex magneto-optical constant
T_C	Curie temperature
T_{e}	electron temperature
T_{s}	spin temperature
T_{l}	lattice temperature

References

1. Anderson, D., *HDD Opportunities & Challenges, Now to 2020.* 2013.
2. IBM. *RAMAC: The First Magnetic Hard Disk*. 1957 [cited 2020 16/03]; Available from: https://www.ibm.com/ibm/history/ibm100/us/en/icons/ramac/impacts/?mhsrc=ibmsearch_a&mhq=305%20RAMAC.
3. Baibich, M.N., et al., *Giant magnetoresistance of (001) Fe/(001) Cr magnetic superlattices.* Physical review letters, 1988. **61**(21): p. 2472.
4. Binasch, G., et al., *Enhanced magnetoresistance in layered magnetic structures with antiferromagnetic interlayer exchange.* Physical review B, 1989. **39**(7): p. 4828.
5. Tsang, C., *12 Gb/in2 recording demonstration with SV read heads & conventional narrow pole-tip write heads.* IEEE Trans. Magn., 1999. **35**(2): p. 683.
6. Gittleman, J., B. Abeles, and S. Bozowski, *Superparamagnetism and relaxation effects in granular Ni-Si O 2 and Ni-Al 2 O 3 films.* Physical review B, 1974. **9**(9): p. 3891.
7. Iwasaki, S.-i. and K. Takemura, *An analysis for the circular mode of magnetization in short wavelength recording.* IEEE Transactions on Magnetics, 1975. **11**(5): p. 1173-1175.
8. Iwasaki, S. and Y. Nakamura, *An analysis for the magnetization mode for high density magnetic recording.* IEEE Transactions on Magnetics, 1977. **13**(5): p. 1272-1277.
9. Iwasaki, S., Y. Nakamura, and K. Ouchi, *Perpendicular magnetic recording with a composite anisotropy film.* IEEE Transactions on Magnetics, 1979. **15**(6): p. 1456-1458.
10. Toshiba. *Toshiba Leads Industry in Bringing Perpendicular Data Recording to HDD--Sets New Record for Storage Capacity With Two New HDDs*. 2004 [cited 2020 18/03].
11. Richter, T. *Seagate develops hard disks with 24 TB memory and 480 MB/s*. 2019; Available from: https://www.slashcam.com/news/single/Seagate-develops-hard-disks-with-24-TB-memory-and--14895.html.
12. Kryder, M.H., et al., *Heat Assisted Magnetic Recording.* Proceedings of the IEEE, 2008. **96**(11): p. 1810-1835.
13. Eesley, G., *Observation of nonequilibrium electron heating in copper.* Physical review letters, 1983. **51**(23): p. 2140.
14. Bukin, N., et al., *Time-resolved imaging of magnetic vortex dynamics using holography with extended reference autocorrelation by linear differential operator.* Sci Rep, 2016. **6**: p. 36307.
15. Beaurepaire, E., et al., *Ultrafast spin dynamics in ferromagnetic nickel.* Physical review letters, 1996. **76**(22): p. 4250.
16. Anisimov, S., B. Kapeliovich, and T. Perelman, *Electron emission from metal surfaces exposed to ultrashort laser pulses.* Zh. Eksp. Teor. Fiz, 1974. **66**(2): p. 375-377.
17. Stanciu, C., et al., *All-optical magnetic recording with circularly polarized light.* Physical review letters, 2007. **99**(4): p. 047601.
18. Yang, Y., et al., *Ultrafast magnetization reversal by picosecond electrical pulses.* Science Advances, 2017. **3**(11): p. e1603117.
19. Mangin, S., et al., *Engineered materials for all-optical helicity-dependent magnetic switching.* Nature materials, 2014. **13**(3): p. 286.
20. Radu, I., et al., *Transient ferromagnetic-like state mediating ultrafast reversal of antiferromagnetically coupled spins.* Nature, 2011. **472**(7342): p. 205-8.
21. Ostler, T., *TA Ostler, J. Barker, RFL Evans, RW Chantrell, U. Atxitia, O. Chubykalo-Fesenko, S. El Moussaoui, L. Le Guyader, E. Mengotti, LJ Heyderman, F. Nolting, A. Tsukamoto, A. Itoh, D. Afanasiev, BA Ivanov, AM Kalashnikova, K. Vahaplar, J. Mentink, A. Kirilyuk, Th. Rasing, and AV Kimel, Nat. Commun. 3, 666 (2012).* Nat. Commun., 2012. **3**: p. 666.
22. Lalieu, M.L.M., et al., *Deterministic all-optical switching of synthetic ferrimagnets using single femtosecond laser pulses.* Physical Review B, 2017. **96**(22).

23. Lambert, C.-H., et al., *All-optical control of ferromagnetic thin films and nanostructures.* Science, 2014. **345**(6202): p. 1337-1340.
24. Hellman, F., et al., *Interface-induced phenomena in magnetism.* Reviews of modern physics, 2017. **89**(2): p. 025006.
25. Choi, G.M., A. Schleife, and D.G. Cahill, *Optical-helicity-driven magnetization dynamics in metallic ferromagnets.* Nat Commun, 2017. **8**: p. 15085.
26. Hoveyda, F., E. Hohenstein, and S. Smadici, *Heat accumulation and all-optical switching by domain wall motion in Co/Pd superlattices.* Journal of Physics: Condensed Matter, 2017. **29**(22): p. 225801.
27. Moreno, R., et al., *Conditions for thermally induced all-optical switching in ferrimagnetic alloys: Modeling of TbCo.* Physical Review B, 2017. **96**(1).
28. Gorchon, J., Y. Yang, and J. Bokor, *Model for multishot all-thermal all-optical switching in ferromagnets.* Physical Review B, 2016. **94**(2): p. 020409.
29. Khorsand, A.R., et al., *Role of magnetic circular dichroism in all-optical magnetic recording.* Phys Rev Lett, 2012. **108**(12): p. 127205.
30. Cornelissen, T., R. Córdoba, and B. Koopmans, *Microscopic model for all optical switching in ferromagnets.* Applied Physics Letters, 2016. **108**(14): p. 142405.
31. Kirilyuk, A., A.V. Kimel, and T. Rasing, *Ultrafast optical manipulation of magnetic order.* Reviews of Modern Physics, 2010. **82**(3): p. 2731-2784.
32. Berritta, M., et al., *Ab Initio Theory of Coherent Laser-Induced Magnetization in Metals.* Phys Rev Lett, 2016. **117**(13): p. 137203.
33. Zhang, G., et al., *First-principles and model simulation of all-optical spin reversal.* Physical Review B, 2017. **96**(13): p. 134407.
34. Quessab, Y., et al., *Helicity-dependent all-optical domain wall motion in ferromagnetic thin films.* Physical Review B, 2018. **97**(5).
35. Parlak, U., et al., *Optically induced magnetization reversal in [Co/Pt]N multilayers: Role of domain wall dynamics.* Physical Review B, 2018. **98**(21).
36. Du, X., et al., *Approaching ballistic transport in suspended graphene.* Nature nanotechnology, 2008. **3**(8): p. 491.
37. Zhang, Y., et al., *Experimental observation of the quantum Hall effect and Berry's phase in graphene.* nature, 2005. **438**(7065): p. 201.
38. Orlita, M., et al., *Approaching the Dirac point in high-mobility multilayer epitaxial graphene.* Physical review letters, 2008. **101**(26): p. 267601.
39. Mak, K.F., et al., *Atomically thin MoS 2: a new direct-gap semiconductor.* Physical review letters, 2010. **105**(13): p. 136805.
40. Radisavljevic, B., et al., *Single-layer MoS 2 transistors.* Nature nanotechnology, 2011. **6**(3): p. 147.
41. Zhang, W., et al., *High-gain phototransistors based on a CVD MoS2 monolayer.* Advanced materials, 2013. **25**(25): p. 3456-3461.
42. Bao, W., et al., *High mobility ambipolar MoS2 field-effect transistors: Substrate and dielectric effects.* Applied Physics Letters, 2013. **102**(4): p. 042104.
43. Bernardi, M., M. Palummo, and J.C. Grossman, *Extraordinary sunlight absorption and one nanometer thick photovoltaics using two-dimensional monolayer materials.* Nano letters, 2013. **13**(8): p. 3664-3670.
44. Docherty, C.J., et al., *Ultrafast transient terahertz conductivity of monolayer MoS2 and WSe2 grown by chemical vapor deposition.* ACS nano, 2014. **8**(11): p. 11147-11153.
45. Mai, C., et al., *Many-body effects in valleytronics: direct measurement of valley lifetimes in single-layer MoS2.* Nano Lett, 2014. **14**(1): p. 202-6.
46. Sie, E.J., et al., *Intervalley biexcitons and many-body effects in monolayer MoS 2.* Physical Review B, 2015. **92**(12): p. 125417.

47. Berkelbach, T.C., M.S. Hybertsen, and D.R. Reichman, *Theory of neutral and charged excitons in monolayer transition metal dichalcogenides.* Physical Review B, 2013. **88**(4): p. 045318.
48. Chernikov, A., et al., *Exciton binding energy and nonhydrogenic Rydberg series in monolayer WS 2.* Physical review letters, 2014. **113**(7): p. 076802.
49. Splendiani, A., et al., *Emerging photoluminescence in monolayer MoS2.* Nano letters, 2010. **10**(4): p. 1271-1275.
50. Korn, T., et al., *Low-temperature photocarrier dynamics in monolayer MoS2.* Applied Physics Letters, 2011. **99**(10): p. 102109.
51. Wang, G., et al., *Polarization and time-resolved photoluminescence spectroscopy of excitons in MoSe2 monolayers.* Applied Physics Letters, 2015. **106**(11): p. 112101.
52. Yang, L., et al., *Long-lived nanosecond spin relaxation and spin coherence of electrons in monolayer MoS2 and WS2.* Nature Physics, 2015.
53. Cha, S., et al., *1s-intraexcitonic dynamics in monolayer MoS2 probed by ultrafast mid-infrared spectroscopy.* Nature communications, 2016. **7**.
54. Ross, J.S., et al., *Interlayer exciton optoelectronics in a 2D heterostructure p–n junction.* Nano letters, 2017. **17**(2): p. 638-643.
55. Rivera, P., et al., *Valley-polarized exciton dynamics in a 2D semiconductor heterostructure.* Science, 2016. **351**(6274): p. 688-691.
56. Lui, C.H., et al., *Observation of interlayer phonon modes in van der Waals heterostructures.* Physical Review B, 2015. **91**(16): p. 165403.
57. Ulstrup, S., et al., *Ultrafast Band Structure Control of a Two-Dimensional Heterostructure.* ACS nano, 2016.
58. Hill, H.M., et al., *Observation of excitonic Rydberg states in monolayer MoS2 and WS2 by photoluminescence excitation spectroscopy.* Nano letters, 2015. **15**(5): p. 2992-2997.
59. Ye, Z., et al., *Probing excitonic dark states in single-layer tungsten disulphide.* Nature, 2014. **513**(7517): p. 214.
60. Huang, B., et al., *Layer-dependent ferromagnetism in a van der Waals crystal down to the monolayer limit.* Nature, 2017. **546**(7657): p. 270.
61. Zhong, D., et al., *Van der Waals engineering of ferromagnetic semiconductor heterostructures for spin and valleytronics.* Science advances, 2017. **3**(5): p. e1603113.
62. Naguib, M., et al., *Two‐dimensional nanocrystals produced by exfoliation of Ti3AlC2.* Advanced Materials, 2011. **23**(37): p. 4248-4253.
63. Sadagapan, V. and H. Gatos, *Superconductivity in the transition metal carbides: Mo4. 8Si3C0. 6, Mo0. 95Hf0. 05C0. 75 and Mo2C.* Journal of Physics and Chemistry of Solids, 1966. **27**(2): p. 235-238.
64. Xu, C., et al., *Large-area high-quality 2D ultrathin Mo 2 C superconducting crystals.* Nature materials, 2015. **14**(11): p. 1135.
65. Deng, Y., et al., *Black phosphorus–monolayer MoS2 van der Waals heterojunction p–n diode.* ACS nano, 2014. **8**(8): p. 8292-8299.
66. Je, S.-G., et al., *Asymmetric magnetic domain-wall motion by the Dzyaloshinskii-Moriya interaction.* Physical Review B, 2013. **88**(21).
67. Zhang, Y., et al. *Multi-level cell STT-RAM: Is it realistic or just a dream?* in *2012 IEEE/ACM International Conference on Computer-Aided Design (ICCAD)*. 2012. IEEE.
68. Zhang, Y., et al., *Read performance: The newest barrier in scaled STT-RAM.* IEEE Transactions on Very Large Scale Integration (VLSI) Systems, 2014. **23**(6): p. 1170-1174.
69. Wang, C.-Y., et al. *Impact of external magnetic field on embedded perpendicular STT-MRAM technology qualified for solder reflow*. in *2017 IEEE International Electron Devices Meeting (IEDM)*. 2017. IEEE.
70. Qiu, X., et al., *Characterization and manipulation of spin orbit torque in magnetic heterostructures.* Advanced Materials, 2018. **30**(17): p. 1705699.

71. You, L., et al., *Switching of perpendicularly polarized nanomagnets with spin orbit torque without an external magnetic field by engineering a tilted anisotropy.* Proceedings of the National Academy of Sciences, 2015. **112**(33): p. 10310-10315.
72. Grimaldi, E., et al., *Single-shot dynamics of spin–orbit torque and spin transfer torque switching in three-terminal magnetic tunnel junctions.* Nature nanotechnology, 2020. **15**(2): p. 111-117.
73. Wang, Y., et al., *Electrical control of the exchange spring in antiferromagnetic metals.* Advanced Materials, 2015. **27**(20): p. 3196-3201.
74. Lu, N., et al., *Electric-field control of tri-state phase transformation with a selective dual-ion switch.* Nature, 2017. **546**(7656): p. 124-128.
75. Leon, A.O., et al., *Manipulation of the RKKY exchange by voltages.* Physical Review B, 2019. **100**(1).
76. Železný, J., et al., *Relativistic Néel-order fields induced by electrical current in antiferromagnets.* Physical review letters, 2014. **113**(15): p. 157201.
77. Prenat, G., et al., *Ultra-fast and high-reliability SOT-MRAM: From cache replacement to normally-off computing.* IEEE Transactions on Multi-Scale Computing Systems, 2015. **2**(1): p. 49-60.
78. Prenat, G., et al., *Beyond STT-MRAM, spin orbit torque RAM SOT-MRAM for high speed and high reliability applications*, in *Spintronics-based Computing*. 2015, Springer. p. 145-157.
79. Chen, B., et al., *All-oxide–based synthetic antiferromagnets exhibiting layer-resolved magnetization reversal.* Science, 2017. **357**(6347): p. 191-194.
80. Liu, X., S. Ishio, and H. Ma, *Study of magnetization reversal process in FeCo/Ru/FeCo exchange coupled synthetic antiferromagnetic multilayers.* Journal of Nanomaterials, 2015. **2015**.
81. Li, L., et al., *Interlayer exchange coupling in [Pt/Co]n/MgO/[Co/Pt]2 perpendicular magnetic tunnel junctions.* Journal of Applied Physics, 2014. **116**(12).
82. Shi, G.Y., et al., *Spin-orbit torque in MgO/CoFeB/Ta/CoFeB/MgO symmetric structure with interlayer antiferromagnetic coupling.* Physical Review B, 2017. **95**(10).
83. Wu, G., et al., *Laser-Induced Magnetization Dynamics in Interlayer-Coupled [Ni/Co]4/Ru/[Co/Ni]3 Perpendicular Magnetic Films for Information Storage.* ACS Applied Nano Materials, 2019. **2**(8): p. 5140-5148.
84. Liu, Z.Y. and S. Adenwalla, *Oscillatory interlayer exchange coupling and its temperature dependence in [Pt/Co]3/NiO/[Co/Pt]3 multilayers with perpendicular anisotropy.* Phys Rev Lett, 2003. **91**(3): p. 037207.
85. Parkin, S.S. and D. Mauri, *Spin engineering: Direct determination of the Ruderman-Kittel-Kasuya-Yosida far-field range function in ruthenium.* Phys Rev B Condens Matter, 1991. **44**(13): p. 7131-7134.
86. *Interlayer exchange coupling and its temperature dependence in [Pt/Co]4/MgO/[Co/Pt]2 perpendicular magnetic tunnel junctions.* Journal of Applied Physics, 2010. **108**(7).
87. Ruderman, M.A. and C. Kittel, *Indirect exchange coupling of nuclear magnetic moments by conduction electrons.* Physical Review, 1954. **96**(1): p. 99.
88. Kasuya, T., *Prog. Theor. Phys.* Prog. Theor. Phys., 1956. **16**: p. 45.
89. Yosida, K. and A. Okiji, *Spin Polarization of Conduction Electrons Due to s-d Exchange Interaction.* Progress of Theoretical Physics, 1965. **34**(4): p. 505-522.
90. Yang, Q., et al., *Ionic liquid gating control of RKKY interaction in FeCoB/Ru/FeCoB and (Pt/Co)2/Ru/(Co/Pt)2 multilayers.* Nat Commun, 2018. **9**(1): p. 991.
91. Pauli, W., *Exclusion principle and quantum mechanics*, in *Writings on Physics and Philosophy*. 1994, Springer. p. 165-181.
92. Weiss, P., *L'hypothèse du champ moléculaire et la propriété ferromagnétique.* 1907.
93. Cowan, R.D., *The theory of atomic structure and spectra*. 1981: Univ of California Press.
94. O'handley, R.C., *Modern magnetic materials: principles and applications*. 2000: Wiley.

95. Xu, Y., et al., *Giant enhancement of orbital moments and perpendicular anisotropy in epitaxial Fe/GaAs (100).* Journal of Applied Physics, 2001. **89**(11): p. 7156-7158.
96. Ikeda, S., et al., *A perpendicular-anisotropy CoFeB–MgO magnetic tunnel junction.* Nature materials, 2010. **9**(9): p. 721-724.
97. Sirotkin, E. and F.Y. Ogrin, *Anisotropic Coupling in Hexagonal Arrays of Asymmetric Nickel Nano-Rings.* IEEE Transactions on Magnetics, 2010. **46**(6): p. 1840-1843.
98. Bairagi, K., et al., *Tuning the magnetic anisotropy at a molecule-metal interface.* Physical review letters, 2015. **114**(24): p. 247203.
99. Bruno, P., *Tight-binding approach to the orbital magnetic moment and magnetocrystalline anisotropy of transition-metal monolayers.* Phys Rev B Condens Matter, 1989. **39**(1): p. 865-868.
100. Weller, D., et al., *Microscopic origin of magnetic anisotropy in Au/Co/Au probed with x-ray magnetic circular dichroism.* Physical Review Letters, 1995. **75**(20): p. 3752.
101. Hubert, A. and R. Schäfer, *Magnetic domains: the analysis of magnetic microstructures*. 2008: Springer Science & Business Media.
102. Vaterlaus, A., T. Beutler, and F. Meier, *Spin-lattice relaxation time of ferromagnetic gadolinium determined with time-resolved spin-polarized photoemission.* Physical review letters, 1991. **67**(23): p. 3314.
103. Koopmans, B., et al., *Explaining the paradoxical diversity of ultrafast laser-induced demagnetization.* Nature materials, 2010. **9**(3): p. 259-265.
104. Koopmans, B., et al., *Explaining the paradoxical diversity of ultrafast laser-induced demagnetization.* Nat Mater, 2010. **9**(3): p. 259-65.
105. Hübner, W. and K. Bennemann, *Simple theory for spin-lattice relaxation in metallic rare-earth ferromagnets.* Physical Review B, 1996. **53**(6): p. 3422.
106. Banerjee, C., et al., *Single pulse all-optical toggle switching of magnetization without Gd: The example of Mn2RuxGa.* 2019.
107. Fowley, C., et al., *Magnetocrystalline anisotropy and exchange probed by high-field anomalous Hall effect in fully compensated half-metallic Mn 2 Ru x Ga thin films.* Physical Review B, 2018. **98**(22): p. 220406.
108. You, C.Y. and S.C. Shin, *Derivation of simplified analytic formulae for magneto‐optical Kerr effects.* Applied Physics Letters, 1996. **69**(9): p. 1315-1317.
109. Yang, Z.J. and M.R. Scheinfein, *Combined three-axis surface magneto-optical Kerr effects in the study of surface and ultrathin-film magnetism*. J. Appl. Phys., 1993. **74**(11): p. 6810.
110. Van der Ziel, J., P.S. Pershan, and L. Malmstrom, *Optically-induced magnetization resulting from the inverse Faraday effect.* Physical review letters, 1965. **15**(5): p. 190.
111. Pitaevskii, L., *Electric forces in a transparent dispersive medium.* Sov. Phys. JETP, 1961. **12**(5): p. 1008-1013.
112. Ostler, T., et al., *Ultrafast heating as a sufficient stimulus for magnetization reversal in a ferrimagnet.* Nature communications, 2012. **3**: p. 666.
113. Lu, X., et al., *Roles of heating and helicity in ultrafast all-optical magnetization switching in TbFeCo.* Applied Physics Letters, 2018. **113**(3): p. 032405.
114. Alebrand, S., et al., *Light-induced magnetization reversal of high-anisotropy TbCo alloy films.* Applied Physics Letters, 2012. **101**(16).
115. Cheng, F., et al., *All‐Optical Helicity‐Dependent Switching in Hybrid Metal–Ferromagnet Thin Films.* Advanced Optical Materials, 2020. **8**(13): p. 2000379.
116. Quessab, Y., et al., *Resolving the role of magnetic circular dichroism in multishot helicity-dependent all-optical switching.* Physical Review B, 2019. **100**(2).
117. Nieves, P. and O. Chubykalo-Fesenko, *Modeling of Ultrafast heat-and field-assisted magnetization dynamics in FePt.* Physical Review Applied, 2016. **5**(1): p. 014006.

118. Lee, O.J., et al., *Central role of domain wall depinning for perpendicular magnetization switching driven by spin torque from the spin Hall effect.* Physical Review B, 2014. **89**(2).
119. Kimel, A.V., et al., *Ultrafast non-thermal control of magnetization by instantaneous photomagnetic pulses.* Nature, 2005. **435**(7042): p. 655-7.
120. Popova, D., A. Bringer, and S. Blügel, *Theory of the inverse Faraday effect in view of ultrafast magnetization experiments.* Physical Review B, 2011. **84**(21).
121. Vahaplar, K., et al., *Ultrafast path for optical magnetization reversal via a strongly nonequilibrium state.* Phys Rev Lett, 2009. **103**(11): p. 117201.
122. Hertel, R.J.J.o.m. and m. materials, *Theory of the inverse Faraday effect in metals.* 2006. **303**(1): p. L1-L4.
123. Kalashnikova, A.M., A.V. Kimel, and R.V. Pisarev, *Ultrafast opto-magnetism.* Physics-Uspekhi, 2015. **58**(10): p. 969-980.
124. Popova, D., A. Bringer, and S. Blügel, *Theoretical investigation of the inverse Faraday effect via a stimulated Raman scattering process.* Physical Review B, 2012. **85**(9).
125. Shen, Y.R. and N. Bloembergen, *Interaction between Light Waves and Spin Waves.* Physical Review, 1966. **143**(2): p. 372-384.
126. Mueller, B.Y., M. Haag, and M. Fähnle, *Ab initio theory for ultrafast magnetization dynamics with a dynamic band structure.* Journal of Magnetism and Magnetic Materials, 2016. **414**: p. 14-18.
127. Hohenberg, P. and W. Kohn, *Density functional theory (DFT).* Phys. Rev, 1964. **136**: p. B864.
128. Kohn, W. and L.J. Sham, *Self-consistent equations including exchange and correlation effects.* Physical review, 1965. **140**(4A): p. A1133.
129. Ceperley, D.M. and B.J. Alder, *Ground state of the electron gas by a stochastic method.* Physical review letters, 1980. **45**(7): p. 566.
130. Perdew, J.P. and W. Yue, *Accurate and simple density functional for the electronic exchange energy: Generalized gradient approximation.* Physical review B, 1986. **33**(12): p. 8800.
131. Agranat, M., et al., *Interaction of picosecond laser pulses with the electron, spin, and phonon subsystems of nickel.* Zh. Eksp. Teor. Fiz, 1984. **86**(1376): p. 10.
132. Ryan, J., et al., *Time-resolved photoluminescence of two-dimensional hot carriers in GaAs-AlGaAs heterostructures.* Physical review letters, 1984. **53**(19): p. 1841.
133. Mourou, G. and K. Meyer, *Subpicosecond electro‐optic sampling using coplanar strip transmission lines.* Applied Physics Letters, 1984. **45**(5): p. 492-494.
134. Stathis, J. and M. Kastner, *Time-resolved photoluminescence in amorphous silicon dioxide.* Physical Review B, 1987. **35**(6): p. 2972.
135. Beechem, J.M. and L. Brand, *Time-resolved fluorescence of proteins.* Annual review of biochemistry, 1985. **54**(1): p. 43-71.
136. Dornes, C., et al., *The ultrafast Einstein-de Haas effect.* Nature, 2019. **565**(7738): p. 209-212.
137. Shapiro, S.L. and D.H. Auston, *Ultrashort light pulses: picosecond techniques and applications*. 1977: Springer.
138. Atxitia, U. and T.A. Ostler, *Ultrafast double magnetization switching in GdFeCo with two picosecond-delayed femtosecond pump pulses.* Applied Physics Letters, 2018. **113**(6).
139. Xu, Y., et al., *Ultrafast Magnetization Manipulation Using Single Femtosecond Light and Hot‐Electron Pulses.* Advanced Materials, 2017. **29**(42): p. 1703474.
140. Banerjee, C., et al., *Single pulse all-optical toggle switching of magnetization without Gd: The example of Mn2RuxGa.* arXiv preprint arXiv:1909.05809, 2019.
141. Lu, X., et al., *Roles of heating and helicity in ultrafast all-optical magnetization switching in TbFeCo.* Applied Physics Letters, 2018. **113**(3).
142. Alebrand, S., et al., *Interplay of heating and helicity in all-optical magnetization switching.* Physical Review B, 2012. **85**(9).

143. Vahaplar, K., et al., *All-optical magnetization reversal by circularly polarized laser pulses: Experiment and multiscale modeling.* Physical Review B, 2012. **85**(10).
144. Nieves, P. and O. Chubykalo-Fesenko, *Modeling of Ultrafast Heat- and Field-Assisted Magnetization Dynamics in FePt.* Physical Review Applied, 2016. **5**(1).
145. Chimata, R., et al., *Microscopic model for ultrafast remagnetization dynamics.* Phys Rev Lett, 2012. **109**(15): p. 157201.
146. Cheng, T., et al., *Dual-pump manipulation of ultrafast demagnetization in TbFeCo.* Physical Review B, 2016. **93**(6).
147. Schneider, C.A., W.S. Rasband, and K.W. Eliceiri, *NIH Image to ImageJ: 25 years of image analysis.* Nat Methods, 2012. **9**(7): p. 671-5.
148. Evans, R.F., et al., *Atomistic spin model simulations of magnetic nanomaterials.* Journal of Physics: Condensed Matter, 2014. **26**(10): p. 103202.
149. Zhang, W., et al., *The indispensable role of the transversal spin fluctuations mechanism in laser-induced demagnetization of Co/Pt multilayers with nanoscale magnetic domains.* 2018. **29**(27): p. 275703.
150. Kimling, J. and D.G. Cahill, *Spin diffusion induced by pulsed-laser heating and the role of spin heat accumulation.* Physical Review B, 2017. **95**(1): p. 014402.
151. Evans, R.F., et al., *Ultrafast thermally induced magnetic switching in synthetic ferrimagnets.* Applied Physics Letters, 2014. **104**(8): p. 082410.
152. Medapalli, R., et al., *Multiscale dynamics of helicity-dependent all-optical magnetization reversal in ferromagnetic Co/Pt multilayers.* Physical Review B, 2017. **96**(22): p. 224421.
153. Yamada, K.T., et al., *Efficient all-optical helicity-dependent switching in Pt/Co/Pt with dual laser pulses.* arXiv preprint arXiv:1903.01941, 2019.
154. Kresse, G. and J. Hafner, *Ab initio molecular dynamics for liquid metals.* Physical Review B, 1993. **47**(1): p. 558.
155. Kresse, G. and J. Hafner, *Ab initio molecular dynamics for open-shell transition metals.* Physical Review B, 1993. **48**(17): p. 13115.
156. Kresse, G. and J. Furthmuller, *Phys Rev B 54: 11169 https://doi. org/10.1103*. 1996, PhysRevB.
157. Haas, P., et al., *Insight into the performance of GGA functionals for solid-state calculations.* Physical Review B, 2009. **80**(19): p. 195109.
158. Perdew, J.P., K. Burke, and M. Ernzerhof, *Generalized gradient approximation made simple.* Physical review letters, 1996. **77**(18): p. 3865.
159. Momma, K. and F. Izumi, *VESTA 3for three-dimensional visualization of crystal, volumetric and morphology data.* Journal of Applied Crystallography, 2011. **44**(6): p. 1272-1276.
160. Lin, C.-J., et al., *Magnetic and structural properties of Co/Pt multilayers.* Journal of Magnetism and Magnetic Materials, 1991. **93**: p. 194-206.
161. Kyuno, K., et al., *Theoretical study on the strain dependence of the magnetic anisotropy of X/Co(X=Pt, Cu, Ag, and Au) metallic multilayers.* Journal of Applied Physics, 1996. **79**(9): p. 7084-7089.
162. Kim, J.H. and S.C. Shin, *Interface roughness effects on the surface anisotropy in Co/Pt multilayer films.* Journal of applied physics, 1996. **80**(5): p. 3121-3123.
163. Beaurepaire, E., et al., *Spin dynamics in CoPt 3 alloy films: A magnetic phase transition in the femtosecond time scale.* Physical Review B, 1998. **58**(18): p. 12134.
164. Anisimov, V.V., J. Zaanen, and O.K. Andersen, *Band theory and Mott insulators: Hubbard U instead of Stoner I.* Phys Rev B Condens Matter, 1991. **44**(3): p. 943-954.
165. Kulik, H.J., et al., *Density functional theory in transition-metal chemistry: a self-consistent Hubbard U approach.* Phys Rev Lett, 2006. **97**(10): p. 103001.
166. Li, J. and P.M. Haney, *Optical spin transfer and spin-orbit torques in thin film ferromagnets.* Phys Rev B, 2017. **96**.
167. Grimaldi, C. and P. Fulde, *Theory of screening of the phonon-modulated spin-orbit interaction in metals.* Physical Review B, 1997. **55**(23): p. 15523.

168. Chang, C.H. and M.H. Kryder, *Effect of substrate roughness on microstructure, uniaxial anisotropy, and coercivity of Co/Pt multilayer thin films.* Journal Of Applied Physics, 1994. **75**(10): p. 6864-6866.
169. Stillrich, H., et al., *Magnetic anisotropy and the cone state in Co/Pt multilayer films.* Journal of Applied Physics, 2009. **105**(7): p. 07C308.
170. Zhang, Z., P. Wigen, and S. Parkin, *Pt layer thickness dependence of magnetic properties in Co/Pt multilayers.* Journal of applied physics, 1991. **69**(8): p. 5649-5651.
171. Knepper, J.W. and F.Y. Yang, *Oscillatory interlayer coupling inCo ／ Ptmultilayers with perpendicular anisotropy.* Physical Review B, 2005. **71**(22).
172. Vomir, M., M. Albrecht, and J.-Y. Bigot, *Single shot all optical switching of intrinsic micron size magnetic domains of a Pt/Co/Pt ferromagnetic stack.* Applied Physics Letters, 2017. **111**(24): p. 242404.
173. Bruno, P. and C. Chappert, *Oscillatory coupling between ferromagnetic layers separated by a nonmagnetic metal spacer.* Physical review letters, 1991. **67**(12): p. 1602.
174. Němec, P., et al., *Antiferromagnetic opto-spintronics.* Nature Physics, 2018. **14**(3): p. 229-241.
175. Baltz, V., et al., *Antiferromagnetic spintronics.* Reviews of Modern Physics, 2018. **90**(1): p. 015005.
176. Bonfiglio, G., et al., *Magnetization dynamics of the compensated ferrimagnet*

Mn2RuxGa. Physical Review B, 2019. **100**(10).
177. Parkin, S., R. Bhadra, and K. Roche, *Oscillatory magnetic exchange coupling through thin copper layers.* Physical Review Letters, 1991. **66**(16): p. 2152.
178. Kampfrath, T., et al., *Coherent terahertz control of antiferromagnetic spin waves.* Nature Photonics, 2011. **5**(1): p. 31-34.
179. Yang, Q., et al., *Ionic Gel Modulation of RKKY Interactions in Synthetic Anti-Ferromagnetic Nanostructures for Low Power Wearable Spintronic Devices.* Adv Mater, 2018. **30**(22): p. e1800449.
180. Saarikoski, H., et al., *Current-driven dynamics of coupled domain walls in a synthetic antiferromagnet.* Physical Review B, 2014. **90**(9).
181. Zhang, Q., et al., *Terahertz Emission From an Exchange-Coupled Synthetic Antiferromagnet.* Physical Review Applied, 2020. **13**(5).
182. Kim, K., et al., *Interlayer coupling field in spin valves with CoFe/Ru/CoFe/FeMn synthetic antiferromagnets.* Journal of Applied Physics, 2001. **89**(11): p. 7612-7615.
183. Weisheit, M., et al., *Electric field-induced modification of magnetism in thin-film ferromagnets.* Science, 2007. **315**(5810): p. 349-351.
184. Hoveyda, F., et al., *Ultrafast demagnetization at high temperatures.* Journal of Physics: Condensed Matter, 2018. **30**(19): p. 195802.
185. Roth, T., et al., *Temperature Dependence of Laser-Induced Demagnetization in Ni: A Key for Identifying the Underlying Mechanism.* Physical Review X, 2012. **2**(2).
186. Carpene, E., et al., *Dynamics of electron-magnon interaction and ultrafast demagnetization in thin iron films.* Physical Review B, 2008. **78**(17).
187. Kuneš, J. and V. Kamberský, *First-principles investigation of the damping of fast magnetization precession in ferromagnetic 3 d metals.* Physical Review B, 2002. **65**(21): p. 212411.
188. Mizukami, S., et al., *Laser-induced fast magnetization precession and Gilbert damping for CoCrPt alloy thin films with perpendicular magnetic anisotropy.* Applied physics express, 2010. **3**(12): p. 123001.
189. Azzawi, S., A. Hindmarch, and D. Atkinson, *Magnetic damping phenomena in ferromagnetic thin-films and multilayers.* Journal of Physics D: Applied Physics, 2017. **50**(47): p. 473001.
190. Briner, B. and M. Landolt, *Thermally activated bilinear and biquadratic exchange coupling across amorphous silicon.* EPL (Europhysics Letters), 1994. **28**(1): p. 65.
191. Yosida, K., *Magnetic properties of Cu-Mn alloys.* Physical Review, 1957. **106**(5): p. 893.

192. Kastler, A., *Optical methods of atomic orientation and of magnetic resonance.* JOSA, 1957. **47**(6): p. 460-465.
193. Grunberg, P., et al., *Layered magnetic structures: Evidence for antiferromagnetic coupling of Fe layers across Cr interlayers.* Phys Rev Lett, 1986. **57**(19): p. 2442-2445.
194. Bruno, P., *Theory of intrinsic and thermally induced interlayer magnetic coupling between ferromagnetic films separated by an insulating layer.* Phys Rev B Condens Matter, 1994. **49**(18): p. 13231-13234.
195. Bruno, P., *Theory of interlayer magnetic coupling.* Phys Rev B Condens Matter, 1995. **52**(1): p. 411-439.
196. Toscano, S., et al., *Exchange-coupling between ferromagnets through a non-metallic amorphous spacer-layer.* Journal of magnetism and magnetic materials, 1992. **114**(1-2): p. L6-L10.
197. Faure-Vincent, J., et al., *Interlayer magnetic coupling interactions of two ferromagnetic layers by spin polarized tunneling.* Physical review letters, 2002. **89**(10): p. 107206.
198. Yakushiji, K., et al., *Perpendicular magnetic tunnel junctions with strong antiferromagnetic interlayer exchange coupling at first oscillation peak.* Applied Physics Express, 2015. **8**(8).
199. Sato, H., et al., *Co/Pt multilayer based reference layers in magnetic tunnel junctions for nonvolatile spintronics VLSIs.* Japanese Journal of Applied Physics, 2014. **53**(4S): p. 04EM02.
200. Koopmans, B., et al., *Ultrafast magneto-optics in nickel: Magnetism or optics?* Physical Review Letters, 2000. **85**(4): p. 844.
201. Bigot, J.-Y., M. Vomir, and E. Beaurepaire, *Coherent ultrafast magnetism induced by femtosecond laser pulses.* Nature Physics, 2009. **5**(7): p. 515-520.
202. Wu, G., et al., *Annealing effect on laser-induced magnetization dynamics in Co/Ni-based synthetic antiferromagnets with perpendicular magnetic anisotropy.* Applied Physics Letters, 2019. **115**(14).
203. Koopmans, B., *Handbook of Magnetism and Advanced Magnetic Materials*. 2007, Wiley, New York.
204. Dalla Longa, F., et al., *Influence of photon angular momentum on ultrafast demagnetization in nickel.* Physical Review B, 2007. **75**(22): p. 224431.
205. Malinowski, G., et al., *Control of speed and efficiency of ultrafast demagnetization by direct transfer of spin angular momentum.* Nature Physics, 2008. **4**(11): p. 855-858.
206. Thielemann-Kuhn, N., et al., *Ultrafast and Energy-Efficient Quenching of Spin Order: Antiferromagnetism Beats Ferromagnetism.* Phys Rev Lett, 2017. **119**(19): p. 197202.
207. Geim, A.K. and K.S. Novoselov, *The rise of graphene.* Nature materials, 2007. **6**(3): p. 183.
208. Xiao, D., et al., *Coupled spin and valley physics in monolayers of MoS 2 and other group-VI dichalcogenides.* Physical Review Letters, 2012. **108**(19): p. 196802.
209. Yan, T., et al., *Long valley relaxation time of free carriers in monolayer WSe 2.* Physical Review B, 2017. **95**(24): p. 241406.
210. Baugher, B.W., et al., *Intrinsic electronic transport properties of high-quality monolayer and bilayer MoS2.* Nano letters, 2013. **13**(9): p. 4212-4216.
211. Verdi, C. and F. Giustino, *Fröhlich electron-phonon vertex from first principles.* Physical review letters, 2015. **115**(17): p. 176401.
212. Sohier, T., et al., *Breakdown of optical phonons' splitting in two-dimensional materials.* Nano letters, 2017. **17**(6): p. 3758-3763.
213. Luo, Y.K., et al., *Opto-valleytronic spin injection in monolayer MoS2/Few-layer graphene hybrid spin valves.* Nano letters, 2017. **17**(6): p. 3877-3883.
214. Clark, S.J., et al., *First principles methods using CASTEP.* Zeitschrift für Kristallographie-Crystalline Materials, 2005. **220**(5/6): p. 567-570.
215. Li, H., et al., *From bulk to monolayer MoS2: evolution of Raman scattering.* Advanced Functional Materials, 2012. **22**(7): p. 1385-1390.

216. Jin, W., et al., *Direct measurement of the thickness-dependent electronic band structure of MoS 2 using angle-resolved photoemission spectroscopy.* Physical review letters, 2013. **111**(10): p. 106801.
217. Zhang, Y., et al., *Direct observation of the transition from indirect to direct bandgap in atomically thin epitaxial MoSe2.* Nature nanotechnology, 2014. **9**(2): p. 111-115.
218. Tongay, S., et al., *Thermally driven crossover from indirect toward direct bandgap in 2D semiconductors: MoSe2 versus MoS2.* Nano letters, 2012. **12**(11): p. 5576-5580.